UNIVERSITY OF CALIFORNIA,
IRVINE

DYNAMIC SYSTEM MODELS FOR MECHANISM OF DEEP BRAIN STIMULATION AND DYSTONIA

DISSERTATION

submitted in partial satisfaction of the requirements
for the degree of

DOCTOR OF PHILOSOPHY

in Biomedical Engineering

by

Maral Kasiri

Dissertation Committee:
Professor Terence D. Sanger, Chair
Professor David Reinkensmeyer
Associate Professor Beth Lopour

2024

DEDICATION

to love, children, and peace!

TABLE OF CONTENTS

LIST OF FIGURES

LIST OF TABLES

ACKNOWLEDGMENTS

I would like to thank my committee chair and advisor, Professor Terence D. Sanger, for his guidance, support, and kindness throughout my entire PhD. His advice has always been invaluable for my academic journey, prospective careers, and also personal life. I want to express my sincere appreciation to Dr. Sanger who have always encouraged me to follow my intuition and believe in my capabilities. Without his brilliant guidance, ideas, perspective, and generous funding, this PhD and dissertation would not be possible.

I would also like to thank my dissertation and qualifying exam committee members, Prof. David J. Reinkensmeyer, Dr. Beth A. Lopour, Dr. Autumn S. Ivy. and Dr. Gregory Brewer their feedback on my research results in 2022, which guided me and directed the last two years of my research work. Their suggestions and insights have been crucial and invaluable for enhancing the quality of my work.

Further, I would like to acknowledge my fellow lab members, including Dr. Estefanía Hernandez-Martin, Dr. Jonathan Realmuto, Dr. Alireza Mousavi, Dr. Sumiko Abe, Jennifer MacLean, Dr. Allison Przekop, Aprille Tongol, Jaya Nataraj, Jessica Widmark-Hillman, Yun Sun, Rahil Soroushmojdehi, Sina Javadzadeh No, Mehrnaz Asadi, Alexandra Zakharova, Teresa Serna, and Alyson Matsuoka. My lab-mates have played an important role in this dissertation in gathering of data, assistance with neurological examinations, data analysis, brainstorming, and feedback. I also greatly appreciate Dr. Mark Liker and Dr. Joffre Olaya for performing the surgeries for our patients and enabling us to gather all the data at the hospital. In addition, I would like to acknowledge Dr. Emilia Ambrosini, Dr. Emilia Biffi, and Dr. Alessandra Pedrocchi for their contributions to my research during the first year of my PhD.

In addition, I would like to specifically thank Dr. Sanger for providing generous financial support in the last 4 years of my study at University of California- Irvine (UCI). I would also thank University of Southern California (USC) for granting me the Viterbi Fellowship during my first year as a PhD student in 2019. My thanks also go to UCI and the department of biomedical engineering for supporting me financially by granting me a graduate fellowship for the last quarter of my PhD and teaching assistance positions. Further, I express my sincerest gratitude towards our patients, research participants, and their parents for participating in our studies and allowing us to use their data to advance research within the fields of movement disorders, deep brain stimulation, and human neurophysiology. Without your selfless contributions, this dissertation would not have been possible.

Last but not least, I want to thank my parents and sisters for their unwavering support of any kind and their patience. I also thank my dearest friends, who are like family to me, for always being there for me and supporting me through the hard times.

I thank you all sincerely.

VITA

Maral Kasiri

EDUCATION

Ph.D. in Biomedical Engineering — 2024
University of California-Irvine (UCI) — Irvine, California

M.Sc. in Biomedical Engineering — 2018
University of Southern California (USC) — Los Angeles, California

B.Sc. in Biomedical Engineering- Biomechanics — **2**016
Amirkabir University of Technology (Tehran Polytechnic) — Tehran, Tehran

JOB/RESEARCH EXPERIENCE

Data Science Intern — 2024
Sage Therapeutics — Cambridge, Massachusetts

Graduate Research Assistant — 2020-2024
Sanger Lab - University of California, Irvine — Irvine, California

Computation Intern — 2023
Evozyne Inc. — Chicago, Illinois

Graduate Research Assistant — 2019–2020
Sanger Lab - USC — Los Angeles, California

Graduate Research Assistant — 2020
Informatics and Computing in Neuroscience (ICON) lab - USC — Los Angeles, California

Research Assistant — 2018–2019
Human Performance and Robotics Lab, Cal. State - Long Beach — Long Beach, California

Student Researcher — 2016–2018
Valero Lab - USC — Los Angeles, California

TEACHING EXPERIENCE

Teaching Assistant — 2022-2023
University of California - Irvine — Irvine, California

Teaching Associate — 2018-2019
California State University - Long Beach — Long Beach, California

PUBLICATIONS

Local field potential signal transmission is correlated with the anatomical connectivity measured by diffusion tractography **2024**

Maral Kasiri, Sumiko Abe, Rahil Soroushmojdehi, Estefania Hernandez-Martin, S. Alireza Seyyed Mousavi, Terence Sanger, medRxiv, 10.1101/2024.04.14.24305803

Diffusion tractography predicts Deep Brain Stimulation evoked potential amplitude and delay **2024**

Sumiko Abe, Jessica Sofie Louise Vidmark, Estefania Hernandez-Martin, Maral Kasiri, Rahil Soroushmojdehi, S. Alireza Seyyed Mousavi, Terence David Sanger, medRxiv, 10.1101/2024.04.11.24305627

Exogenous brain stimulation pulses are carried along the motor pathways from pallidum to distant targets: Results of a transfer function analysis **2023**

Maral Kasiri, Jessica Widmark Hillman, Estefania Hernandez-Martin, S. Alireza Seyyed Mousavi, Terence D Sanger, medRxiv, 2023.04. 28.23289218

Improvement of speed-accuracy trade-off with practice of a novel task in children with secondary dystonia **2023**

Maral Kasiri, Emilia Biffi, Emilia Ambrosini, Alessandra Pedrocchi, Terence D Sanger, Journal of Neurophysiology, 10.1152/jn.00214.2023

Globus Pallidus internus increases activity during movement in children with secondary dystonia **2023**

Estefania Hernandez-Martin, Maral Kasiri, Sumiko Abe, Jennifer MacLean, Joffre Olaya, Mark Liker, Jason Chu, Terence D Sanger, iScience Journal, 10.1016/j.isci.2023.107066

Correlated activity in globus pallidus and thalamus during arm movement in three children with primary dystonia **2023**

Maral Kasiri, Sina Javadzadeh, Jaya Nataraj, s Alireza Seyyed Mousavi, Terence D Sanger, Dystonia Medical Research Foundation, 10.3389/dyst.2023.11117

ABSTRACT OF THE DISSERTATION

DYNAMIC SYSTEM MODELS FOR MECHANISM OF DEEP BRAIN STIMULATION AND DYSTONIA

By

Maral Kasiri

Doctor of Philosophy in Biomedical Engineering

University of California, Irvine, 2024

Professor Terence D. Sanger, Chair

Dystonia is a movement disorder characterized by involuntary muscle contractions leading to abnormal movements and postures. This movement disorder poses significant challenges to affected individuals. Treating children with dystonia is challenging, as the condition is a network disorder impacting the brain's entire signaling system, rather than being localized to a specific brain region. This involves dystonic signals propagating through the neuronal network, extending from the cortex to the muscles. This irregular or imbalanced signal transmission is believed to be the root cause of dystonic symptoms. These symptoms manifest as spasticity, abnormal postures, and involuntary muscle contractions, each contributing to the nature of this disorder. Although many have studied the pathophysiology of dystonia, the pattern of neural activity in dystonia still remains unclear.

While dystonic symptoms can be managed or moderated through medication or other methods a definitive cure remains elusive. Therefore, further investigation on the mechanism of dystonia and its treatments are required. This dissertation aims to elucidate the complex mechanisms of dystonia and motor control in pediatric patients, with a primary emphasis on the effects of deep brain stimulation (DBS) on the deep brain regions, using principles of control theory and dynamic models. DBS has been widely used as an effective symp-

tomatic treatment of dystonia. This treatment involves implantation of depth leads inside deep brain regions which allows us to study the neural behavior and transmission within the brain networks affected by dystonia. In addition to the focus on dynamic models of neural signal transmission, this study explores the potential of sensory awareness as a non-invasive therapeutic option to ameliorate motor symptoms associated with dystonia, included as additional chapters to this dissertation. Through comprehensive analysis and experimentation, this dissertation research contributes to the advancement of DBS as a treatment of various neurological disorders and understanding of dystonia's underlying neurophysiological mechanisms.

The outcomes presented in this dissertation stem from my efforts in devising strategies to handle neurophysiological data, eliminate noise, and construct computational models informed by concepts of electrical engineering and my deep understanding of human neurophysiology and neuroscience. By employing these methodologies and knowledge, I aspire to make a small but lasting impact on the understanding of the mechanisms of dystonia and DBS. I am convinced that my doctoral investigation has advanced our comprehension of the effects of DBS and abnormal patterns of neural activity associated with dystonia, aiming to achieve optimal clinical outcomes for patients with dystonia and also other related movement and neurological disorders.

INTRODUCTION

Dystonia Definition and Epidemiology. Dystonia is characterized by involuntary, sustained muscle contractions (maintained co-contraction of agonist and antagonist muscles) leading to abnormal postures, twisting, repetitive movements, or tremor, often exacerbated by movement attempts [5, 209, 208, 176, 238]. Dystonia is the third most common movement disorder, after Parkinson's disease, affecting approximately 500,000 adults and children in north America [182]. It is a dynamic disorder, with severity fluctuating based on activity and posture. The condition may manifest in various forms, including, but not limited to, over-extension or over-flexion of the hand, inversion of the foot, lateral flexion or retro-flection of the head, spinal torsion with back arching and twisting, forceful eye closure, or a fixed grimace. These symptoms typically subside during resting state and sleep [182].

Etiology. Dystonia is a condition, exhibiting a wide range of symptoms, causes, and clinical manifestations. One of the ways to categorize dystonia is based on its etiology: primary (genetic) and secondary (acquired) dystonia [192, 79, 50].

Primary dystonia, also known as idiopathic dystonia, is characterized by dystonia being the only neurological sign, apart from tremor, after excluding acquired or neurodegenerative causes which is further categorized into early-onset (childhood) and adult-onset types [182, 208]. Although the exact cause of primary dystonia is unclear, it is believed to have a significant genetic component, even in cases without a family history of dystonia, and is likely influenced by a combination of genetic susceptibility and environmental factors. Early-onset primary dystonia generally starts in a limb and often progresses to become generalized. This form is frequently associated with mutations in the DYT1 and DYT6 genes [182]. In contrast, adult-onset dystonia typically affects the cervical, cranial, or brachial muscles and usually remains focal or segmental. Notably, cervical dystonia is the most prevalent form of adult-onset dystonia and is more common than early-onset primary dystonia [182].

Secondary dystonias arise from environmental factors and have identifiable causes such as head injuries, side effects of drugs (like tardive dyskinesia), or underlying neurological diseases (such as Cerebral Palsy and Wilson disease) [182, 207].

Pathophysiology. The principal cause of dystonia has been thought to be dysfunction of the basal ganglia, as the basal ganglia is thought to be responsible for integrating motor control signals [200]. Secondary dystonia is often due to lesions of the basal ganglia, specifically the putamen or globus pallidus. However, the absence of neurodegeneration in primary dystonia, as well as observations that lesions of brain regions other than the basal ganglia can cause secondary dystonia, has led to the idea that dystonia is a neuro-functional or network disorder; meaning that it is characterized by abnormal connectivity that may occur in a structurally normal-appearing brain and it may occur as the transmission of abnormal signals through the brain network [190, 207, 206, 182]. In other words, dystonia is considered to be a motor system disorder rather than a disease of a particular motor structure. Studies have provided evidence of dysfunction in almost every region of the central nervous system involved in motor control and sensorimotor integration, including cortex, brainstem, cerebellum, and spinal cord [182, 207, 238, 211]. Neurophysiological studies demonstrate a variety of changes consistent with abnormalities in inhibitory control, sensorimotor integration, and brain plasticity [182, 200]. The studies on muscle activation in the dystonia show inaccurate co-contraction of agonist and antagonist muscles with prolonged bursts and overflow to the muscles [147, 182].

Treatment Methods. Dystonia involves disruptions in the sensorimotor circuit due to various causes, affecting multiple brain regions including the basal ganglia [207, 182, 237]. Treatment primarily includes medications and botulinum toxin. Physical, occupational, and speech therapies are also beneficial, and some patients may need ambulatory aids [182].

The most effective medications for treating dystonia include anticholinergics (such as trihexyphenidyl), GABA agonists (like baclofen and benzodiazepines), and dopaminergic agents.

These drugs work by altering dopaminergic and cholinergic neurotransmission and reducing GABA-mediated inhibition in the dystonic central nervous system (CNS) [182, 237].

For focal dystonia, botulinum toxin injections are highly effective. These injections block the release of acetylcholine at the neuromuscular junction, leading to temporary muscle weakness and decreased activity in the affected dystonic muscles [85, 182, 96, 188]. Botulinum toxin is the first-line treatment for cervical dystonia and is commonly used for laryngeal dystonia, and focal limb dystonia. Beside its peripheral effects, botulinum toxin injections may also alter afferent feedback from affected muscles, potentially normalizing abnormal changes in the CNS [85, 182, 96].

Dystonia used to be treated with surgical procedures like pallidotomy or thalamotomy (surgically removing parts of pallidum or thalamus). While these surgical procedures were beneficial for some symptoms, they often resulted in permanent and debilitating side effects, such as dysarthria [86, 225, 34]. These surgeries have largely been replaced by deep brain stimulation (DBS) [233], which offers a reversible and adjustable approach similar to a lesional effect. Over the past two decades, DBS has emerged as a significant treatment option for patients with severe primary dystonia [207, 205, 214, 212, 206]. The globus pallidus (GPi) is the established target for DBS in dystonia cases [207, 92]. This intervention is thought to work by inducing functional changes within the abnormal motor networks of dystonia, aiming to normalize pathologically overactive motor responses. Unlike the immediate effects seen in Parkinson's disease or essential tremor, the impact of DBS in dystonia is typically delayed, often taking weeks to months [207, 205, 214, 212, 206]. This aligns with the understanding of dystonia as a sensorimotor connectivity disorder that requires time to adjust and adapt to changes across the entire motor circuit following DBS [182].

The response to DBS in dystonia patients varies significantly, with some experiencing dramatic improvements, while others see only modest benefits or none at all [207]. Currently, no single factor, including the status of the DYT1 gene, has been conclusively identified as

a predictor of DBS efficacy. The mechanism of DBS and determination of which patients with primary or secondary dystonia will respond best to DBS is still an open question and needs further research [207, 182].

Despite the above-mentioned advancements, there are instances where such treatments fall short in effectiveness, leaving patients in need of alternative solutions. This gap underscores the critical necessity for the development and exploration of additional treatment modalities for secondary dystonia. This dissertation aims to include a comprehensive study on the mechanism of DBS in dystonia by addressing the following questions: 1) What is the mechanism of dystonia?; 2) what are the patterns of neural activity in deep brain regions of children with dystonia, during the rest and voluntary movement?; 3) How does DBS change these patterns of activation and functional connectivity?; 4) How are these patterns related to the anatomical connectivity? Additionally, in the last two chapters of this dissertation the effectiveness of augmented vibrotactile biofeedback device is explored, as a noninvasive add-on, for improvement of movement in children with dystonia.

Chapter Summaries

Summary of Chapter 1: Increased and correlated activity in globus pallidus and thalamus during voluntary reaching movement.

In this chapter, I tested the classical rate model of the physiology of dystonia in three patients who have undergone DBS surgery for the treatment of dystonia. The classical models of the physiology of dystonia suggest that involuntary muscle contractions are caused by inappropriate low activity in GPi that fails to adequately inhibit thalamic inputs to cortex. The deep brain signals were recorded through the implanted externalized depth Stereoelectroencephalography (sEEG) leads during a voluntary reaching task. I, then, compared the corresponding muscle activity with the power in the spectrogram of the local field potential (LFP) and spike counts in GPi, subthalamic nucleus (STN), and the Ventralis oralis ante-

rior/posterior (VoaVop) and Ventral Anterior (VA) subnuclei of the thalamus, while subjects are at rest or attempting to make active voluntary arm or leg reaching movements. In all subjects, both spectrogram power and spike activity in GPi, STN, VoaVop, and VA are positively correlated with movement. In particular, GPi and STN, both increase activity during movement. These results contradict the classical rate model of the patho-physiology of dystonia, and support more recent models that propose abnormalities in the detailed pattern of activity rather than the overall lumped activity of pallidum and thalamus.

This chapter is published in *Dystonia Journal, special issue "Motor Circuits and Motor Symptoms in Dystonia: Translational Approaches from Animal Models to Patients", Volume 2, Pages 11117 in February 2023.*

Summary of Chapter 2: Dynamic causal model to study rest-to-active phase transition in pallidum and thalamus

As mentioned above, the rate model of basal ganglia function predicts that muscle activity in dystonia is due to disinhibition of the thalamus resulting from decreased inhibitory input from the pallidum. However, I showed contradictory results in patients with primary dystonia in the previous chapter. In this chapter, we tested this hypothesis in a larger cohort, including nine children with dyskinetic cerebral palsy (DCP). Here, I analyzed movement-related activity and phase transition from resting state to active state in motor subnuclei of pallidum and thalamus. The initial evaluation of patterns of activities in pallidum and thalamus revealed prominent alpha- and theta-band frequency peaks in the GPi, VoaVop subnuclei of the thalamus, and STN during movement but not at rest. Connectivity and phase transition analysis using dynamic causal modeling (DCM) indicated stronger coupling between STN-VoaVop and STN-GPi compared to GPi-VoaVop. These findings contradict the hypothesis of decreased thalamic inhibition in dystonia, suggesting that abnormal patterns of inhibition and disinhibition, rather than reduced GPi activity, contribute to the disorder. Additionally, the study implies that correcting abnormalities in GPi function or it

projection to thalamus may explain the effectiveness of DBS targeting the STN and GPi in treating dystonia.

This chapter is published in *iScience Journal, Volume 26, Issues 7, Publisher Elsevier, July 2023.*

Summary of Chapter 3: Deep brain stimulation in globus pallidus internus travels to thalamus and subthalamic nuclei along physiological pathways

In this chapter, I studied how DBS pulses affect the distant targets in deep brain regions, specifically from pallidum to thalamus. The traditional belief that DBS primarily affects the site of stimulation is challenged by recent findings, which demonstrate that DBS can generate robust evoked potentials (EPs) both locally and in distant brain regions. This indicates that DBS's electrical effects may modulate downstream targets, though the exact therapeutic implications of these EPs remain uncertain. The mechanisms by which DBS pulses reach these distant areas, and the paths they take, are still not fully understood. Various scenarios, including orthodromic and antidromic transmission, among others, are some of the possibilities. The availability of recordings from deep brain regions with DBS on and off enables us to study how DBS pulses are transmitted. We hypothesized that DBS pulses travel via the same pathways used by intrinsic neural signals. This was explored through a transfer function analysis comparing impulse responses in the brain during DBS-off and DBS-on states. The findings indicate that electrical pulses from DBS partially travel through the brain's intrinsic motor pathways, as evidenced by the ability to partially predict the elicited evoke responses due to pallidal stimultion, using only the intrinsic neural activity.

Summary of Chapter 4: DBS modulates transmission of dystonic signals in pallidothalamic network

In this chapter, I assessed how DBS modulates the transmission of signals in pallidothalamic network. Based on the clinical efficacy of DBS for children with dystonia, GPi of basal

ganglia or the STN are the effective stimulation targets, although the specific mechanism of action is unknown. Based on the results from previous chapter, dystonic patients show increased low frequency activity in GPi, STN and thalamus. Here we test this hypothesis that DBS modulates the transmission of abnormal low-frequency oscillations (LFOs), thereby improving motor symptoms by altering deep brain regions activity and LFO projections onto thalamic motor subnuclei. Therefore we analyzed intracranial signals from thirteen pediatrics and young-adults with dystonia, with DBS on and off. We tested the effect of DBS with various stimulation frequencies on the transfer function gains of pathways within the deep brain regions and the power spectral density of each region. The results confirmed that GPi and STN stimulation effectively changes the transfer function gains from pallidum to motor subnuclei of thalamus in low frequency bands, by jamming the pathways. These results elicit a better understanding of the mechanism and effects of DBS. This, in turn, may provide fundamental knowledge for the development of closed-loop DBS, particularly in controlling the intensity and pattern of stimulation. A better understanding of neuromodulation could also help to further the design of brain-computer interfaces and neurorehabilitation systems.

Summary of Chapter 5: Local field potential signal transmission is correlated with the anatomical connectivity measured by diffusion tractography

In this chapter, I explored the relationship between diffusion tensor imaging (DTI) parameters of anatomical connectivity and signal transmission characteristics derived from DBS-off transfer function models, previously discussed. The focus here is on the connection between structural and functional connectivity in dystonia patients. For this study, before undergoing DBS, DTI scans were obtained from twelve patients. After performing image analysis and finding the anatomical tracts, measures of anatomical connectivity were computed. We then computed measures of functional connectivity from the DBS-off transfer functions, such as maximum gain of the transfer function and the maximal energy transmission. We then employed Generalized Linear Model (GLM) analysis to examine the relationships between

these measures. Results revealed a positive correlation between the fractional anisotropy (FA) and axial diffusivity (AD) with the intrinsic neural transmission measures from the transfer function models; But we found no significant correlation between the transmission and the number of fiber tracts or their length. These results indicate that white matter integrity, as indicated by FA and AD, may mirror the amplification and propagation of intrinsic brain signals across the network. Highlighting the crucial link between structural and functional connectivity, this study provides insights into the propagation of intrinsic signals within the brain network.

Summary of Chapter 6: Effect of EMG-activated vibrotactile biofeedback on skill learning

In this chapter, I assessed whether an augmented vibrotactile biofeedback improves skill learning in children with dystonia. Based on the theory of failure of motor learning, children with secondary dystonia have sensory deficit, which could adversely affect learning. Here, we proposed that this device may improve the skill learning in children with secondary dystonia, as they have sensory deficit. We evaluated the device's effect on motor learning by assessing motor performance, using Fitt's law, in children with both types of dystonia (primary and secondary), during performing of point-to-point and cyclic trajectory following tasks. The findings of this study indicate that the vibrotactile feedback device significantly aids movement improvement in cyclic and smooth tasks, but not in point-to-point movements, in children with acquired dystonia.

Summary of Chapter 7: Improvement of speed-accuracy trade-off during practice of a point-to-point task

Based on the results from the previous chapter, we found that children with secondary dystonia learn the task by practice. In other words, their movement improves following one week of practice of point-to-point. We used the speed-accuracy trade-off (Fitt's law)

principles, to explore if children with secondary dystonia adopt a different strategy during learning in comparison with healthy children. The results of this study showed that both healthy children and children with acquired dystonia move more slowly performing the more difficult tasks, and both groups improve the relationship between speed and task difficulty after one week of practice. We also showed that healthy children adopt a safer strategy compared to children with dystonia. These results indicate that both groups compensate for risk and signal-dependent noise (inherent variability) and that the increased variability in dystonia can be modified with practice.

This chapter is published in *Journal of Neurophysiology, Volume 130, Issue 4, Pages 931-940 in October 2023.*

General methods

0.1 Patient selection

In total, data from 24 pediatric and young adult patients with dystonia (acquired, genetic, or neurometabolic) are used in this dissertation. Patients with dystonia were selected for DBS surgery if there existed potential stimulation target(s) identifiable with magnetic resonance imaging (MRI) and if alternative medical therapies such as botulinum toxin injections and standard pharmacotherapy had been ineffective [212, 239, 209, 207]. The patients were diagnosed with dystonia by a pediatric movement disorder specialist (T.D.S.) using standard criteria [209]. The patients' demographics and the temporary leads' locations are described in Table 1. All patients or parents of minors provided signed informed consent for surgical procedures in accordance with standard hospital practice at Children's Health Orange County (CHOC) or Children's Hospital Los Angeles (CHLA). The patients or parents of minor patients also consented or assented to Health Insurance Portability and Accountability Act (HIPAA) authorization for the research use of protected health information and the recorded electrophysiological data.

0.2 Surgical procedure

As part of our clinical procedure for determining DBS targets, we implanted up to 12 temporary AdTech MM16C (Adtech Medical Instrment Corp., Oak Creek, WI, USA) externalized sEEG depth leadds (Fig. 4.1) into potential DBS targets [132]. Based on prior studies of clinical efficacy in children with dystonia, typical targets for DBS include STN and GPi, in basal ganglia, ventral intermediate (VIM), VoaVop, and VA thalamic subnuclei [214, 207], pedunculopontine nucleus (PPN) [145] and substantia nigra reticulata (SNr) [66]. A sample

Table 1: Patients Demographics; Patients are between 6-25 year-old; CP: Cerebral Palsy, GA1: Glutaric aciduria type 1, F: female; M: male.

Subject	Etiology	Gender	Implanted Regions
S1	DYT1	F	VA, VoaVop, STN, VIM, GPi
S2	KMT2B	M	VA, VoaVop, VIM, STN, 2 GPi leads
S3	KMT2B	M	VA, VoaVop, STN, VIM, PPN, 2 GPi leads
S4	CP	F	VA, VoaVop, VIM, STN, 2 GPi leads
S5	CP (HIE)	M	VA, VoaVop, VIM, STN, 2 GPi leads
S6	CP	F	VA, VoaVop, VIM, STN, GPi
S7	CP	F	VA, VoaVop, VIM, STN, 2 GPi leads
S8	CP	M	VPL, VoaVop, VIM, STN, GPi
S9	CP	F	VA, VoaVop, VIM, STN, GPi
S10	CP	M	VA, VoaVop, VIM, STN, GPi
S11	CP	F	VA, VoaVop, VIM, STN, GPi
S12	CP	F	VA, VoaVop, VIM, 2 GPi leads
S13	Metabolic	M	VA, VoaVop, STN, VIM, PPN, 3 GPi leads
S14	Metabolic	M	VA, VoaVop, STN, VIM, PPN, 3 GPi leads
S15	Unknown	M	VA, VoaVop, STN, PPN, 2 GPi leads
S16	CP	M	VA, VoaVop, STN, VIM, PPN, 2 GPi leads
S17	GA1	M	VA, VoaVop, STN, VIM, PPN, 2 GPi leads
S18	H-ABC	M	STN, VoaVop, VIM, 2 GPi leads
S19	GA1	M	VA, VoaVop, STN, VIM, 2 GPi leads
S20	atypical PKAN	M	VoaVop, STN, SNr, VIM, PPN, 3 GPi leads
S21	CP	M	VA, VoaVop, STN, SNr, VIM, PPN, 2 GPi leads
S22	MYH2	M	VoaVop, STN, SNr, VIM, PPN, 3 GPi leads
S23	CP	M	VoaVop, STN, SNr, VIM, PPN, 3 GPi leads

of the externalized leads and the implanted regions in the deep brain is shown in Figure 1[1]. Depth electrodes were placed using standard stereotactic procedure [133, 132], with the most distal stimulation contact placed at the target location. Electrode locations were confirmed by co-registration of the preoperative MRI with postoperative computed tomography (CT) scan [92] as depicted in Figure 2.

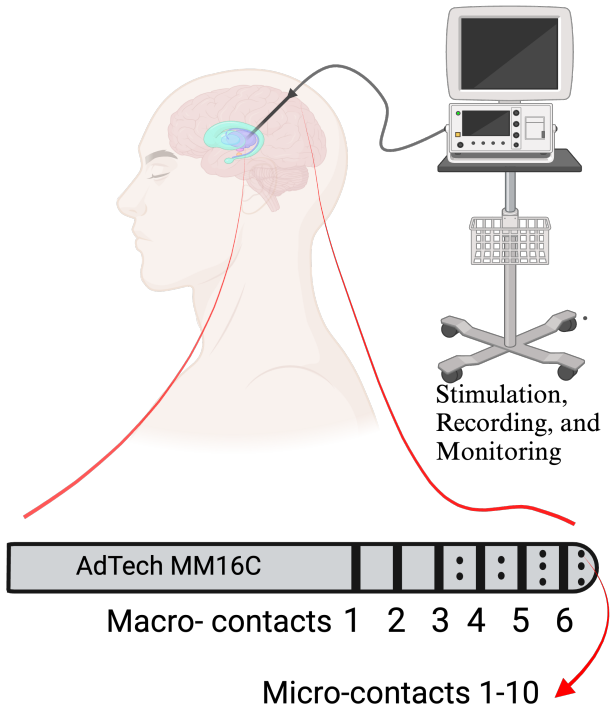

Figure 1: Schematic of externalized Adtech sEEG Leads, containing 6 macro-contacts for stimulation and recording and 10 high-impedance micro-contacts for recording only.

The patients were then transferred to the neuromodulation monitoring unit (NMU) at the children's hospital of Orange County (CHOC) or Children's Hospital, Los Angeles (CHLA) for DBS programming and testing different patterns of stimulation and the assessment of their clinical efficacy. During this phase, which can last up to seven days, we captured local field potential (LFP) signals via depth electrodes with and without stimulation. Thereafter,

[1]Created with BioRender.com

the clinical DBS team and neurologist determine the optimal stimulation target(s), and the temporary depth leads are then removed [132, 133]. Two weeks after the removal of the temporary leads, the permanent ones are implanted at the chosen DBS targets, along with the pulse generator [132, 133].

0.3 Instrumentation and setup

Each implanted lead contains 6 low-impedance (1–2 $k\Omega$) ring macro-contacts, with 2 mm height and 5 mm on-center spacing, and 10 high-impedance (70–90 $k\Omega$) micro-wire electrodes (50-μm diameter) referred to as micro-contacts. The micro-contacts are arranged in groups of 2 or 3, evenly spaced around the circumference of the lead shaft, halfway between adjacent pairs of the first four macro-contacts. A schematic of the electrode is shown in Figure 1. The leads were connected to Adtech Cabrio™ connectors with a custom unity-gain preamplifier for each micro-contact to reduce noise and motion artifacts. Macro-contacts bypassed the preamplifiers to allow for external electrical stimulation. This setup enables clinicians to stimulate through macro-contacts while simultaneously recording from all the micro- and macro-contacts. All data reported here are recorded from the high-impedance electrodes (micro-contacts). These signals were amplified and sampled at 24 kHz by a system with a PZ5M 256-channel digitizer and RZ2 processor, and stored in a RS4 high speed data storage (Tucker-Davis Technologies Inc., Alachua, FL, USA) [92].

In addition to the LFP recordings, we recorded muscle activity from 16 surface electromyography (EMG) Trigno™ Avanti (Delsys Incorporated, Natick, MA) sensors, attached to upper and lower extremities. We recorded EMG signals from biceps, triceps, flexor carpi ulnaris, extensor carpi radialis, gastrocnemius, tibialis, quadriceps, and hamstrings bilaterally, to track the changes in muscles activity with the brain activity. All EMG signals were sampled at 2 kHz and the EMG system was synchronized with the TDT using a pulse generator.

0.4 DBS electrode localization

[2] Preoperative anatomical brain scans were acquired using a MAGNETOM 3T MRI scanner (SIEMENS Medical System, Erlangen, Germany). A magnetization-prepared rapid gradient-echo (MP RAGE) sequence was used to achieve precise anatomical mapping, with repetition time (TR) of 1800 ms, an echo time (TE) of 2.25 ms, a flip angle of 8°, a voxel size of 1 mm^3, and a field of view (FOV) of 240 mm^2. After the operation, computed tomography (CT) scans were acquired with GE (GENERAL ELECTRIC Healthcare, Milwaukee, WI, USA) CT scanner.

To find and segment the brain regions, first, we used Freesurfer software [62] and localized deep brain regions. After We manually adjusted this segmentation by FreeView (a view tool of FreeSurfer), a transformation matrix of deep brain regions (including thalamus, pallidum, and brainstem) was computed from each individual space region to Montreal Neurological Institute (MNI) space by FSL FLIRT tool [101]. Thereafter, the transformation matrices were used to transform the sub-regions from DISTAL atlas (built by LEAD-DBS [61]) to the "actual" individual space.

For visualization of lead trajectories, we can not use standard softwares [98] because they do not support the specifications of our sEEG leads and are unable to visualize 10 to 14 leads simultaneously. Therefore, for localization of sEEG leads, we used macro-contacts metal artifacts in the CT-scans to create a binary mask of spatial coordinates of the macro-contacts for all Adtech sEEG leads [111]. We aligned the CT and T1-volumes using the FLIRT tool in FSL (Figure 2 a, b) and projected 3D voxel values onto 2D images [125], to precisely localize the lead trajectories.

After the lead trajectories were estimated based on the projection coordination (Figure 2b),

[2]Dr. Sumiko Abe performed all the image processing and electrode localization, and these steps are included in the methods section for the clarity of dissertation methodology.

a linear calculation was applied to find the location of micro-contacts which are located between macro contacts based on the device specification. Finally, we used DSI-studio package [247] to integrate the sEEG leads coordinates with the atlas images as depicted in Figure 2c. This method enabled us to localize each micro-contacts row of sEEG leads, as some leads target multiple regions within the deep brain.

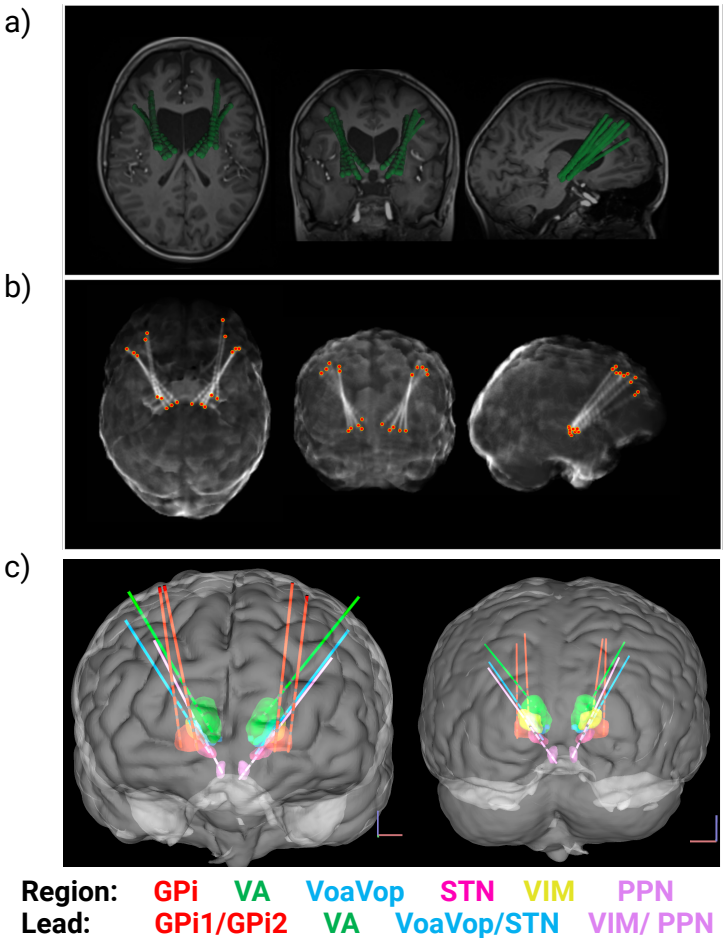

Figure 2: (a,b) sEEG lead trajectory reconstruction in axial (left), coronal (middle), and sagittal (right) views in an individual space. (a) The CT scan is marked as a dense structure and fitted onto the structural images. (b) Projection images in axial, coronal, and sagittal views are used to reconstruct the positions of the sEEG leads. (c) Anterior (left) and posterior (right) views of reconstructed lead trajectories and nuclei segments in one patient; DBS targets were segmented and the spatial coordinates of the leads were calculated. The figure illustrates GPi (red), VA (green), VoaVop (blue), and VIM (yellow), STN (magenta), PPN (violet) along with the reconstructed sEEG lead trajectories using DSI studio package.

0.5 Elecrophysiological recording protocols

Elecrophysiological recordings were conducted at the NMU after localization of the leads' macro-contacts. We recorded intracranial LFPs from all patients, with and without stimulation, following our standard protocol for testing the efficacy of different stimulation settings explained below.

Baseline recording

Baseline data were recorded through all micro-contacts and all leads while patients were awake sitting comfortably in bed.

Stimulation protocol

Stimulation pulses of 90 μs width, 3 V amplitude, at five different frequencies (25, 55, 85, 185, and 250 Hz) were administered through two adjacent macro-contacts (anode and cathode) at a time, ensuring that the cathode is in the desired DBS target. For stimulation frequencies above 60 Hz, we setup the stimulation protocol such that to ramp up the voltage, from 0 to 3 V at the rate of .25 volt per second, for the convenience of the patient. We administered approximately 1200 pulses per stimulation frequency after ramping up the voltage. The LFP signals were recorded through the micro-contacts simultaneously during the stimulation as shown in Figure 3).

Voluntary reaching task

Patients were asked to perform voluntary reaching task with their upper or lower limbs while we recorded LFP and EMG signals from the muscles of the corresponding limb. The

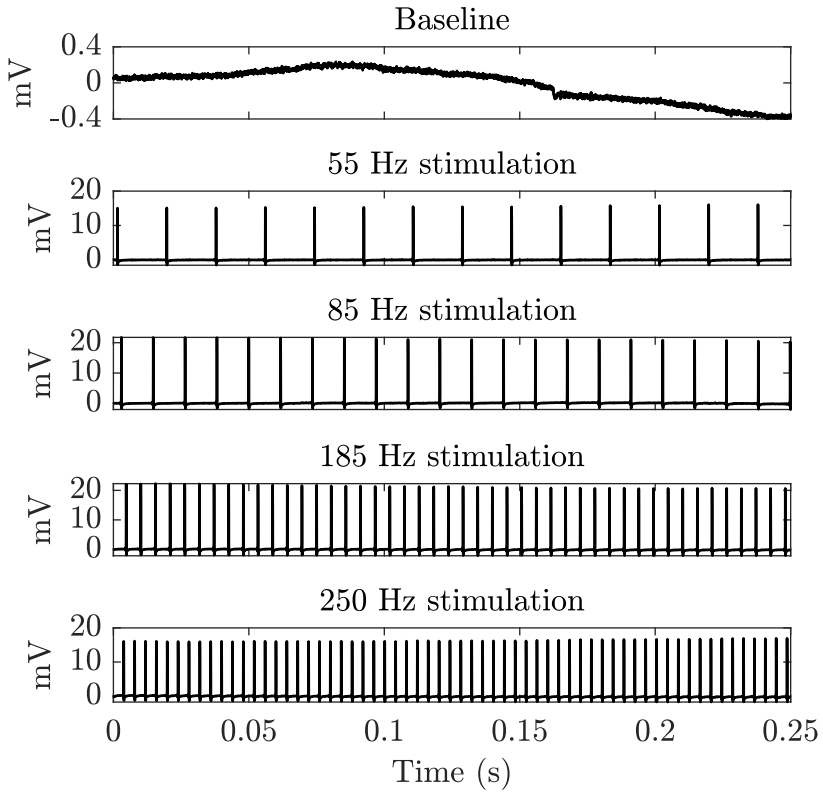

Figure 3: Sample of raw data recorded over 0.25 seconds during baseline, and during DBS at 55, 85, 185, and 250 Hz.

experiment is designed for them to perform about 100 seconds of reaching task followed by thirty seconds of resting period for 4-6 consecutive trials. In all cases, dystonia was present in the tested limb, as evident by the presence of dystonic postures interfering with expected performance of the task. Movement and rest onset and offset times were marked and synchronized automatically with the EMG recordings during the experiment.

0.6 General data treatment

LFP filtering

The LFP recordings from 10 micro-contacts of each lead were notch filtered at 60 Hz up to 5 harmonics. They were then high pass filtered at 1 Hz to remove the drift. Subtraction of micro-contact pairs were used to capture the voltage difference between each two adjacent pairs and to remove the common noise (bipolar montage). For example, instead of using micro contacts 1 to 3 separately, we used their subtraction (1-2, 1-3, and 2-3). This kind of filtering removes the common noise from the data and reveals the underlying activity. The signals recorded from three micro contacts before and after the filtering are shown in Figure 4.

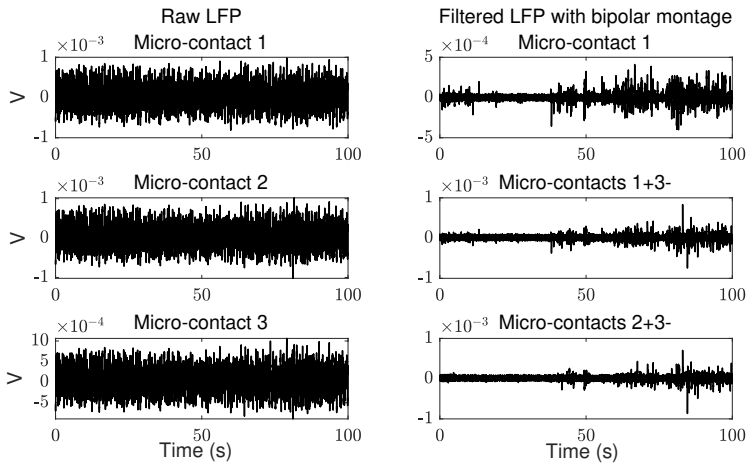

Figure 4: LFP recordings during the voluntary task for 1 trial. The recordings are from three micro contacts on the first row of an STN lead (left). The signals were high pass filtered and transformed into the bipolar montage of each pair of adjacent contacts (right)

EMG filtering

The EMG signals were filtered using a Bayesian nonlinear filter to highlight the changes in muscle activity, the onset and offset, as well as the activation itself. This filter models

the EMG signal as a random process and estimates this random process using a Bayesian estimation. This estimate is proportional to the isometric joint torque and has a higher signal-to-noise ratio compared to other linear methods of filtering [203]. An EMG signal before and after the Bayesian nonlinear filter is shown in Figure 5.

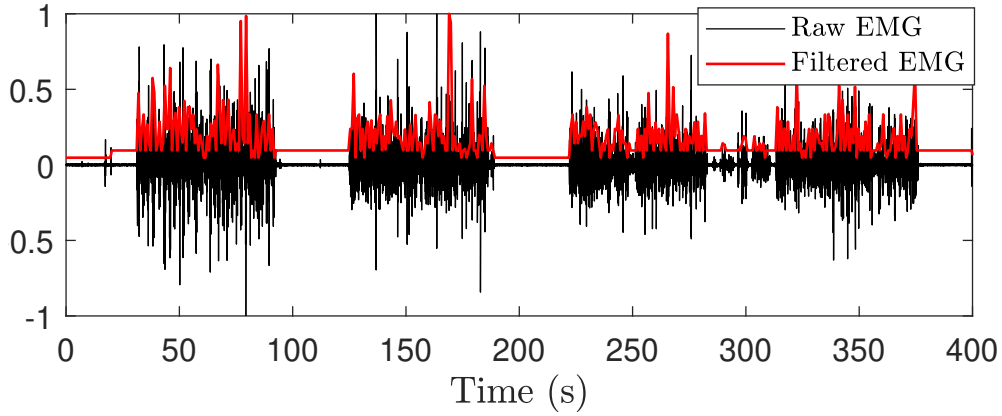

Figure 5: Biceps EMG recording (normalized) during the voluntary reaching task for 4 trials (black) and the Bayesian filtered signal (red).

Chapter 1

Increased and correlated activity in globus pallidus and thalamus during voluntary reaching movement

1.1 Abstract

Classical models of the physiology of dystonia suggest that involuntary muscle contractions are caused by inappropriate low activity in Globus Pallidus internus (GPi) that fails to adequately inhibit thalamic inputs to cortex. In this study, we test this hypothesis in three children with primary dystonia who have undergone DBS surgery for the treatment of dystonia. We recorded their deep brain signals through externalized depth sEEG leads during a voluntary reaching task. We, then, compared the corresponding muscle activity with the power in the spectrogram of the local field potential (LFP) and spike counts in GPi, subthalamic nucleus (STN), and the Ventral oralis (VoaVop) and Ventral Anterior (VA) subnuclei of the thalamus, while subjects are at rest or attempting to make active voluntary arm or

leg reaching movements. In all three subjects, both spectrogram power and spike activity in GPi, STN, VoaVop, and VA are positively correlated with movement. In particular, GPi and STN, both increase activity during attempted movement. These results contradict the classical rate model of the physiology of dystonia, and support more recent models that propose abnormalities in the detailed pattern of activity rather than the overall lumped activity of pallidum and thalamus.

1.2 Introduction

The classical "rate" model of basal ganglia physiology in dystonia developed by Albin and others has been built upon the known anatomical connections between striatum, pallidum, subthalamus, and thalamus [6, 56, 242]. Inhibitory projection neurons originating in striatum and pallidum will hyperpolarize their targets in pallidum, subthalamus, and thalamus, while excitatory projection neurons in subthalamus and thalamus will depolarize their targets in pallidum and cortex. In primates, there is a division into direct and indirect pathways. The direct pathway includes inhibitory projections from striatum to Globus Pallidus internus (GPi) and from GPi to thalamus, followed by excitatory projections from thalamus to cortex. The indirect pathway includes inhibitory projections from striatum to Globus Pallidus externus (GPe), from GPe to subthalamic nucleus (STN), and from GPi to thalamus, with excitatory projections from STN to GPi. Modifications of this model over the past decades have recognized the important role of a "hyperdirect" pathway from cortex to STN, as well as pathways from STN to GPe, GPi to STN, and medial thalamic nuclei to striatum. In all models, the final common pathway linking basal ganglia to thalamus remains the inhibitory projection from GPi to thalamus including the ventral oralis anterior and posterior (VoaVop) and ventral anterior (VA) subnuclei [58, 184].

The patterns of excitatory and inhibitory connections suggest what has been referred to as

the classical "rate" model. The simplicity of this model has led to widespread adoption, and it has proven useful in the prediction of the physiology of Parkinson's disease, in which high firing rates in GPi are thought to cause inappropriate inhibition of thalamic outputs to cortex, thus leading to delayed movement initiation and decreased speed of movement (bradykinesia) [6]. The finding of relatively lower firing rates in GPi during voluntary movement in some patients with dystonia has led to the suggestion that dystonia is due to the opposite problem: failure of inhibition of thalamic outputs to cortex [24]; thus, potentially leading to excessive involuntary muscle contractions (such as overflow, co-contraction, or hyperkinetic movements) [241, 242]. This theory has been supported in recordings from healthy nonhuman primates showing that GPi activity is typically very high. It has also been supported by the observation that electrical stimulation in GPi can ameliorate symptoms in patients with dystonia.

However, important discrepancies in the application of the classical model to dystonia have been noted [241, 177]. Perhaps the most significant is the observation that lesions in GPi also lead to amelioration of dystonia, whereas the model would predict that lesions would worsen dystonia. Another discrepancy is that if reduction in GPi activity initiates movement in the healthy brain, then there is no mechanism for initiation of activity in a brain with low GPi baseline activity. Another discrepancy is the observation that dystonic muscle activity is almost always caused by or worsened by active attempts at movement, whereas the classical model would predict the presence of dystonia at rest. Another important missing element of some models is the absence of a depolarizing (excitatory) input to thalamus [242]; without such an input, thalamus will never activate and the hyperpolarizing (inhibitory) inputs from GPi will have no effect [56].

We examine the predictions of the classical rate model by making simultaneous recordings from high-impedance electrodes in GPi, STN, VoaVop, and VA in three children with primary dystonia. Recordings are performed as part of a previously-reported targeting method

in which temporary externalized stere-electroencephalography (sEEG) depth electrodes are implanted in potential DBS targets, and children are tested with stimulation and recording while awake and unrestrained [214, 212]. This method eliminates the effects of restrained movement (in the operating room with a head-frame) and sedation and partial anesthesia, and permits prolonged testing with children awake, unrestrained, un-medicated, and performing routine tasks of daily living in a hospital room with parents and clinical staff present. Clinical outcomes from this targeting method have been reported elsewhere. Here we utilize recorded data obtained from the sEEG leads during voluntary arm or leg reaching movements in three children who previously underwent this procedure.

1.3 Materials and methods

1.3.1 Patient selection and data acquisition

In this study, three patients with primary (genetic dystonia) were selected. See S1, S2, and S3 in Table 1 for patients demographics. We sought to study the pattern of activity of thalamus subnuclei and GPi in these subjects during voluntary reaching movement versus rest (baseline). Therefore we only used the DBS-off recordings from VoaVop, VA, STN, and GPi during the voluntary reaching task. All data analyses were performed in MATLAB R2020a (The MathWorks, Inc., Natick, MA, USA)[1].

1.3.2 Time-frequency analysis

To compute the spectrograms of the recorded nonstationary signals, all signals were divided into segments with sixty percent overlap using a Kaiser window with time resolution of three

[1]The experiment protocol and the setup is explained in details in the general methods of this dissertation.

seconds, and 0.7 leakage factor. Next, signals were transformed into the frequency domain using a short-time Fourier transform. Finally, the spectra of each segment were computed to build the spectrograms. The spectrograms were computed in two frequency ranges of 1-13 Hz (delta, theta, and alpha) and 13-35 Hz (beta). This specific frequency ranges are chosen as they are of standard frequency bands used in frequency analysis of brain activity, particularly electroencephalogram (EEG) analysis. Additionally, the delta, theta, alpha, and beta bands are important in other movement disorders such as Parkinson's disease, which shows abnormality in alpha and beta band oscillations [241].

1.3.3 Spike analysis of LFP recording

[2]Spike analysis was performed on the micro-contact LFP recordings, using the bipolar montage, explained earlier. Signals were band-pass filtered between 350 and 3000 Hz using an 8th order Butterworth filter. A non-linear energy operator (NEO) [107] was applied to the data to aid in spike detection by enhancing sharp peaks in bipolar LFP signals:

$$y(t) = x^2(t) - x(t-1)x(t+1) \tag{1.1}$$

where $x(t)$ is a sample of the waveform at time t and $y(t)$ is the enhanced output. Spikes are characterized by localized high frequencies and sharp increases in instantaneous energy. These features are captured in the magnitude of the NEO, which is large only when the signal is high in power [$x^2(t)$ is large] and high in frequency [$x(t-1)x(t+1)$ is small].

Peak detection was performed on the NEO, where the amplitudes of detected peaks were between three and seventy times the standard deviation of the noise. Following event detection, wavelet decomposition was used to extract features from detected events and a

[2]The spike analysis in this chapter was done by Sina Javadzadeh No, S. Alireza Seyyed Mousavi, and Jaya Nataraj. It is included in the chapter for further supporting the results.

Gaussian Mixture Model (GMM) was used to cluster detected events [227]. Events with low probability of belonging to any clusters were removed. Events associated with the same cluster were identified as a "spike" belonging to the same originating neuron(s), and average spike rates were determined within the relevant intervals (movement or rest).

Because the impedance of the recording contacts is less than 100 $k\Omega$, it is likely that the identified spikes correspond to multiple neuron clusters rather than to single units that would be recorded with higher impedance electrodes. Additionally, the spike clusters are identified by consistent shapes. If there were variability in the cluster, the overall shape would vary as well. A spike cluster likely represents a stereotyped firing pattern from a group of nearby neurons. Nevertheless, the spike rates are likely to parallel the neural activity that would be obtained from higher impedance recordings.

1.3.4 Statistical analysis

To measure the effect of movement on the average power in two frequency bands and the spike rates a linear mixed effects model with repeated measures was fitted to the power in each band as well as the spike rates. Repeated measures for the time-frequency analysis are the average power in each frequency band for every 5 seconds of each period of voluntary reaching and rest. Repeated measures for the spike analysis are the average firing rates for each voluntary reaching and rest period. The model for the time frequency analysis consists of condition (active versus rest), frequency range ([1-13] and [13-35] Hz), and their interactions as fixed effects. Subject intercept was included as a random effect, and by-subject random slopes were the frequency range. The model for average spike rate analysis consists of the condition as the fixed effect, while the random effect was assumed to be the subject intercept. All the statistical analyses were done using the lme4 [16] and emmeans [223] packages in R-studio (R core team, 2021).

1.4 Results

Figure 1.1 shows time-frequency and spike analyses of LFP recordings for one subject. LFP recordings, spectrograms, and spike rasters are displayed from top to bottom for contralateral GPi, STN, VoaVop, and VA. Figure 1.1 also includes an example EMG recording from the left biceps to highlight the reaching and resting periods. Results from the spectrogram analysis suggest a clear trend in power, where power is increased during the reaching task in both frequency bands (1-13 Hz and 13-35 Hz) and decreased in rest periods in all target locations. In particular, power starts to increase as the patient starts one period of voluntary reaching and subsequently decreases as the patient is in rest. Additionally, raster plots in all target locations illustrate increased spiking activity in voluntary reaching task periods in comparison to resting states. The observations are consistent among all the three subjects. A linear mixed-effects model was fitted on data from each brain region separately for group analysis. The explained variance of the models are shown in Table 1.1. We performed a pairwise comparison between the rest versus the active state to test for significance of change in firing rates and power. Analysis of variance (ANOVA) using type II Wald chi-square test, with 95% confidence interval was performed on the linear models, and showed a significant difference between the active versus the resting state ($Pr(> chisq) < .01$) for all tested brain regions. We then computed the log of the ratio between active and resting state powers for each frequency range. This measure is significantly different from zero for both frequency ranges. The results are shown in Figure 1.2 for each patient. The average spike rates in both active and resting states for all three patients are shown in Figure 1.3.

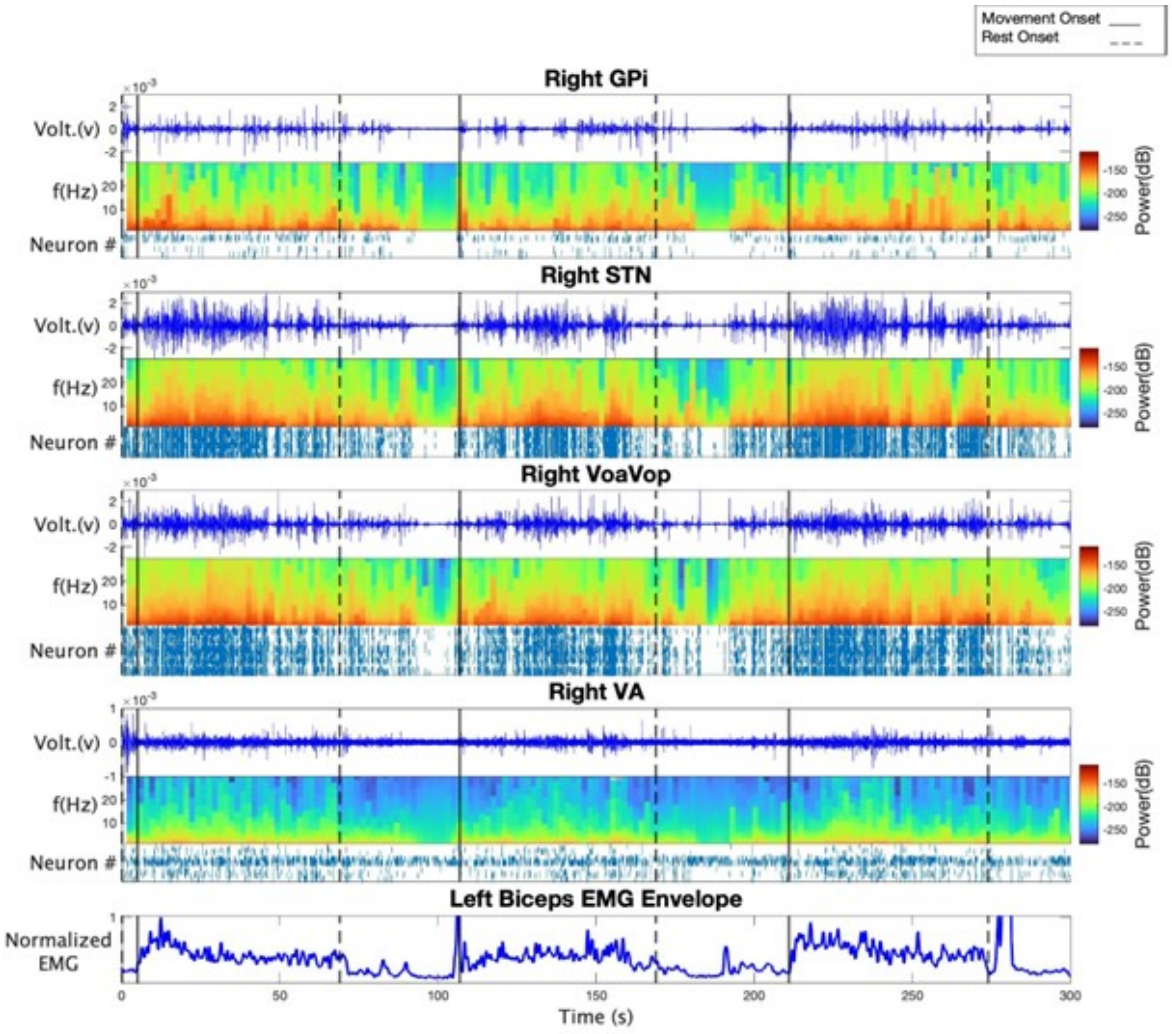

Figure 1.1: From top to bottom: raw LFP recording, spectrogram, and spike raster of GPi, STN, VoaVop, and VA for subject S1. The bottom plot demonstrates left biceps EMG recording as an example in order to highlight voluntary reaching task and rest periods. Spectrogram results show increased power in voluntary reaching task periods compared to resting periods. Spike rasters show increased neural activity in voluntary reaching task periods compared to resting periods.

1.5 Discussion

The classical rate model of basal ganglia function predicts that STN and GPi activity will be low and thalamic activity will be high during movement, and that STN and GPi activity will be high and thalamic activity will be low at rest [6, 185]. While the predictions for VoaVop and VA subnuclei of the thalamus are supported by our results, the predictions for

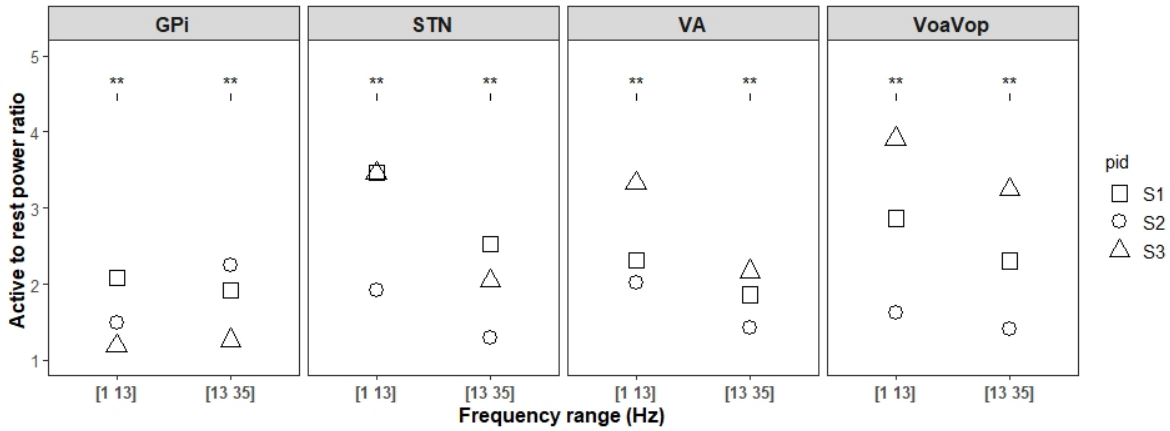

Figure 1.2: Ratio of active to rest average power in frequency ranges 1-13 Hz and 13–35 Hz for three patients are shown by different shapes in GPi, STN, VA, and VoaVop. The group analysis shows that log power ratio is significant for all of them.

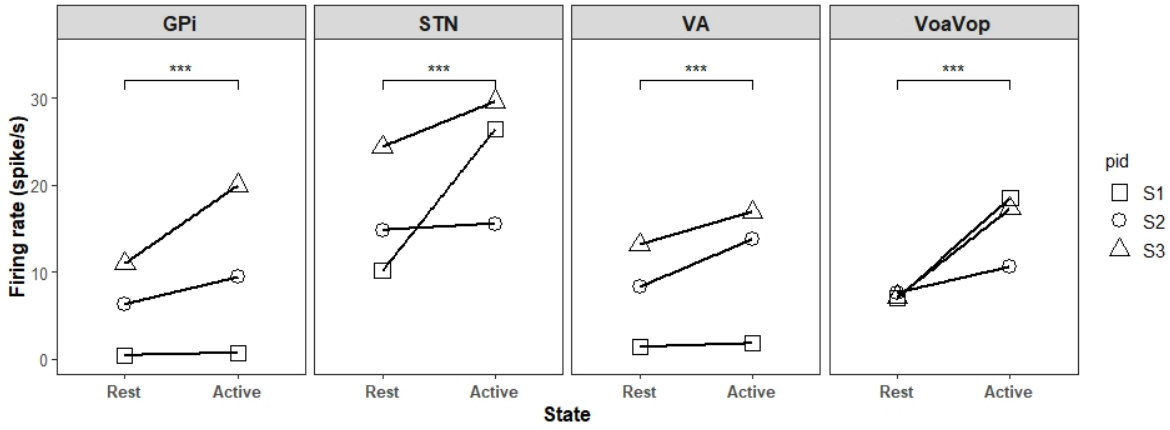

Figure 1.3: The average firing rate of resting versus voluntary reaching state for three subjects and the regression line in GPi, STN, VA, and VoaVop. The group analysis shows a significant increased firing rate during voluntary reaching period in GPi, STN, VA, and VoaVop

STN and GPi are contradicted. Our results are in agreement with prior results in monkeys showing increases in GPi activity from rest to movement, with maintained high GPi activity during movement and voluntary posture [106, 157, 10, 163].

The rate model is known to have significant problems when applied to dystonia [177, 241], and we suggest several possible ways to address these problems as shown by our data. Most importantly, the classical model is incomplete because it does not posit a stimulatory (depolarizing) input to thalamus, and without excitation of thalamus, GPi inhibition would

Group analysis results	Power analysis R^2	Firing rate analysis R^2
GPi	0.49 **	0.42 **
STN	0.76 **	0.22 **
VA	0.68 **	0.53 **
VoaVop	0.88 **	0.34 **

Table 1.1: Statistical results of the linear mixed-effect model fits for group analysis. All the explained variances are reported. The intercepts are significantly different from zero and the pairwise comparison [in both power and spike analysis] revealed that there is a significant difference between movement and resting state at all recorded brain regions (** $p - value < 0.01$)

have no effect (There is no point in inhibiting a neuron that never fires). Although GPi and GPe also receive primary inhibitory input from both striatum and pallidum, both structures also receive excitatory input from STN. The primary excitatory input to thalamus arises from cerebral cortex, and we suggest that augmenting the model with an excitatory cortical-thalamic-cortical loop provides an explanation for the increased thalamic firing during movement [241]. In this case, the role of the GPi is to selectively inhibit this loop at the thalamus, effectively "sculpting" the thalamo-cortical loop. This mechanism is supported by lesion studies showing involuntary antagonist muscle activity resulting from lesions of GPi [158, 161]. Dystonia could arise, similarly to the classical model, from insufficient inhibition of parts of this loop. In this augmented model, GPi would only need to inhibit the loop when thalamus is activated, consistent with our results. The deficit in dystonia would then be either insufficient inhibition (GPi increases rate with movement, but not enough) or an incorrect pattern of inhibition [241, 159] (GPi increases rate with movement but does not properly sculpt the thalamic activity). This proposal is consistent with the finding of abnormal sensory responses in thalamus, consistent with failure of inhibition of cortical inputs [130].

It is worth noting that the suggested dichotomy in which Parkinsonism represents decreased activity while dystonia represents increased activity is an oversimplification that may also be contributing to contradictions with the classical model [24]. Although dystonia was originally

classified as a hyperkinetic disorder, it shares features common to both hyperkinetic disorders (dyskinesia, Huntington's chorea) and hypokinetic disorders (rigidity, bradykinesia) [241]. In children, a combination of parkinsonism and dystonia is typically present in conditions of low dopamine (e.g., dopa-responsive dystonia) or diffuse hypoxic injury (e.g., dyskinetic cerebral palsy) [205]. Electromyographic (EMG) recordings from both Parkinsonism and dystonia demonstrate slow rates of contraction and change in contraction levels [71, 147] and both Parkinsonism and dystonia have hyperkinetic components that can include tremor and dyskinesia. Therefore, while electrophysiological data continue to support increased activity in GPi in parkinsonism compared with dystonia, both disorders may include a failure of appropriate inhibition of thalamo-cortical loops that includes both insufficient inhibition of unwanted movement and insufficient disinhibition of intended movement. Such similarities would be consistent with the observation that DBS in either GPi or STN as well as dopaminergic medication can ameliorate symptoms in both disorders.

Our results appear to contradict recordings from human and nonhuman primate models of dystonia that typically show very high GPi activity at rest [242] , inconsistent with the rate model. We suggest three hypotheses to explain this discrepancy. First, it is possible that nonhuman primates and humans have different patterns of activity in basal ganglia. Second, we only obtain recordings from human patients with severe disease, whereas the nonhuman primate recordings are typically made in healthy animals. Third, a nonhuman primate strapped into a recording apparatus with head immobilized may not be truly at rest, and ongoing isometric force exerted against the seating system and head immobilization system may not always be evident but could nevertheless lead to baseline activation of deep brain regions associated with movement or posture.

The results presented here include several important weaknesses. First, we tested only three children, and although all three have a genetic origin of their dystonia, the specific mutations are different. This suggests that the phenomena we observed are not confined to a single

cause of primary dystonia, but whether this is a general feature of all patients (children and adults) or other forms of dystonia is not known. Second, we tested only reaching movement and it is possible that patterns seen during other activities such as ambulation, speaking, eating, or isometric movements would be different. Third, we cannot determine the relationship between GPi firing and dystonic components of movement because it is not possible to separate dystonic from voluntary components of movement in our paradigm. From a theoretical point of view, our results do not shed light on the involvement of dopamine [193], sensory pathways [50, 211, 213, 215], cerebellum [72, 224, 190], or other structures in the causes of dystonia.

Despite these limitations, our results support an overall increase in GPi firing from rest to movement in children with primary dystonia. This is an important observation for understanding the nature of dystonia and the mechanism of function of interventions including medications and DBS surgery. This finding is consistent with the hypothesis that it is the pattern of GPi outputs rather than the average firing rate that is abnormal in dystonia [241, 159], and that this pattern may include both inappropriate inhibition of desired thalamic activity as well as inappropriate disinhibition of unwanted thalamic activity. Confirmation of this hypothesis in a larger cohort of patients with more varied causes of dystonia will be important for further understanding and improved treatment of this debilitating disorder. Therefore, we performed the same analysis in a larger cohort of patients with secondary dystonia and it is presented in the next chapter.

Chapter 2

Dynamic causal model to study rest-to-active phase transition in pallidum and thalamus

2.1 Abstract

The rate model of basal ganglia function predicts that muscle activity in dystonia is due to disinhibition of the thalamus resulting from decreased inhibitory input from the pallidum. We seek to test this hypothesis in children with dyskinetic cerebral palsy undergoing evaluation for deep brain stimulation (DBS) to analyze movement-related activity and phase transition from resting state to active state in different brain regions. The initial evaluation of patterns of activities in pallidum and thalamus revealed prominent alpha- and beta-band frequency peaks in the GPi, VoaVop subnuclei of the thalamus, and STN during movement but not at rest. Connectivity and phase transition analysis indicated stronger coupling between STN-VoaVop and STN-GPi compared to GPi-VoaVop. These findings contradict the

hypothesis of decreased thalamic inhibition in dystonia, suggesting that abnormal patterns of inhibition and disinhibition, rather than reduced GPi activity, contribute to the disorder. Additionally, the study implies that correcting abnormalities in GPi function may explain the effectiveness of DBS targeting the STN and GPi in treating dystonia.

2.2 Introduction

The mechanism underlying childhood dystonia is not fully understood but may include an imbalance between midbrain dopaminergic and striatal cholinergic signaling [17], abnormal patterns of subcortical activity [114], excessive basal ganglia or peripheral loop gain [205], or decreased focusing of intended patterns of muscle activity [208, 205, 207, 112]. Dystonia has been identified as the second most common movement disorder in pediatric patients [183], impacting motor function, and causing pain and discomfort. CP encompasses a heterogeneous group of developmental disorders with a movement disorder pattern that is diagnosed as dyskinetic CP [165]. Clinical goals for the treatment of dystonia involve maximizing function [122], with some non-invasive treatment options including enteral medications such as anticholinergics or muscle relaxants [232]. More recently, an overall improvement in patient outcomes has been achieved with deep brain stimulation (DBS), a method that uses implanted electrodes to modulate brain activity and signal transmission. In addition to stimulating, some leads (e.g., stereoelectroencephalography [sEEG] leads) offer the opportunity to record from human deep brain regions [174].

Several studies have reported low-frequency oscillations (LFO) in the theta and alpha bands in the globus pallidus internus (GPi) and the subthalamic nucleus (STN) for dystonia and Parkinson's disease [114]; moreover, increased beta band activity has been noted in both disorders [189, 114]. Contrary to previous studies that have focused solely on the basal ganglia (GPi or STN), we recorded from thalamic subnuclei and basal ganglia simultaneously

in awake pediatric patients with dystonia, through sEEG depth leads, as it has been recently informed to ameliorate the dystonic symptoms in adults [207]. While the pallidum (GPi) has become the main DBS target for the treatment of dystonia in children [254, 115, 52, 53], the response rates in dyskinetic CP are modest and unpredictable, with almost half of the children responding poorly [140]. Due to the limitations of pallidal DBS in dystonia, there is a need to explore alternative brain targets such as thalamic nuclei [139] or the STN [234], which are rarely targeted and thus underexplored. Selection of targets may be aided by electrophysiological data recorded from temporary (sEEG) electrodes placed at target regions. We hence collected recordings from temporary depth leads in a novel clinical procedure [132, 212, 214], which provided us the opportunity to examine LFOs across multiple deep brain regions in awake patients.

Multiple deep brain recordings allow us to not only measure the activity patterns associated with dystonia, but also understand the physiology underlying the disorder. For example, the classical basal ganglia model explains how the flow of information is regulated by deep brain regions, and it is separated into 'direct' and 'indirect' pathways [242, 6, 241, 56]. In this model, the cortico-striato-GPi path is the 'direct' pathway that facilitates movements, whereas the cortico-striatal-GPe-STN-GPi is the 'indirect' pathway that suppresses movements. This classical model has been accepted as a model for normal function and several movement disorders including parkinsonism and dystonia [56, 84]. A prediction of the model, confirmed in non-human primates, is that there is normally a high-tonic firing rate of GPi-output neurons at rest in order to suppress thalamic neurons and inhibit signals to the motor cortex that would drive movement. The model predicts that GPi output should be paused or reduced in order to perform movement, allowing activation of the thalamus [6, 172].

For dystonia, a commonly applied model is the 'rate model' of basal ganglia, which predicts that a loss or lowering of excitatory output from the STN to GPi would lower inhibitory output from GPi to the thalamus and result in excessive involuntary movements [184, 58].

Several experimental and clinical results have been at odds with this prediction, including the improvement of dystonia with pallidotomy. These and other results (as discussed in previous chapter) have led several authors to suggest that the pattern of output from GPi in dystonia is more important than the overall average firing rate, so that an inappropriate or insufficient pattern of inhibition is a cause of dystonia. It is not known if these considerations apply to children with dyskinetic CP [241, 159, 161, 160]. In order to understand the GPi function in dyskinetic CP patients, the VoaVop of the thalamus, GPi, and STN neural activities were recorded simultaneously in a group of awake children while either at rest or executing active voluntary movements with their upper limbs. Here, we aim to study the pattern of activity in these regions and explore how the connectivity gains in these regions change during a state transition from "rest" to "active". Therefore, we first performed a time-frequency analysis to confirm the abnormal activation of GPi during movement but not the resting state. We, then, fit a dynamic causal model [70] to the recordings of these regions, modeling the neuronal activity using a mean field model [169], to infer the causal connections between these regions. Thereafter, the models were evaluated and we analyzed the transfer function gains and coherence between regions to evaluate the rest-to-active phase transition in these regions.

2.3 Materials and methods

2.3.1 Patient selection and data acquisition

We selected nine patients with acquired dystonia (due to dyskinetic CP) from the DBS study cohort (patients S4-S12 in Table 1). In this study, we analyzed data from electrodes in GPi, VoaVop, and STN (and presented the data from VIM and PPN) during the voluntary

reaching task (with their upper limb) to explore the patterns of activity in these regions[1]. VoaVop is a known motor nucleus, while VIM is a sensory nucleus, and here we are focusing mainly on the motor pathways within the deep brain regions. Besides, VA (motor thalamic subnuclei) was not targeted for all patients, therefore, VIM and VA data were not used as part of this study.

2.3.2 Time-frequency analysis

We performed time frequency analysis during the voluntary reaching task in all nine children with dystonia. The method to calculate the power spectrums is elaborated in the previous chapter.

2.3.3 Dynamic causal modeling

Dynamic Causal Modeling (DCM) is a Bayesian method of model comparison to learn the dynamics of a system and infer the causal or effective connectivity between the elements in that dynamical system [70, 67]. This model is an extension of building a state space model using the empirical data, but it considers the neuronal models of activation besides the network dynamics [70, 67, 68, 54]. Additionally, it allows us to study the distribution of the neuronal population response based on a probabilistic representation of activity. In other words, it can be used to investigate the response of neural systems by looking at the neural interactions that generate those responses and it helps us to understand how the neurobiology and neural interactions generate these responses [186, 169, 168, 118].

In this study, we modeled the neural dynamics of the basal ganglia-thalamus loop using a dynamic causal model which is implemented in Statistical Parametric Mapping (SPM12, The

[1]The experiment protocol and the setup is explained in details in the general methods of this dissertation.

Wellcome Trust Centre for Neuroimaging, University College London) [65]. DCM predicts the dynamics based on the assumptions about anatomical and functional connectivity and helps to predict the synaptic properties of each connection (excitatory, inhibitory, or both) and the connection gains by fitting a neural model to the empirical data. We can employ different neuronal models to predict various network dynamics within the brain based on the neurons interactions in that region or the importance of including various receptors in our model [70, 118, 169]. For this study, we chose the mean-field model (MFM) [29] to implement the DCM; Mean field models are conductance-based models that estimate the mean activity of cell population densities by simplifying it [186, 169]. MFM is a fair assumption as it is a close model to the nature of neural populations dynamics in basal ganglia and thalamus and it models both inhibitory and excitatory cell populations. It approximates the mean activity of each population based on the fitted data and estimating the cell populations' states which include voltage and excitatory and inhibitory conductances. The explanatory equations (that are derived from Hodgkin-Huxley type neuron model [93, 94]) are elaborated here.

Mean Field Theory and Model

Mean field theory, a straightforward yet impactful technique in physics, was devised to explain various phenomena, especially phase transitions [20, 126, 149, 29]. Essentially, it involves neglecting variations and details in the interactions among the system's components, which allows for gaining reasonably accurate understanding with low computational cost. Moreover, mean field results show a limited reliance on the detailed specifics of the system, offering the potential to derive universal principles applicable to several apparently distinct sub-systems [29].

This approach is particularly relevant for analyzing neural circuits in the brain, which consist of a large number of interconnected neurons, making the mean field analysis an ideal method

for understanding this complex system [29]. The primary aim here is to identify properties of neural circuits and their transition between a "resting" state to an "active" state. These types of transitions are associated with network physiological connections within deep brain regions, and are generally not influenced by the exact [large] number of neurons, the specifics of the neuron model, or the exact values of synaptic weights [29]. Therefore, the focus often shifts to properties averaged across the spectrum of possible weights in the infinitely large networks. Such crucial properties, like the presence of a distinct phase transition, emerge only in this limitless network size [29].

The goal here is to approximate the input to a neuron with a mean field that is generated by its afferents [29]. Put simply, the assumption is that neurons in a network are subjected to an input current that matches the average input produced by their presynaptic neurons as shown schematically in Fig. 2.1. The reasoning behind this is that the input current is the aggregate of N random variables. When these variables are independent and N is large, the central limit theorem indicates that their combined distribution approaches a Gaussian distribution. Therefore, the input to a neuron i can be expressed as [29]:

$$I_i(t) = \sum_{j \neq i}^{N} J_{ij} X_j + I_{i,\text{ext}} \approx \langle I_i \rangle + \eta(t) \tag{2.1}$$

where N is the number of binary neurons $x_i \in \{0, 1\}$ that are mutually connected by synapses J_{ij} and each of them receive external input $I_{i,\text{ext}}$ from distant neurons, from other brain areas, and I_i is the input current to unit i. Note that the sum goes over all N neurons but the neuron i itself. Here the $\eta(t)$ is a Gaussian variable with stationary statistics that fluctuates in time and $\langle . \rangle$ refers to average with respect to distribution [29].

Here, the firing rate can be defined as a nonlinear function of the all the external currents

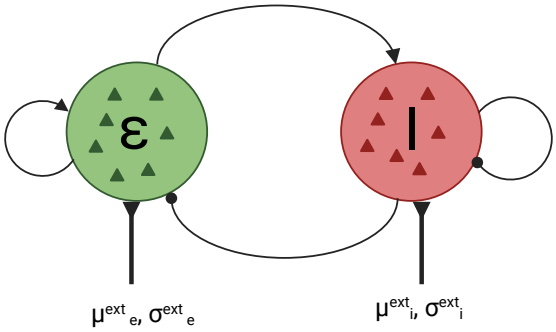

Figure 2.1: Schematic Representation of a Mean Field Model; This diagram illustrates the fundamental principle of mean field theory, showing how components of a system interact with an averaged field, simplifying complex interactions into a more general framework, where μ_e and σ_e are average and standard deviation of the excitatory population, μ_i and σ_i are the average and standard deviation of the inhibitory population, and "ext" stands for the "external input".

to a unit, $f_i(t) = \delta(I_i(t))$, thereore:

$$f_i = \delta\left(\sum_{j\neq i}^{N} J_{ij}X_j + I_{i,\text{ext}}\right) \Rightarrow f = \delta(\mathbf{J}f + I_{ext}) \tag{2.2}$$

where the vector f is the same on the left and the right hand side of the equation, and $\mathbf{J}$ is the synaptic matrix. The equation holds true because of the assumption of large number of neurons ($N \to \infty$) and considerations from law of large numbers. Here, if the neurons are identical and receive identical external current, for large N, the mean input current μ_i can be estimated as [29]:

$$\mu_i = NJf + I_{\text{ext}} \quad \text{and} \quad f = \delta(NJf + I_{\text{ext}}) \tag{2.3}$$

and the variance input current can be estimated as:

$$\sigma_i^2 \approx \frac{g^2 f}{N} \tag{2.4}$$

where $g = NJ$ is a constant, assuming that input current is proportional to N due to the scaling of J with N [29].

Ultimately, in these series of equations, the mean activity (presynaptic firing or current) is modeled by the Morris-Lecar-type differential equations (which is a simplified version of the Hodgkin-Huxley's squid axon model) [170] as the sum of conductance (C) times the voltage change $\dot{V}$ in that neural population or layer:

$$I = C\dot{V} = g(V_{rev} - V) + \Gamma \tag{2.5}$$

In this equation Γ is a unit noise, V_{rev} is the reversal potential (the membrane potential at which the current changes direction), V is the membrane potential and g is the conductance of neurons. The inhibitory or excitatory conductance rate for each layer is the product of the inverse membrane time constant $\frac{1}{K}$ and the sum of input/output conductance. This type of dynamic allows for nonlinearity in the dynamic model and enables us to evaluate neural connections [169, 168, 69, 54].

2.3.4 Model setup

We used the intracranial recordings of GPi, VoaVop, and STN during the voluntary reaching task. We, then, built seven different DCM using SPM to predict the change in the strength of connectivity and coupling gain between each two pairs of subnuclei, during the transition

from rest to the active state. Each source (GPi, VoaVop, or STN) was fit to a MFM which models the inhibitory and excitatory connections within each of the subnuclei. These seven fitted models are shown in Fig. 2.3 (a). All the models are build based on the known connections between these three subnuclei. We wanted to confirm if DCM is able to predict how these connections change during active state versus resting state. We assumed all the inhibitory and excitatory connections can be modulated during the phase transition from rest to active movement (red dots in Fig. 2.3 (a)). We then used a Bayesian comparison method (built-in SPM) to compare which model has the highest probability to be true given the empirical data [68, 67, 195, 69].

2.4 Results

2.4.1 Time-frequency analysis

We performed time-frequency analysis for all nine patients in this study. The method is similar to the methods explained in the previous chapter. The time-frequency analysis in this study, yielded similar results, indicating increased activity of GPi during voluntary movement. To illustrate our results, the EMGs of the biceps, triceps, wrist flexor, and extensor during the voluntary reaching task for four trials are shown in the top four plots of Fig. 2.2 (a), for one subject. On the bottom row of the same subfigure, the sum of the EMGs are shown, representing a pattern of activation of all muscles during the voluntary reaching task. This output signal is correlated with the generated muscle torques as the EMGs are filtered using a nonlinear Bayesian filter (representing envelope of EMGs), highlighting the changes in muscle activity as well as the activation itself. Our results demonstrate that there exists higher correlation between the EMG and the motor-subnuclei of the deep brain regions, including GPi, VoaVop, VA, and STN compared to other regions (VIM and/or

PPN) as illustrated in Fig. 2.2 (b) and (c). This correlation indicates that the motor nuclei in the brain regions activate during movement, and they are less active during the rest. The comparison of all the frequency bands in these subnuclei yielded the same result. As shown in Fig. 2.2 (c), this correlation of activity with the EMG can be seen more or less in GPi, especially in theta [4-8 Hz], alpha [8-12 Hz], and beta [12-30 Hz] frequency bands.

We then explored the correlation between the motor subnuclei activation average power in five frequency bands up to 1000 Hz with either the EMG or derivative of the EMG which is a measure of movement onset and offset or torque. The results demonstrate that there exists higher correlation ($p - value < 0.05$) between the EMG, itself, and the motor-subnuclei of the deep brain regions (GPi, VoaVop, VA, and STN) compared to other regions (VIM and PPN), regardless of the frequency band. Comparison of correlation coefficients of the power in five frequency ranges (color coded) with EMG recordings and the derivative of EMG recordings, in motor subnuclei is depicted in 2.2 (d). The Pearson correlation coefficients are computed for all and the ones that are significantly different from zero are marked with **.

2.4.2 DCM results

Although the cortex-basal ganglia-thalamic anatomic connectivity is widely known, We sought to test the transmission of information through this loop to determine which pathways are having the greatest modulatory influence during the reaching task. To do this, we tested a total of seven possible connectivity models with inhibitory, excitatory, and mixed excitatory and inhibitory projections as shown in Fig. 2.3 (a). Models were selected to encompass several plausible connections between structures. Note that connections represent flow of coherent information, but not necessarily a direct or monosynaptic connection between regions. For example, there may not be a direct anatomic connection between STN and

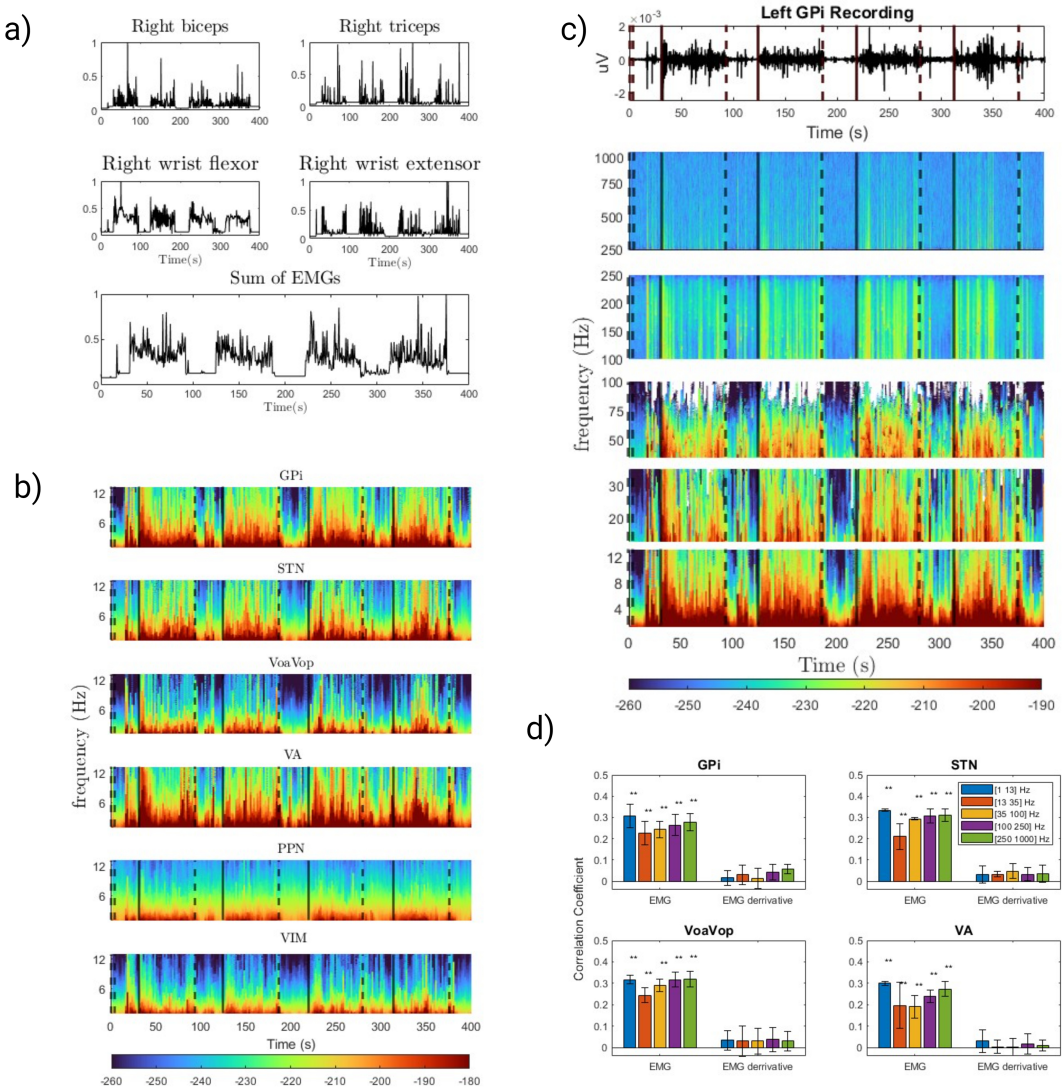

Figure 2.2: a) EMGs of the biceps, triceps, wrist flexor, and extensor and their sum during the voluntary reaching task during four trials, for one subject; b) Corresponding, contralateral, low frequency spectrogram of GPi, STN, VoaVop, VA, PPN, and VIM during the same trial. The vertical solid black lines on the spectrograms indicate the onset of the movement, and the dashed vertical black lines indicate the onset of resting period. All the motor nuclei (GPi, STN, VoaVop, and VA) have higher activity during the movement compared to rest, in theta and alpha frequency bands; c) (Top) Raw signal of Gpi recording, and (Bottom) the spectrograms of Gpi in frequencies from 1 Hz to 1 kHz (5 bands). GPi has higher activity during the movement compared to rest, in all frequency bands; d) Statistical results confirming the increased and correlated activity in all motor nuclei.

VoaVop, however, functional connectivity could be mediated through regions connected to both nuclei such as pallidum and/or cortex. We included modulatory effects (how movement

affects the connections between structures during phase transition) for all excitatory and inhibitory projections. The model's connectivity structure and parameter values constitute the system's transfer functions, which are used to generate predicted cross-spectra between regions, for comparison with the observed spectra. Conditional expectations are given by variational Bayesian inference under the Laplace approximation, such that free energy serves as an approximation for log-model evidence [68, 67, 195, 69]. Based on the assumption that lowest free energy estimates yielded valid results, the first model was the best model with the highest log-evidence depicted in Fig. 2.3 (b). Additionally, the a-posteriori probability of each of the model was computed to confirm the best model. Hence, the first model was selected with the highest posterior confidence, depicted in Fig. 2.3 (c).

The effects of movement on excitatory and inhibitory connections (known as extrinsic coupling strengths) with their probabilities (0 to 1 values, gray scale) which represent the modulatory effects of movement are shown in Fig. 2.4. The strongest excitatory connections are from VoaVop to STN, from STN to GPi, and from STN to VoaVop, while the most prominent inhibitory connections are from GPi to VoaVop, as expected. The largest effect of movement is predicted to be on the STN-VoaVop and STN-GPi connections (probability > 0.8). The modulatory effect on the connections are measured by the transfer function gains between each two structures. Using the first model, we calculated the gain coefficients (here ranked from 0 to 5) to determine the change in connection strength due to modulation by movement (transition from rest to active state). The gains obtained from the active state for all connections were normalized to resting state gains (defined with the value = 1), showing increase or decrease from the resting state for each connection as illustrated in Fig. 2.5. The strongest effects are appear to be from STN to VoaVop, and from STN to GPi, with values up to 4 times higher than those for resting state. The less strong effects are on the connections from GPi to VoaVop or from VoaVop to STN, with values below or close to the resting state.

The absolute cross-spectra between each regions are shown in Fig. 2.6 (a) and (b). This

figure represents both the model prediction of cross spectra and the real data in two states: resting (Fig. 2.6 (a)) and active (Fig. 2.6 (b)). Model predictions of the pairwise coherence functions between each two regions (ranked from 0-1) are also presented in Fig. 2.6 (c). Brain recordings from GPi and VoaVop show peak coherences ($\sim$ 15 Hz) in the beta-band, with significant differences from resting signals. Moreover, STN-VoaVop and STN-GPi show peak coherence in the beta-band principally, with coherence values of approximately 0.3 and 0.5. Please note that the coherence is a metric to evaluate the extent of signal transmission and information flow between two regions at those specific frequencies; while the gain coefficients are the metrics that show the transfer function gain between these two regions, representing the extent of signal amplification. Therefore, one cannot be concluded from the other.

2.5 Discussion

The basal ganglia compose a complex system that sends and receives feedback to the cortex through the thalamus and striatum. The STN and the striatum receive cortical inputs, while the GPi sends information to the thalamus, which in turn modulates cortical activity. The "rate model" of basal ganglia [241] suggests that high activity in the GPi is required to inhibit movement at rest. In particular, the rate model postulates that increased movement in dystonia is due to low-firing rates in the GPi. However, the alterations of this circuit resulting in dystonic muscle contractions are still not fully understood. Our surgical procedure [132] allows us to simultaneously record from multiple targets in awake patients without the influence of anesthesia. Therefore, it enables us to record valuable and useful data and to address some questions such as: 1) which frequency bands are associated with movement for each targeted deep brain region in dyskinetic CP, and 2) whether the results are consistent with the predictions of the 'rate model' of basal ganglia in dyskinetic CP.

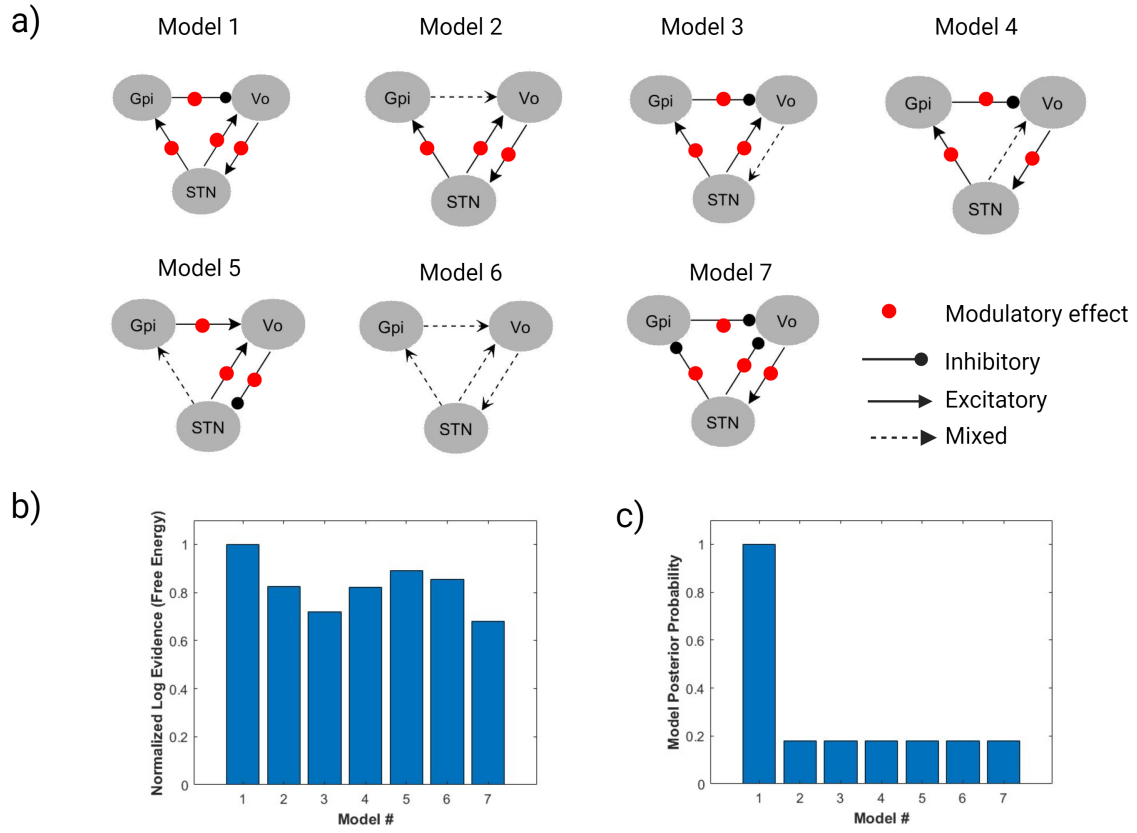

Figure 2.3: a) Schematic of the tested dynamic models to fit the empirical data and perform the Bayesian comparison on. Seven models were tested in this study. b) All models were compared using the free energy estimate of model evidence (the first model (model 1) had the highest log-evidence, $p < 0.05$); c) Posterior model probability to corroborate the best model, reveals that the first model has the highest likelihood to represent the empirical data and causal connections.

2.5.1 Frequency patterns in dyskinetic CP

A characterization of frequency patterns in dyskinetic CP is crucial to understanding the underlying dysfunction in children with dystonia. Previous studies have focused on frequency patterns in the pallidum in patients with clinically successful outcome [221, 228, 36, 41], and have shed light on the pathophysiology of dystonia, observing bursting cells in the GPi (observed from single-unit recordings during DBS surgery [164]) and theta band activity in both the GPi [174] and the STN in patients with dystonia [74]. However, the role of the pallidum in the pathophysiology of dystonia is still unknown. One theory suggests that

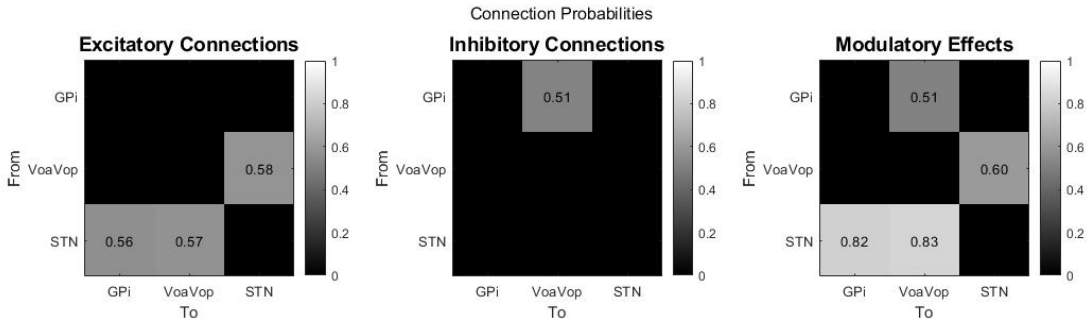

Figure 2.4: The predicted conditional probability of the strongest functional excitations, VoaVop to STN, STN to GPi, and STN to VoaVop, are shown in the left figure. The conditional probability of the functional inhibition from the GPi to VoaVop is presented in the middle figure. The conditional probabilities of the modulation of each of these connections are shown in the right hand figure with the largest effects on STN to VoaVop,and to GPi connections (probability > 0.8).

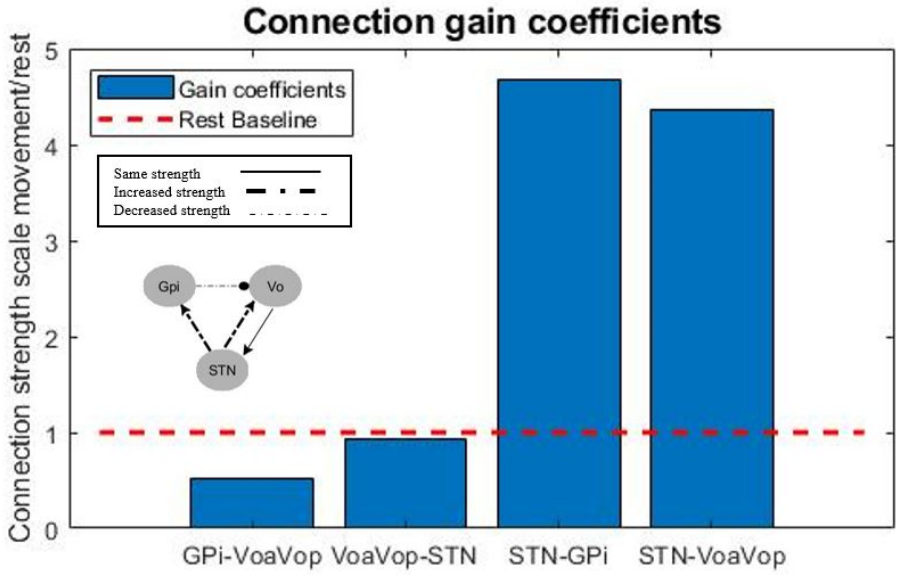

Figure 2.5: Estimation of coupling strength among the three structures analyzed for the first model, in terms of gain coefficients. Transfer function gain coefficients were normalized to the resting state (red dashed line) to predict the effect of movement relative to the resting state. The impact of movement on functional connectivity is shown, with major effects observed as increased strength (bold black dashed lines) from STN to VoaVop and from STN to GPi. Movement was observed to decrease the functional inhibition strength between GPi and VoaVop (gray dashed line).

dystonic muscle contractions may be caused by excessive gain in the cortex-basal ganglia-thalamic loop, impacting motor network function [200, 151]. Additionally, there is growing

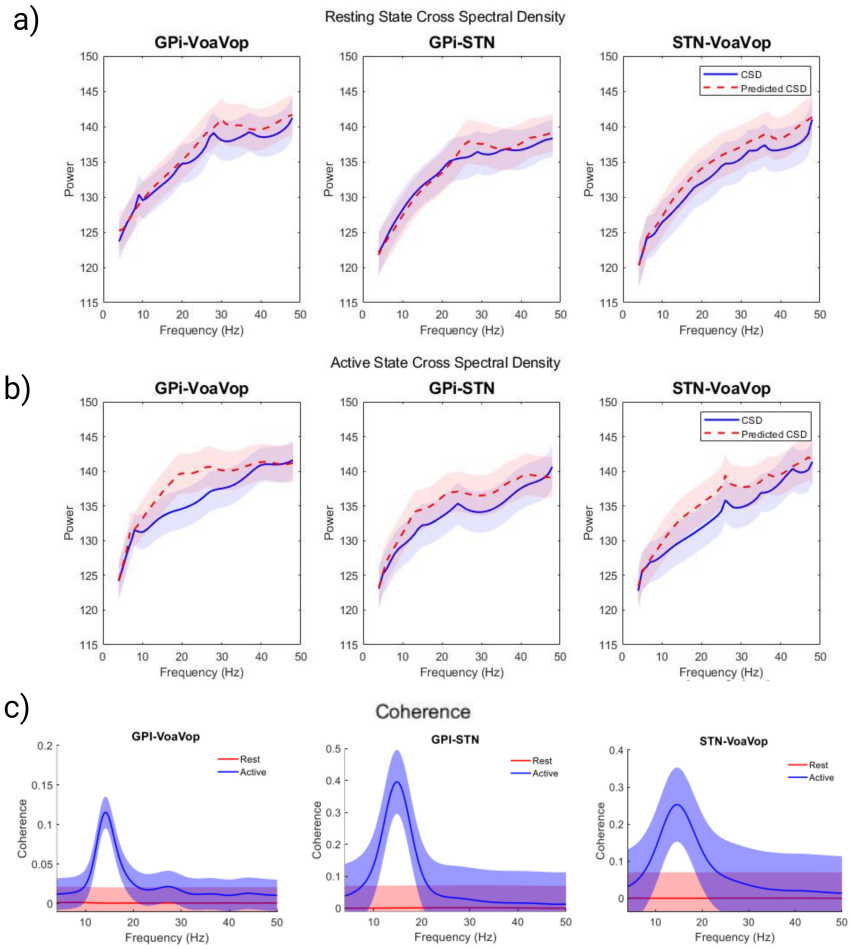

Figure 2.6: a) Resting state cross spectral density for each connection (solid blue line) and the model prediction (dashed red line); b) Active state cross spectral density for each connection (solid blue line) and the model prediction (dashed red line); c) Coherence analysis; Depicts the relationships between signals as a coherence function on the spectra for GPi-VoaVop, GPi-STN and STN-VoaVop.

evidence of the involvement of other brain regions, such as the cerebellum [91, 67, 114], and the sensorimotor cortex [175]. The presence of peaks in theta, alpha and beta bands in the pallidum could be significant to the pathophysiology of dystonia. In line with previous findings [174], our results show activity in all these bands; however, across patients, the most distinct peak during voluntary movement was in the low beta band (maximum peak at ∼13 Hz). Since the STN receives input from the cortex via the hyperdirect pathway, we expected to see power across a wide frequency range during movement, which our results (Fig. 2.2)

confirmed. Beta-band peaks were also noted in thalamic subnuclei, though less pronounced than those in the pallidum, and with detectable differences from those observed at rest. While the major power in thalamic recordings is in the beta band, there is also power at higher frequencies ($> 30Hz$) (Fig. 2.2 (C) and (D)). Similar to observations in the pallidum and thalamus, the major power in the STN is concentrated in the beta band. These findings lead us to believe that the signal transmission in the beta band (around 13 Hz) triggered by movement is maintained across all structures from the STN to the GPi and from the GPi to VoaVop, with detectable differences in magnitude between areas of connectivity, as shown in Fig. 2.2 (b).

In conclusion, despite the presence of both excitatory and inhibitory connections between regions, all regions are active during movement, consistent with modulation of patterns of activity within each region, rather than modulation of the overall activity of the regions. This could be a biomarker of dystonia and it requires further study.

2.5.2 Functional connections and rest-to-active state phase transition

Based on the basal ganglia model, the GPi-VoaVop connection is expected to have the highest magnitude with a negative (inhibitory) correlation [222]. However, Fig. 2.5 shows that the strongest connections are between the STN-GPi and STN-VoaVop. On one hand, the basal ganglia, particularly the GPi-STN, exhibit higher magnitudes than the thalamus during movement, suggesting that the basal ganglia modulate the thalamic output [131]. On the other hand, although there is no direct anatomical connection between the STN and VoaVop, their coherence exhibits a higher magnitude than that of GPi-VoaVop. Therefore, these results are inconsistent with the theory of thalamo-cortical disinhibition due to decreased output from the GPi [241].

Our results, confirm current hypotheses of the classical model of the basal ganglia. In particular, we have confirmed the inhibitory connection of the pallidum on the thalamus, and we have also confirmed the expected excitatory effect of STN on pallidum. More surprisingly, we have shown a strong bidirectional functional excitation between STN and motor thalamus. This functional excitation is clearly shown by the results from the free energy estimates (Fig. 2.3 (b) and (c)). Additionally, the results are consistent in explaining how voluntary movement is associated with changes in the transmission of information through the basal ganglia and thalamus. This functional excitation is probably mediated through other brain regions including the cortex, since there is currently no evidence for a direct excitatory connection from STN to the thalamus in humans.

Assuming that there is not a direct anatomic connection between STN and VoaVop, we conjecture that there is inappropriate thalamic excitation as a result of an input from the cortex, which in turn activates downstream STN via the hyperdirect pathway, increasing STN activity. STN in turn excites GPi, resulting in increased activity in GPi during movement but not high enough to inhibit the existing thalamus excitation. GPi outputs 'sculpt' ongoing activity in the thalamus, providing a functional increase in both the thalamus and STN through cortex inputs. Recordings from non-human primates and Parkinson's disease have been consistent with the hypothesis of high GPi activity at rest [6, 172, 173]. Our results, however, differ significantly, as previously reported [91]. One possible explanation is that the function and connectivity of GPi are significantly different in children with dyskinetic CP. Another possibility is that the nature of our recordings, performed in pediatric patients that are unrestrained and comfortable in a hospital bed, allows for true relaxation, whereas non-human primates are not in fact at rest while restrained in an electrophysiology recording apparatus. It is also possible that the high levels of activity seen in Parkinson's disease [131] represent a significant abnormality that is not present in dystonia. We observed strong movement-related modulations in both STN and VoaVop, despite the lack of evidence for direct interactions between these two nuclei from animal models [154]. Excitatory inputs

from the motor cortex may explain these results and suggest a mechanism for the effectiveness of deep brain stimulation in STN [64] and GPi [36] to treat dystonia.

The DCM analysis confirmed the inhibitory connection between GPi and motor thalamus. In addition, our results from frequency analysis clearly show increased activity in both regions during movement compared to during rest. We reconcile these two apparently contradictory findings by proposing that GPi inhibits a subpopulation of thalamic neurons, whereas most of the thalamic target neurons must be excited from other sources (probably cortical inputs). Therefore, our findings are consistent with the hypothesis that GPi outputs 'sculpt' ongoing activity in the thalamus and thereby perform precision modulation of the signal returning to motor cortical areas. This hypothesis is consistent with prior models of the control of motor patterns [241, 159]. Our results provide support for a more complex model of basal ganglia function that may be helpful to understand the mechanism of dystonia and offer potential new treatments.

2.6 Conclusion

The presented results from chapters 1 and 2 provide information on the pattern of activity and functional connectivity between regions in basal ganglia and thalamus in children with secondary dystonia. Further studies are required to determine which components of the observed activity are responsible for dystonia, which one represents compensation for dystonia, and which one represents normal patterns. Nevertheless, the importance of these regions as targets for deep brain stimulation implies that a detailed understanding of the activity patterns can be helpful to elucidate the mechanism of deep brain stimulation and for the clinical selection of appropriate targets. In the next chapters, we explore the correlation of functional connectivity and these patterns with the anatomical measures from tractography, as well as the effect of stimulation on these patterns of activation.

Chapter 3

Exogenous brain stimulation pulses are carried along the motor pathways from pallidum to distant targets

3.1 Abstract

Deep brain stimulation (DBS) is a neuromodulation method for treatment of various neurological disorders. It is often assumed that the primary inhibition or excitation effect of DBS occurs at the site of stimulation. However, recent work has shown that DBS can lead to robust evoked potentials (EP) not only at the stimulation site, representing the local effect, but also in multiple distant brain regions, representing the effects on distant targets. While the significance of these EPs for therapeutic outcomes is not known, it appears that the electrical effects of DBS have at least a partial modulatory impact on downstream targets. Nonetheless, it remains unclear through what mechanism DBS pulses travel to the distant targets or what portion of the pulses travel along the normal pathways from the stimula-

tion site to the distant target(s). The possible scenarios include, but are not limited to, orthodromic or antidromic pathways, accessory pathways, normally inhibited pathways, and direct electromagnetic activation of distant sites. The ability to record signals from brain regions with DBS on and off provides an opportunity to determine the mechanism of DBS signal transmission. We hypothesize that the pathways that transmit DBS pulses include the pathways that transmit intrinsic neural signals. To test this hypothesis, we performed a transfer function analysis on deep brain recordings during DBS-off condition and compared its impulse response with the transmission of signals from electrical stimulation during DBS-on condition. Our results support our claim that the electrical pulses travel partly along intrinsic motor pathways by showing that the propagation of DBS signals can be partially predicted by observation of intrinsic neural activity and measurement of DBS-evoked responses can partially predict normal pathways of neural communication.

3.2 Introduction

DBS is a neuromodulation technique that involves implantation of depth electrodes at potential targets in the brain, through which electrical pulses are administered to modulate neuronal activity [4]. It has been shown that DBS is an effective treatment of various movement and neurological disorders [127], including Parkinson's disease [181], dystonia [207], essential tremor [143], epilepsy [250], and Alzheimer's disease [152]. Additionally, recent advancements show that DBS can be used for the treatment of psychological conditions such as obsessive compulsive disorder [148] and major depressive disorder [55]. Despite recent advancements in clinical applications of DBS and its widespread adoption, its underlying mechanism remains poorly understood [207, 38, 206, 187, 233]; however, several models have been proposed by researchers on the mechanism of DBS, including the "inhibition hypothesis", "excitation hypothesis", and the "disruption hypothesis" [38, 39, 166, 156].

Previous research on the mechanism of DBS indicates that DBS effect is similar to those produced by micro-lesions in the brain [137, 136, 243, 83], which has led to the replacement of lesion-therapy by DBS [39]. The observed similarity suggested that DBS might inhibit local circuits. Although suppression of neuronal activity in the vicinity of the stimulated region was noted, the "inhibition hypothesis" has been called into question by the detection of DBS-evoked responses (EPs) in distant targets [39].

Other studies have confirmed that GPi-DBS directly induces spiking activity in the GPi neurons, which activates the GABA-ergic (inhibitory) projections onto the thalamic regions. This results in inhibition of those downstream targets, supporting the "excitation hypothesis" of the DBS effect [240, 82, 59, 39]. However, this hypothesis was rejected by more recent observations of induced multiphasic responses, consisting of both excitation and inhibition, during GPi-DBS, in the GPi of monkeys with Parkinson's disease [15, 60, 153].

More recently, it has been shown that GPi-DBS during the cortical stimulation inhibits the cortical evoked responses by strong GABAergic inhibition. This suggests that GPi-DBS blocks the information flow through GPi itself, supporting the "disruption hypothesis" [39, 37]. The presented evidences along with other examples [167, 57, 7] suggest that DBS essentially blocks the signal transmission from the input to the output of inhibitory or excitatory pathways, resulting in dissociation of input and output [39], rather than having a sole excitatory or inhibitory effect on the downstream regions [39, 37]. This indicates that DBS impact extends beyond its immediate vicinity, with its global influence on distant targets being demonstrated through the recorded evoked potentials (EPs). DBS pulses propagate in a specific pattern as evident by the EPs; However, the precise mechanism of propagation and the pulse transmission pathways are not known. Here, we propose a transfer function method to identify what portion of the DBS pulses travel along the neural pathways that carry the intrinsic neural signals.

Identifying the DBS signal pathways is essential for computational modeling and direct mea-

surement of the effects of DBS on brain networks [155]. While anatomic evidence from non-invasive technologies such as diffusion tensor imaging (DTI) is available, this provides only indirect support for anatomical connectivity and is not sufficient for assessing the functional connectivity [138]. Direct measurement is required to learn about the signal transmission along these pathways. Noted that, evidence for the presence of a pathway and the presence of intrinsic signal correlations at either end of that pathway is not sufficient to establish causality or the direction of signal transmission. One way to map DBS pulse transmission in deep brain networks is to stimulate in one region and measure its effect on distant targets [229]. However, electrical stimulation is an un-natural and non-physiological input to the brain. It non-selectively activates and depolarizes a wide group of neurons that would be much more selectively activated in physiology, therefore, essentially, its mechanism of transmission can be very different from that of the intrinsic neural signals. DBS pulses can travel from the source to the target through many pathways, including "normal" (orthodromic) pathways, antidromic pathways, accessory pathways that would not normally be active [206], and direct electromagnetic activation of distant sites (as supported by measuring the volume of tissue activated [VTA] which is partially predictive of the widespread neural effects of stimulation) [11]. Alternative mechanisms also include activation of pathways that are normally inhibited [39], those with high threshold, or those that are not accessible to stimulation, including polysynaptic pathways [39].

Considering everything mentioned, it has not been studied if the intrinsic motor signals and the DBS pulses are carried to distant targets through the same mechanism. If they do, what portion of the pathway is directly affected by the DBS pulse, whether it is an orthodromic or antidromic pathway. To distinguish various possibilities, we compared the transmission of DBS pulses to a transfer function representation of intrinsic neural signals (DBS-off local field potentials [LFPs]), at two ends of a known anatomical pathway. The estimated transfer function does not indicate causality, because empirical transfer functions are bi-directional in nature and the causation flow is not clear [35, 78]. Nevertheless, we can set the input and

output of the system based on the evidence of physiological connections [123, 39] and extract useful information based on those presumptions. The study methodology was designed to determine whether the normal pathways carry the DBS pulses or the DBS pulses are affecting the distant targets through other mechanisms. We hypothesize that the distant effects of DBS are most likely due to direct transmission of the DBS pulse, perhaps through depolarization of local axons) rather than propagation of locally-evoked activity to distant sites.

To test our hypothesis, we made use of intracranial brain recordings (LFP) from Stereoelectroencephalography (sEEG) leads [116], which are used in surgeries for treatment of various neurological disorders, including epilepsy [246, 250], Parkinson's disease [152], and dystonia [207, 212, 132]. The sEEG leads were implanted into potential DBS targets, as part of the clinical evaluation for implantation of permanent DBS electrodes in deep brain regions of 7 children and young adults with dystonia [206, 212, 207]. This was followed by one week of extensive tests and recordings in an inpatient neuromodulation monitoring unit (NMU) with the clinical goal of finding the ideal target region(s) for each patient's permanent DBS lead(s) [212, 132]. Clinical evaluation focused on capturing evoked responses in ventral oralis anterior/posterior (VoaVop) and ventral anterior (VA) subnuclei of thalamus, and subthalamic nucleus (STN) during stimulation in globus pallidus internus (GPi), as well as the responses in GPi due to stimulations in VoaVop, VA, and STN [in separate trials]. Clinical data also included recordings of the LFPs during a voluntary reaching task, while stimulation was off (DBS-off).

If a significant fraction of the variance of the evoked response from the DBS pulses can be explained by a transfer function computed using the intrinsic neural signals, we can claim that DBS pulses travel primarily by the physiologically used intrinsic neural signal pathways, most likely through the same mechanism. Additionally, if that is the case, we hypothesize that the fraction of variance in EP explained by the response of the estimated transfer function should be significantly higher in the orthodromic direction than in the antidromic

direction, as there intrinsic signals do not travel antidromically. This further supports our hypothesis that the stimulation pulses are primarily transmitted by a mechanism similar to that of intrinsic neural signals.

3.3 Materials and methods

3.3.1 Data

The data from seven patients (S2, S3, S13-s17 in Table 1) were analyzed in this study. The activity in GPi, STN, VO, and VA were simultaneously recorded within 24 to 96 hours after surgery in two modes: 1) While the stimulation was off, and the patient was performing a voluntary reaching task with the upper limb contralateral to LFP recordings (intrinsic neural signals; DBS-off condition). 2) while the patient was at rest and unilateral stimulation was on (DBS-on condition). Approximately 1200 DBS pulses were administered through two adjacent macro-contacts (anode and cathode) at a time, with 90-µs bandwidth and 3-V voltage at 25 Hz, to each nuclei separately, eliciting DBS evoked potentials [EPs]. Figure 3.1b depicts a simplified schematic of the stimulation target (input) and the recording target (output) for each of the EP recordings in this study. Please note that the stimulation at each of these targets elicit EPs in other areas of the brain, not shown in the here. For example, STN-DBS activates the lenticular fasciculus through activation of hyper direct pathway and provides direct inputs to the thalamic nuclei [39, 162]. However, in this study we are only considering the efferent and afferent pathways to GPi due to its proven efficacy and importance in improvement of dystonic symptoms in our patient cohort [207]. Moreover, in order to reduce the stimulation artifacts, we stimulated through each contact pair in two trials, with the cathode and anode switched, both of which are located in the same subnuclei; therefore, stimulating the similar population of neurons. When the resulting signals are added, the

opposite artifact polarities cancel out while the evoked response polarity is augmented. The experimental protocol, movement-LFP synchronization, and the stimualation protocol are detailed in the general methods of this dissertation and previously published works [239].

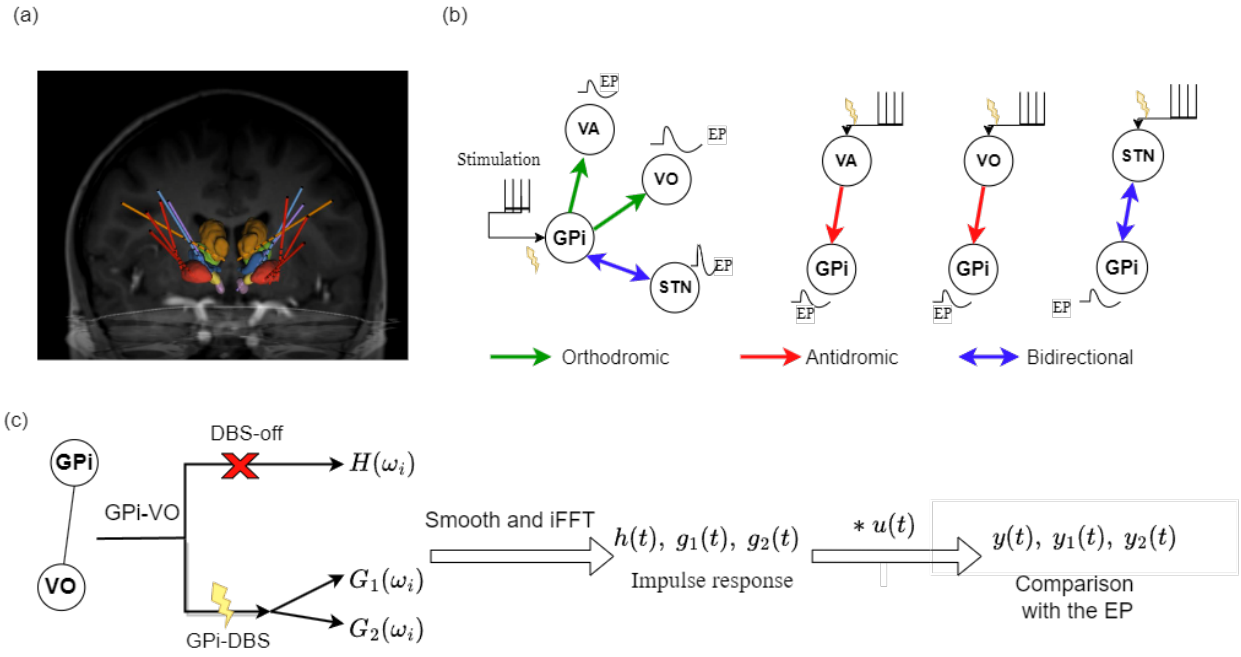

Figure 3.1: a) Frontal view of the DBS leads and the segmented regions in one patient; b) Schematic of all recording and stimulation targets when stimulation is administered in one target, separately. Please note that this is a simplified illustration of the pathways and EPs that we used for our analysis and does not imply the precise pattern of EPs due to stimualtion; c) Highlights the pipeline of transfer functions computations and comparisons for one pathway connecting the GPi and VoaVop electrodes. Note that GPi to VoaVop is orthodromic and VoaVop to GPi is antidromic and we computed three transfer functions, $H(\omega_i)$, $G_1(\omega_i)$, and $G_2(\omega_i)$, for each direction and performed pairwise comparison between their responses, $y(t)$, $y_1(t)$, and $y_2(t)$.

3.3.2 Data analysis

All data preprocessing and analysis were done in MATLAB R2021a (The MathWorks, Inc., Natick, MA, USA).

Data Preprocessing:

After applying the preprocessing steps (explained in general methods) the DBS-off LFPs signals that were recorded during the DBS-off condition were then split into ∼50 two-second segments. On the other hand, LFPs obtained during stimulation underwent another processing step to eliminate stimulation artifacts, which subsequently leads to detection of EPs.

DBS artifact removal. After upsampling the DBS-on bipolar recordings to 120 kHz, the accurate stimulus artifacts peaks were located using the 'findpeaks' function in MATLAB. The signals were then split into 11-ms segments starting from 1 ms prior to stimulus onset (stimulus artifact). Outlier segments were labeled and removed from the data if the artifact amplitude was not within their ±3 standard deviations. All the remaining segments were subsequently aligned through cross-correlation of time-0 artifacts. This resulted in approximately 1000 segments per stimulus location, which were finally averaged to increase signal-to-noise ratio [226]. The stimulus-triggered averaging methodology presented by Nicholas C. Sinclair et al 2019 [226] was repeated for both sets of polarity reversed stimulation settings, which were finally aligned to produce a polarity-reversed average with smaller stimulus and decay artifacts [239, 90, 216], as shown in Figure 3.2.

Transfer Function Computation:

In order to determine whether DBS pulses travel via the same pathways that carry intrinsic neural signals, we compared the DBS EPs with the impulse response of a system defined during DBS-off condition, between the same two points in the brain. In other words, we compared the response at a distant region elicited by DBS at the stimulation site with the impulse response of a transfer function between the stimulation site and the distant region in the absence of DBS (DBS-off condition). Transfer functions are specified in the frequency domain, while evoked potentials are specified in the time domain; therefore, we

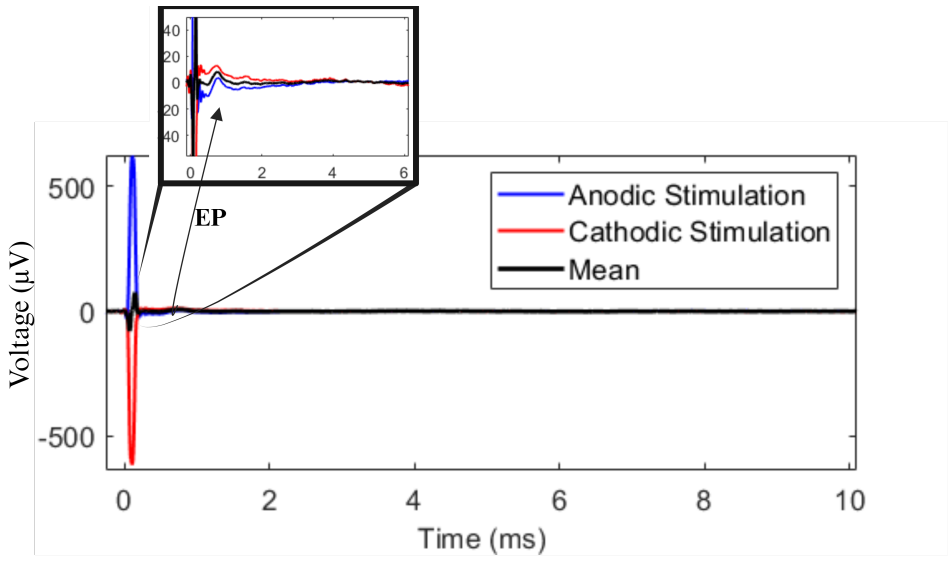

Figure 3.2: The mean responses of anodic and cathodic stimulation segments are shown in blue and red lines. Their average (black line) cancels out the artifact resulting in smaller decay and stimulus and increasing the signal to noise ratio. The figure is zoomed in in voltage axis and time axis and reveals the actual EP at time $\sim 1ms$.

inter-converted the time and frequency domains using Fourier transform (FFT) analysis and performed comparisons in time domain [150]. The method pipeline is depicted in Figure 3.1c.

Intrinsic neural signals transfer function computation. We computed the empirical transfer function estimate (ETFE), $\tilde{H}(\omega_i)$, from one end of a pathway (input X) to the other end of a pathway (output Y), for each 2-second segment of preprocessed DBS-off intrinsic neural recordings, resulting in 50 distinct DBS-off transfer functions per patient. See Figure 3.3a for a schematic representation of the system. In this linear time invariant (LTI) system , $\tilde{H}(\omega_i)$ is given by

$$\tilde{H}(\omega_i) = \frac{Y(\omega_i)}{X(\omega_i)}. \tag{3.1}$$

In this equation, $Y(\omega_i)$ is the FFTof the output signal and $X(\omega_i)$ is FFT of the input signal at frequency ω_i and $H(\omega_i)$ is the transfer function at that frequency [150]. This transfer function is a vector of complex numbers that indicates the gain (amplification) and the phase shift of the input at each frequency, ω_i [150].

DBS EPs transfer function computation. Using the DBS EPs, we computed two additional transfer functions to investigate whether the target EPs result directly from the DBS signal, or from transmission of local responses of neural tissue near the stimulating electrode. The first case would correspond to DBS depolarization of nearby efferent axons, while the second case would correspond to DBS depolarization of nearby neural cell bodies with subsequent propagation of EP from the stimulation site to the distant target [39, 7, 252, 11]. Therefore, we considered these two cases, in which (a) G_1 is a transfer function with the stimulation itself as the system input, $u_1(t)$, as shown in Figure 3.3b, and (b) G_2 is a transfer function with the stimulation-site's EP as its input, $u_2(t)$, as shown in Figure 3.3c. In both cases, the output is considered to be the distant target's EP, $y_1(t)$ and $y_2(t)$. Thus, G_1 is calculated as the ratio of distant target's EP FFT and the stimulation signal's FFT; and G_2 is calculated as the ratio of the distant target's EP FFT and the stimulation site's EP FFT.

It is worth noting that although the window sizes for DBS EP and intrinsic LFP signals differ (10 ms versus 2 s), this disparity does not influence the final results. The EP window size represents an average of 1000 segments, resulting in enhanced signal smoothness. We selected a window size of 2 seconds for the intrinsic LFP signals to achieve higher frequency domain resolution and greater clarity when calculating the impulse responses and ETFEs. We then compared the EPs and impulse responses solely for the duration of the response, which is 5 ms. The computed spectral estimates of the intrinsic neural signals (DBS-off condition) transfer functions alter drastically in higher frequencies because the ETFE variance does not diminish with large numbers of samples (Figure 3.4 top). Therefore, we utilized a smoothing

method to smooth out the ETFE [78, 22].

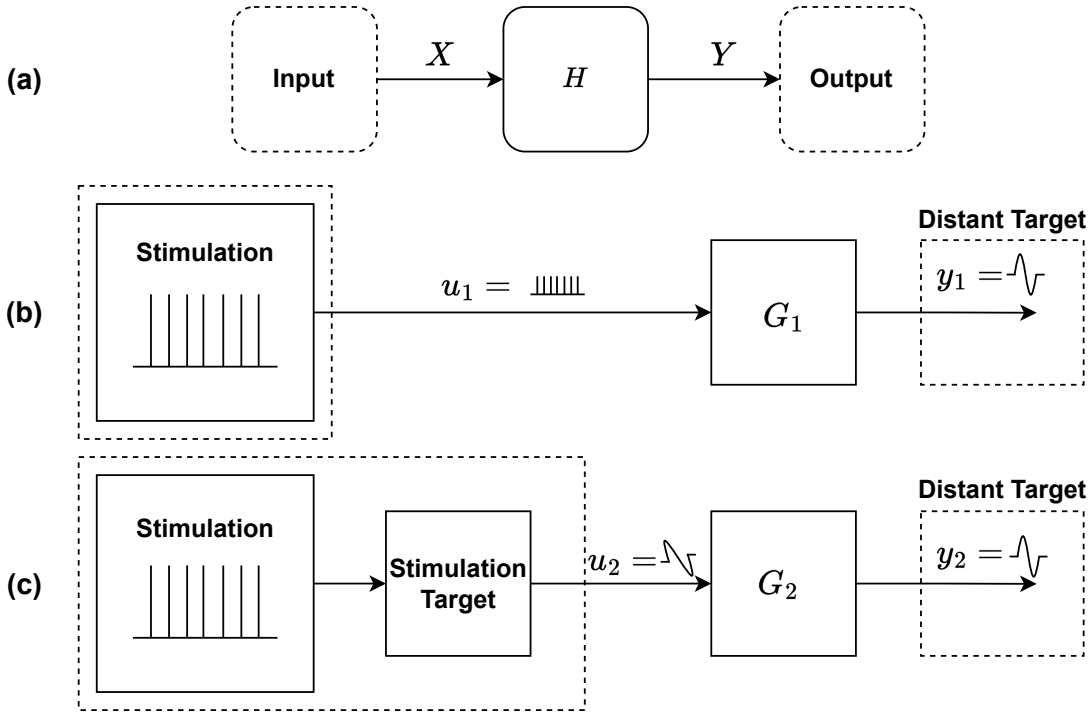

Figure 3.3: Schematic for the pathways system transfer function: a) Intrinsic neural signal pathway system schematic, where one end of the pathways is the system input and the other end is the system output. b) Direct stimulation of efferent axons by DBS stimulation.; and c) Stimulation of local neurons by DBS, with propagation of the subsequent signal to the target. In case (b), we expect the shape of the DBS signal to be the best predictor of the target response. In case (c), we expect the shape of the local EP at the stimulation site to be the best predictor of the target response.

Transfer function smoothing:

Local linear kernel smoothing regression was used to smooth the ETFEs in the frequency domain by solving a weighted least-squares (WLS) problem. The local linear estimator can be obtained by [78, 22, 42, 230]:

$$H(\omega_0) = \frac{1}{N} \frac{\sum_{i=1}^{N} (S_2 - (\omega_0 - \omega_i)^T S_1) K(\frac{\omega_0 - \omega_i}{h}) \tilde{H}(\omega_i)}{S_2 S_0 - S_1^2}. \tag{3.2}$$

Here, $H(\omega_0)$ is the smoothed transfer function, $\tilde{H}(\omega_i)$ is the non-smoothed transfer function estimate at ω_i, N is the number of samples, $K(\frac{\omega_0-\omega_i}{h})$ is the Gaussian kernel function, $K(z) = exp(-\frac{z^2}{\sqrt{2\pi}})$, with the bandwidth of $h = 50\ Hz$, and S_i is given by:

$$S_i = \frac{1}{N}\sum_{i=1}^{N}(\omega_0 - \omega_i)^i K(\frac{\omega_0 - \omega_i}{h}). \tag{3.3}$$

The smoothed ETFE serves as an asymptotically unbiased estimator of the frequency response function [78]. Figure 3.4 shows an example of Bode magnitude plot of the estimated and the smoothed intrinsic neural signals' transfer function (top) and an example of G_1 DBS EPs transfer function (bottom).

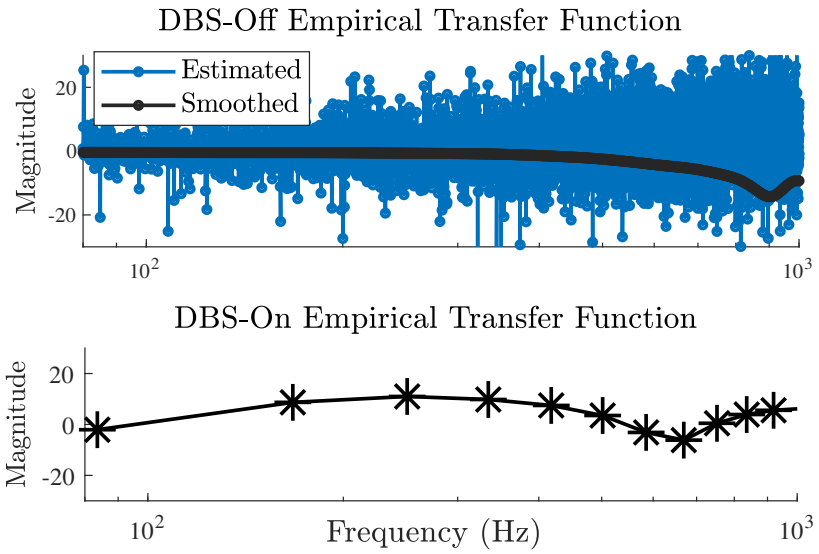

Figure 3.4: (Top) Bode magnitude plot of a raw and smoothed ETFE from the intrinsic neural signal recordings. (Bottom) Bode magnitude of a stimulation evoked potential transfer function. Note that the smoothing method has no effect on the stimulation evoked potential transfer function, as the response duration is brief (∼5 ms) with low number of samples (∼ 100); confirming that the smoothing method does not introduce distortions to the system.

Simulation and Comparison Method:

Let $u(t)$ be a pulse with similar specification to the true stimulation (90-μs pulse width and 3-V amplitude). Let $h(t)$ be the inverse Fourier transform (iFFT) or impulse response of the $H(\omega)$. Thus, the output of the system in time, $y(t)$, is given by the convolution of $h(t)$ with $u(t)$: $y(t) = h(t) * u(t)$. We estimated the output of the intrinsic neural signal transfer function ($y(t)$) by taking the average of the 50 responses to $u(t)$ computed for all 50 segments.

Now, let g_1 and g_2 be the iFFT of G_1 and G_2, and let y_1 and y_2 be their outputs, respectively. Thus, similarly, $y_1(t) = g_1(t) * u(t)$ and $y_2(t) = g_2(t) * u(t)$. Once the responses to $u(t)$ were estimated, we matched the sampling rates and synchronized all outputs with the respective EPs using cross-correlation. Then, we compared $y(t)$, G_1, and G_2 responses (y_1 and y_2) with their corresponding EP, in order to first, discover whether $y_1(t)$ or $y_2(t)$ better replicates the EP, and second, to determine if $y(t)$ can explain a significant fraction of variance in the EP.

Statistical Analysis:

First, we compared y_1 and y_2 with the actual EP to determine if the stimulation is transmitted through activation of nearby axons (G_1) or by activation of nearby cell bodies (G_2). Therefore, we computed the fraction of variance explained in EP by y_1 and y_2, and estimated which one is more likely. Then, we computed the fraction of variance explained in EP by the average response of all 50 DBS-off transfer functions computed from the 2-second segments ($y(t)$), R^2. This allowed us to verify whether the estimated transfer function from DBS-off intrinsic neural signal data ($H(\omega)$) estimates the direct EP. We used $\sim$50 repeated measures of R^2s for each pathway and each direction per subject to perform the statistical analysis. Among these 50 predictions, we marked the ones that were greater than 3 standard deviation from the mean as outliers (limiting to a maximum of 5 outliers for every 50 segments). Once

the outliers were removed, a linear mixed effect model with repeated measure was employed using lme4 [16] package in R-studio (R core team, 2021), with the distant targets as the fixed effect and random intercepts for all subjects. Thereafter, we performed a pairwise multiple comparison using Kenward-Roger's F-test with the emmeans [223] package to find the differences between each pathway (GPi-VoaVop, GPi-VA, and GPi-STN) by comparison of estimated marginal means, and to discover which pathway response is more likely to be predicted by a linear transfer function representation of that pathway. We adjusted the p-values using the Bonferroni method. The analyses were done with outliers included and outliers removed to confirm that the removal of outliers does not significantly affect the final results.

3.4 Results

3.4.1 Stimulation effect on distant targets: Activation of efferent axons or cell bodies?

For all subjects and all regions, the results showed that y_1 is highly correlated ($R^2 = 0.99$) with the actual recorded EP. This was expected since y_1 is the result of the convolving the actual EP with an impulse similar to the actual stimulation pulse. On the other hand the y_2 does not have a significan correlation with the actual EP as shown in Figure 3.5 by the red lines. This provides evidence that the stimulation itself is more likely to cause the EP at the distant target, perhaps by direct excitation of efferent axons near the stimulation site, as opposed to an indirect response due to local cell body excitation. This shows the similarity of y_1 and the actual EP and the inability of y_2 to replicate the EP. Therefore, for the remainder of this paper, EP and y_1 will be used interchangeably, depicted with blue lines in Figure 3.5.

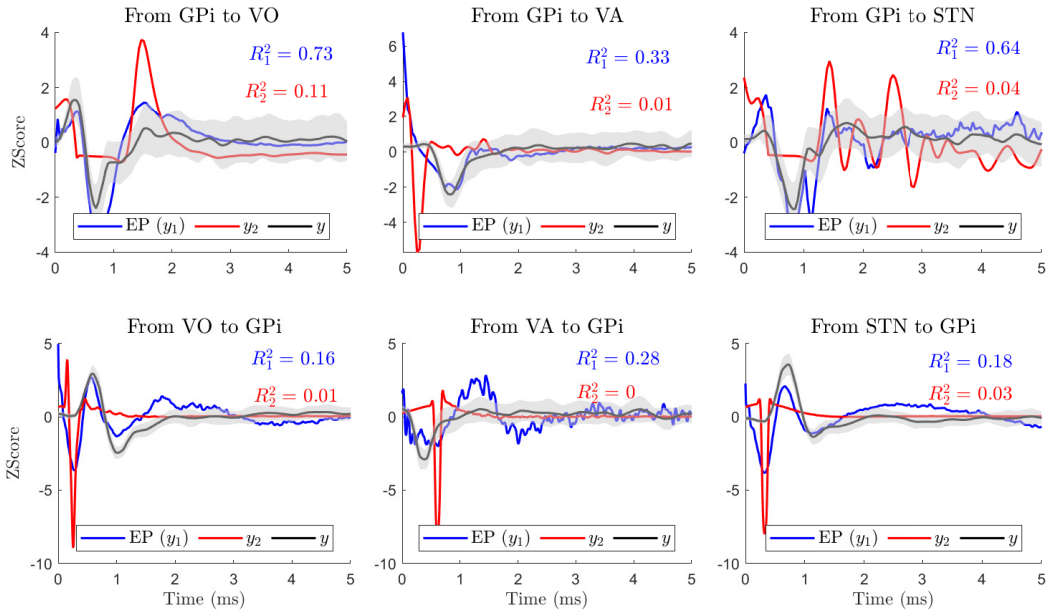

Figure 3.5: The plots show the true responses in VO, VA, and STN, evoked by stimulation in GPi ($y_1(t)$, blue lines). They also illustrate the estimated output of the transfer function G_2 ($y_2(t)$, red lines) as well as the response of the intrinsic neural signal transfer function H ($y(t)$, black lines, averaged over ∼50 segments) and its standard deviation with 95% confidence interval (gray shade). In all cases, the impulse response of the ETFE explains a high variance of direct EP or $y_1(t)$, and not the $y_2(t)$.

3.4.2 Do DBS Pulses propagate through pathways that transmit intrinsic neural signals?

In order to determine whether the DBS pulses are reaching the distant targets through pathways similar to the intrinsic neural signals or not, we tested the reliability and accuracy of the ETFE impulse responses and compared the predictions for all three pathways in both directions (forward and backward). In order to do so, we only compared our predictions with the EP ($y_1(t)$) for each pathway in each direction by computing the fraction of variance explained in EP by $y(t)$ (R_1^2).

The results from comparison of $y(t)$ with $y_1(t)$ (EP) and $y_2(t)$ for one subject are shown in Figure 3.5. As illustrated, the fraction of variance explained in $y(t)$ by $y_2(t)$ (R_2^2) is not

significant in any of the models. However, the fraction of variance explained in $y(t)$ (EP) by $y_1(t)$ (R_1^2) is significant in all the models. This result was consistent among all subjects and pathways (GPi-VoaVop, GPi-VA, and GPi-STN), supporting that the EP of the distant target is predicted by an impulse response of the ETFE at the stimulation site, consistent with depolarization of efferent neurons.

We used the linear mixed effect model ($R^2 = 0.25$) fitted to the R_1^2 (as repeated measures) to compare the quality of prediction in all three pathways, forward and backward. The results of multiple comparison between the pathways, shown in Figure 3.6, demonstrate that the predicted system outputs have stronger correlation with the DBS EPs in VoaVop and STN compared to the DBS EPs in VA ($p - value \prec .01$). The high fraction of variance of EP explained by the output of the transfer function $H(\omega)$ ($y(t)$) reveals that the pathways that transmit external electrical stimulation mostly include pathways that transmit intrinsic neural signals (GPi to VoaVop, GPi to VA, and GPi to STN). In other words, the pathways that transmit external electrical stimulation (DBS pulse) overlap with the pathways that transmit intrinsic neural signals.

3.4.3 Direction of Signal Transmission

Furthermore, we were able to predict the VA, VO, and STN responses to simulation in GPi significantly better than the GPi response to stimulation in VA, VoaVop, and STN ($p - value \prec .01$), respectively. This observation may be explained by underlying anatomical and physiological differences in the fibers connecting two targets (fiber size, anisotropy, and diffusivity or direction of intrinsic neural signal transmission; orthodromic versus antidromic). This also indicates that GPi-thalamus connection is more likely orthodromic, whereas thalamus-GPi is more likely antidromic, or carried by pathways that differ from the normal intrinsic transmission pathways.

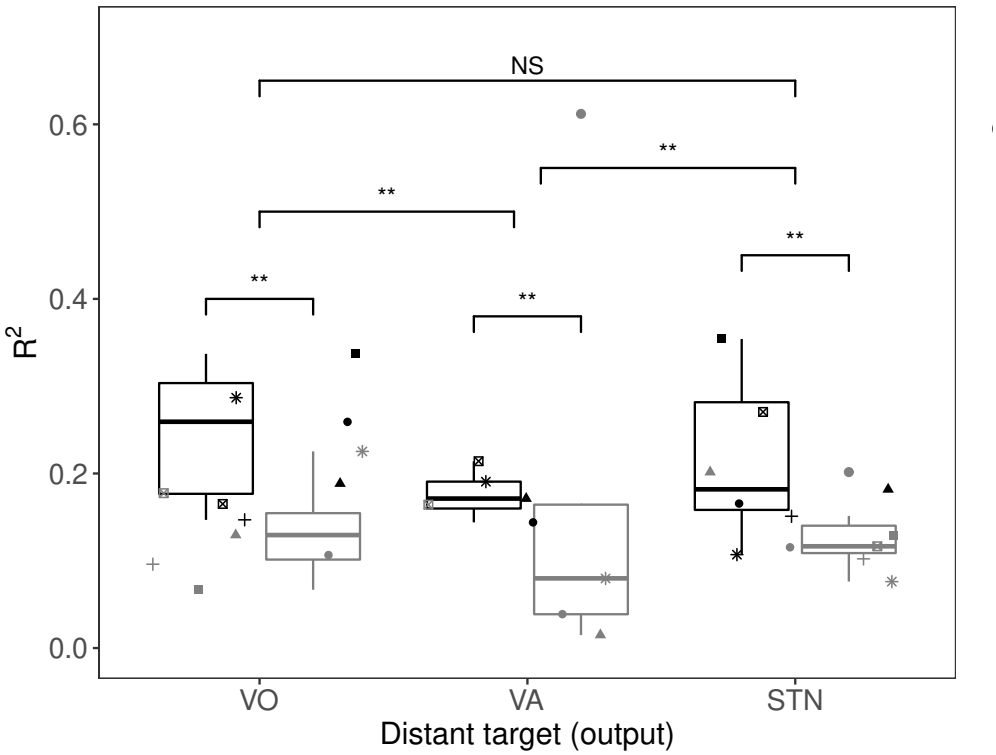

Figure 3.6: The fraction of variance (R^2) of DBS EP explained by the intrinsic neural signal transfer functions of each pathway (black: pathways from GPi; gray: pathways to GPi) for the seven subjects (each shape represents one subject). The variance explained is greater for STN and VoaVop ($p - value \prec .01$) compared to VA, suggesting that the DBS pulses from GPi to STN and VoaVop are more likely to use the same pathways as intrinsic neural signals, compared to the GPi-VA pathway between the electrode locations. However, the fraction of variance explained in EP by the intrinsic transfer functions of GPi-VoaVop and GPi-STN are not significantly different from each other. Moreover, the results also demonstrate that the ETFEs were able to make better predictions of EP in one direction (from GPi to other targets) compared to the reverse direction (from other nuclei to GPi) ($p - value \prec .01$).

3.5 Discussion

In this study we focused on understanding the DBS mechanism of action; as it is significantly important to elucidate the propagation pathways of DBS pulses and to confirm whether these pathways are the same as those utilized by intrinsic neural signals [252, 100]. Previous studies indicate a wide range of potential scenarios for DBS propagation, supported by various models and hypotheses. For example, Zhao et al. [252] demonstrated that STN-DBS in parkinsonian rats activates both motor and non-motor pathways and suggests that

this modulation is probably through orthodromic and antidromic pathways. In addition, through an fMRI study on the PD patients, Jet et al. [100] showed that the STN-DBS and VIM-DBS are transmitted to non-stimulated regions through the anatomical pathways, orthodromically and antidromically. However, systematic studies with computational models to explore these scenarios have been rarely conducted. The access to electrophysiological signals and advancements in engineering tools now enable detailed analyses to improve our understanding of the DBS mechanism of action, allowing for a more precise interpretation of how DBS activity propagates, facilitating the development of more optimized and effective approaches for DBS. Here, by using a transfer function analyses, we confirmed that DBS pulses travel at least in part along physiological motor pathways.

3.5.1 DBS affects distant targets through activation of afferent and efferent axons

In the first part of this study, we tested whether DBS pulses directly excite afferent or efferent cell axons near the stimulation site or they excite the efferent cell bodies, through evaluation of EPs due monosynaptic transmission. To achieve this, we compared the EP at a distant target with the empirical impulse response of two transfer functions obtained from DBS-on neurophysiological recordings; one indicating that the DBS affects the distant targets through the direct activation of efferent or afferent axons (y_1) and the other indicating that the DBS effect is through the activation of the nearby cell body, evoking a local response, and its subsequent transmission to distant targets (y_2). Our results indicate that y_1 is nearly identical to the actual EP, which was expected, while y_2 does not explain any variability in the actual EP at all. This result suggests that the DBS pulses are more likely to affect the distant targets through direct activation of the distant area as opposed to the transmission of the stimulation site's EP to the downstream areas, consequently evoking a response. Here, we are not rejecting other scenarios, but we are providing evidence that the effect of DBS

is significantly less probable through the transmission of local EP at the stimulation site to the distant target.

3.5.2 DBS pulse are more likely to travel along the normal anatomical pathways

Next, we compared the DBS EPs with the impulse responses obtained from intrinsic neural signals recorded during DBS-off condition, while patients were performing voluntary reaching movement ($y(t)$). If a significant portion of the EP or $y_1(t)$ can be explained by the $y(t)$ we can claim that the DBS pulse and the natural neural activity during movement are transferred to the output through the same mechanism. Our results showed that the fraction of variance predicted in STN, VoaVop, and VA EPs from stimulation in GPi was significantly different from zero, consistent with the hypothesis that DBS stimulation travels at least partly through normal physiological pathways. This provides evidence that the pathways that carry DBS pulses overlap with those that transmit intrinsic neural signals, indicating a similarity in their transmission mechanism.

3.5.3 Orthodromic versus Antidromic Signal Transmission

Previous studies on the mechanism of DBS in Parkinson's disease demonstrate the complex interaction of DBS and neural fibers in orthodromic and antidromic activation during the stimulation process [88, 162, 110, 81, 252, 245]. For example, Kang et al. [110] showed that STN-DBS induced both orthodromic and antidromic activation through afferent and efferent axonal activation [39] and explored relative contribution of antidromic versus orthodromic effects of STN-DBS in Parkinson's disease [110].

Here, after we confirmed that the DBS pulses and neural signals pathways overlap, we must

validate our method. One way to do it is to perform the same analysis in the direction of antidromic pathways. In this case, we expected to see significantly lower correlation between the DBS-off impulse responses ($y(t)$) with the antidromic DBS EPs, since, naturally, intrinsic neural signals do not travel antidromically.

To achieve this goal, we first stimulated in GPi and recorded in thalamus and STN, which makes it reasonable to expect that external evoked responses were primarily carried by orthodromic pathways (specially in VoaVop and VA nuclei of thalamus). Second, we included GPi responses to the thalamic nuclei and STN stimulation in our analyses to compare the ETFE response accuracy in one direction versus the opposite direction. Our results showed that the ETFEs could possibly be a good estimate of direction of pathways in GPi to thalamic subnuclei (VoaVop and VA) projections; orthodromic versus antidromic. The higher correlations of ETFE responses with the thalamic DBS EPs in orthodromic (GPi to VA or VoaVop) versus antidromic (VoaVop or VA to GPi) pathways supports our hypothesis and is a confirmation for use of this method. This suggests that physiological pathways from VA, VoaVop, and STN to GPi are less robust than in the opposite direction, and that a greater fraction of the DBS signal may travel through non-physiological pathways in this direction. However, the higher correlation of GPi-STN impulse responses with the EP versus that of STN-GPi does not reflect the bidirectional connectivity between GPi and STN.

We showed that the GPi-VoaVop and GPi-STN responses have higher correlation with their respective impulse response predictions. The higher correlation of the ETFE responses in GPi-VoaVop, and GPi-STN, (in both directions) with the EPs compared to GPi-VA could be due to the fact that there are fewer projections or fibers connecting GPi to VA, leading to less flow of intrinsic neural signals.

3.6 Limitations

An important weakness of this method is that while the estimated transfer function has an implicit direction, it does not provide evidence of causality, since it is essentially a correlation method [78]. Therefore, the presence of a transfer function from GPi to thalamus does not indicate that activity in GPi is responsible for activity in thalamus. On the other hand, the stimulation results (EPs) do indicate causality, but may only partially correspond to normal physiological transmission pathways. Several other scenarios, including reverse transmission or common drive to both sites, remain possible.

Second potential limitation of this study is that subjects were performing voluntary movement during the recording of intrinsic brain activity, whereas they were at rest during the recording of electrical evoked responses. This element of study design was intentional, in order to evaluate whether signals associated with voluntary (but potentially abnormal) movement flow along the same pathways as DBS responses and whether connectivity in the resting state determines signal flow in the active state. Since we assume that a higher flow of movement-related information in the motor pathways could lead to stronger correlation between two ends of a motor pathway and therefore the obtained transfer function from the intrinsic neural signal is a better representation of that pathway. Moreover, by using this method, we ensure that the correlation between the DBS-off impulse responses and the evoked potential are not related to voluntary movements.

Finally, it is crucial to acknowledge the limitations associated with LTI models [129, 251]. LTI models, chosen for their simplicity and interpretability, may not fully capture the dynamic and nonlinear nature of brain function and neural transmission. The brain's complex and adaptive nature might involve time-varying dynamics that cannot be adequately addressed by LTI models [128, 28]. However, LTI models are powerful tools for explaining the linear behavior of the systems. For example, here, despite the nonlinear nature of the neural

activity within the brain, we were able to explain potentially a nonlinear phenomena using a linear method.

3.7 Conclusion and Future Direction

In conclusion, our novel transfer function approach has the potential to describe DBS signal propagation mechanism and possibly, pave the way toward prediction of DBS signal transmission and the causal direction of intrinsic neural signals. Our results imply that electrical stimulation in GPi travels at least in part along pathways that are part of the usual communication between GPi-VoaVop and GPi-STN, and to a lesser extent between GPi-VA. These findings build on what is already established regarding GPi projections to the thalamus nuclei, VoaVop and VA within the motor pathway circuit. This suggests that the natural oscillations dynamics (DBS-off neurophysiological signals) contain useful information about the network responses to DBS pulses, which can be further explored. The results presented here are a first step toward understanding how patterns of therapeutic stimulation interact with the "connectome" to achieve therapeutic benefit. Future work will focus on determining if there are notable differences between anatomical and non-anatomical pathways and studying the impact of DBS on distant brain network underlying activity.

Chapter 4

DBS modulates transmission of dystonic signals in pallidothalamic networks and the local and global oscillations in deep brain regions

4.1 Abstract

Deep brain stimulation (DBS) is a neuromodulation technique commonly used for treatment of movement disorders, including dystonia. Stimulation of the internal globus pallidus (GPi) of basal ganglia or the subthalamic nucleus (STN) typically confers clinical benefit, although the specific mechanism of action is unknown. Previous studies of dystonic patients show abnormalities in low frequency activity in GPi and other motor sensory regions such as STN, Ventral Oralis Anterior/Posterior (VoaVop), and Ventral Anterior (VA) nuclei of thalamus. We hypothesize that the DBS works in part by altering transmission of abnormal signals in

low frequency bands between different brain regions, both at the stimulation site (e.g. GPi) and distant deep brain regions.

In other words, GPi stimulation reduces the transmission of abnormal signals along the projections to thalamic motor subnuclei and modulates low frequency activity on those regions, resulting in improvement of motor symptoms. To test this hypothesis, we used a novel transfer function analysis that has not previously been utilized to study neural signal transmission. We recorded intracranial signals from thirteen pediatric and young adult patients with dystonia, with and without stimulation. We then performed a transfer function analysis, which allowed us to make comparisons between the mean transfer function gains (a measure for amplification of signals from an input to the output of a system) in low frequencies for each deep brain network pathway for the DBS-on and DBS-off conditions. Our results show that DBS modulates the transmission of information between different brain regions. Specifically, we confirmed that GPi stimulation effectively modulates the transfer function gains from pallidum to motor subnuclei of thalamus by increasing the transmission of signals in beta and gamma frequency bands. These results elicit a better understanding of the mechanism and effects of DBS. This, in turn, may provide fundamental knowledge for the development of closed-loop DBS, particularly in controlling the intensity and pattern of stimulation. A better understanding of neuromodulation could also help to further the design of brain-computer interfaces and neurorehabilitation systems.

4.2 Introduction

Deep brain stimulation (DBS) is commonly thought to act by modulating or blocking activity within specific brain regions. Here, we explore the possibility that DBS may also act by modulating the transmission of signals between different brain regions. In particular, we examine whether DBS reduces the transmission of abnormal low frequency oscillations between basal

ganglia and thalamus in children with primary and secondary dystonia [214, 207, 212, 206]. "Dystonia is defined as a movement disorder in which involuntary sustained or intermittent muscle contractions cause twisting and repetitive movements, abnormal postures, or both" [5, 209]. The underlying mechanism of dystonia is not known [5, 207]. However, previous studies have shown that the motor symptoms of dystonia could have several origins including: decreased focus on intended patterns of muscle activity [112], imbalances between midbrain and striatal excitatory/inhibitory signaling [17], abnormal patterns of subcortical activity [114, 92], excessive basal ganglia or peripheral loop gain [114, 113, 200]. Furthermore, mathematical models of dystonia propose that motor features of dystonia may arise from an imbalance in neural circuitry, specifically, an increased gain in the indirect pathway relative to the direct pathway which could lead to unstable and uncontrolled synchronous oscillations within the cortex and basal ganglia [200]. Such oscillatory behavior is assumed to contribute to dystonia, as effective motor control necessitates a controlled balance between these two pathways as depicted in Fig. 4.1 (a). Moreover, microelectrode recordings from our previous works suggest that these abnormal patterns are associated with increased activity in the internal globus pallidus (GPi) of basal ganglia [200] during voluntary movement, particularly at low frequencies in theta (4-8 Hz) and alpha (8-13 Hz) frequency bands [114, 92], providing support for these mathematical models. GPi is essentially an inhibitory nuclei. Therefore, the propagation of excessive activation from basal ganglia to thalamo-cortical loops leads to failure of appropriate inhibition of the thalamo-cortical network. This results in both insufficient inhibition of undesired movement and insufficient disinhibition of intended movement [114]. DBS of the GPi and subthalamic nucleus (STN) at clinically effective frequencies, 120-190 Hz for GPi [73] and 130-185 Hz in STN [30], shows marked clinical benefit, though the exact mechanism of effect is unknown [207, 212, 206]. Moreover, we have shown in a separate study that DBS stimulation pulses are more likely to be transferred through the same pathways as the intrinsic signals [113] by predicting the high frequency evoked responses from DBS using a transfer function model. However, the low frequency con-

tents of these transfer functions, which represents the underlying neural transmission, were not studied. Therefore, how these pulses influence the intrinsic signals is still unclear. Three possible explanations are facilitating, blocking, or changing the power and transmission delay in several frequency bands, or some combination of these effects. [113]. Understanding how DBS signals flow through deep brain networks and influence motor circuitry, especially pathways from pallidum to thalamic motor nuclei, would enhance our understanding of the pathophysiology of dystonia and the mechanism of DBS in treatment of dystonia.

Transfer Functions are commonly used in engineering to analyze transmission of band-limited information between a source and destination. Here, we apply this type of analysis to examine the magnitude of transmission in multiple frequency bands between different brain regions, and how this transmission changes in the presence of DBS. We hypothesized that GPi and STN stimulation alter the transmission of abnormal low frequency activity within the indirect pathway, specifically transmission from STN to GPi. We also explored if GPi and STN stimulation impact the transmission of low frequency activity via outputs of the direct and indirect pathway, from GPi to thalamic nuclei. Our analysis considers the standard low frequency bands: delta, theta, alpha, beta, and low gamma. We further explored the effect of stimulation frequency on the pattern of signal transmission exhibited by three known anatomical pathways in pallidothalamic network: STN to GPi and GPi to VoaVop, and GPi to VA.

To study the effects of stimulation on deep brain network signal transmission, signals were acquired using externalized stereoelectroencephalography (sEEG) leads implanted in basal ganglia and thalamic nuclei in thirteen children and young adults with childhood-onset dystonia of various underlying etiologies (genetic, acquired, or metabolic). Recordings of both the DBS-on and DBS-off conditions were acquired. Empirical transfer functions and their magnitude responses, up to 50 Hz, were then estimated for pathways connecting each pair of these motor regions, in both DBS-on and DBS-off conditions. When multiple electrode

brain recordings are available, transfer function analysis may be an important technique for analysis of the transmission of information between different regions. This method allows for estimation of the flow of information in low frequencies (underlying intrinsic neural activity) during stimulation regardless of the stimulation artifacts, as DBS targets are only stimulated at frequencies above 50 Hz. To our knowledge, this method has not been utilized in the field of brain stimulation and neuromodulation before. This provides an analytical framework that can be used to better understand the effects of DBS on the information flow in deep brain circuitry. Additionally, it sheds light on the mechanism of deep brain stimulation, which could lead to improvement of DBS programming protocols and closed-loop DBS designs.

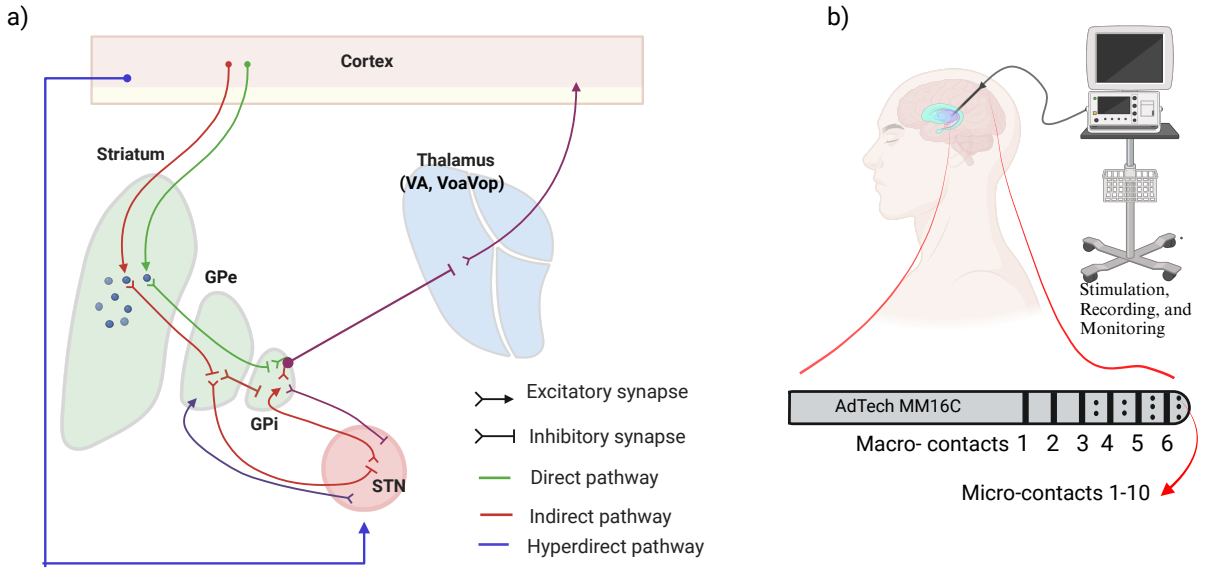

Figure 4.1: a) Schematic representation of the direct and indirect pathways in the cortico-basal ganglia-thalamo-cortical loop. This diagram illustrates the neural pathways within the basal ganglia, thalamus, and cortex, emphasizing their roles in the facilitation and inhibition of movement. The direct pathway (shown in green) promotes the activation of motor cortex through a series of disinhibitory signals. Conversely, the indirect pathway (depicted in red) inhibits movement by suppressing motor cortex activity via inhibitory signalling through thalamic nuclei. The co-activation of these two pathways could be essential for movement initiation and accurate motor control. b) Schematic of an externalized sEEG lead in a deep brain region. This figure illustrates the positioning of the lead within a specific deep brain area, connected to a monitoring unit capable of stimulating and recording simultaneously [21].

4.3 Materials and Methods

4.3.1 Subjects

The stimulation data and baseline recordings from thirteen pediatric and young adult patients undergoing deep brain stimulation (DBS) surgery for the treatment of dystonia were selected for this study (S1-S3, S12-S14, S16, S17, S19-S23 in Table 1).

Data treatment and filtering

All the data, including the baseline LFPs and the stimulation LFPs, were notch filtered at 60 Hz and its two harmonics. A 4^{th} order butterworth highpass filter was applied with a cutoff frequency of 1 Hz to remove drift. The monopolar recordings from the micro-contacts on each row of the lead (total of 10 per lead) were re-referenced to a bipolar montage by computing the voltage difference for each pair of adjacent micro-contacts. Re-referencing produced 8 channel recordings per lead, as shown in Figure. 4.2 (b). This process removes the common mode noise and uncovers the underlying neural activity [114]. It is important to note that a post-processing step to remove stimulation artifacts is not necessary in this case, because all stimulation artifacts will occur at multiples of the stimulation frequency and therefore are effectively removed by low pass filtering below 50Hz. For consistency throughout our analyses, we used a maximum of 10 seconds of signals per stimulation setting and/or baseline recording.

4.3.2 Computation of transfer function

An empirical transfer function can be computed using several different methods. The magnitude of the transfer function is a linear measure of the amount of information transferred

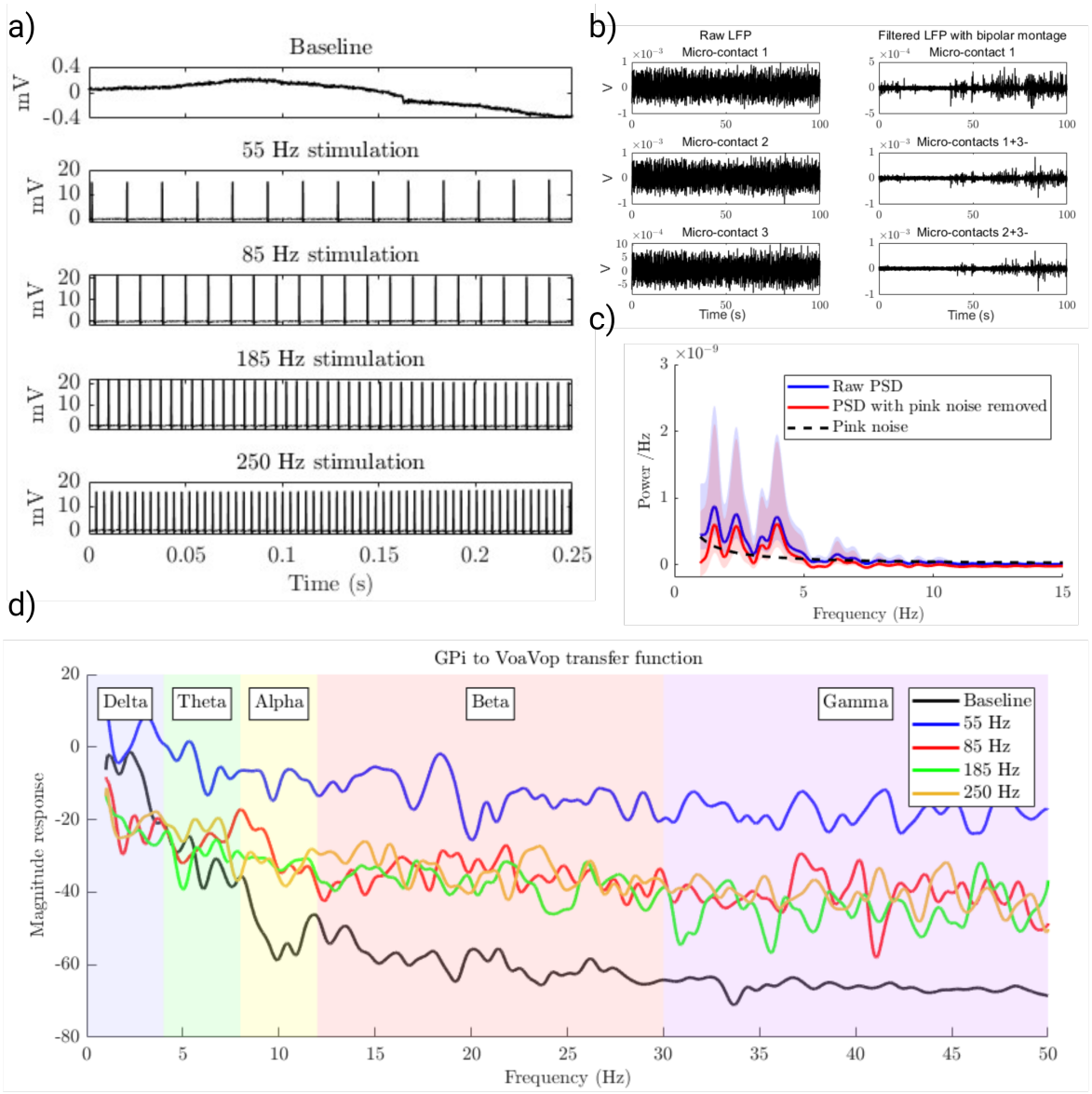

Figure 4.2: a) Sample of raw data recorded over 0.25 seconds during baseline, and during DBS at 55, 85, 185, and 250 Hz,demonstrating contamination from artifacts during the stimulation; b) Baseline LFP recordings from three micro contacts on the first row of STN lead (left). We high pass filtered the signals and transformed them into the bipolar montage (computed the voltage difference) for each adjacent pair on one row (right); c) Raw Power Spectral Density (PSD; blue), the fitted pink noise (black dashed line), and the PSD after removal of the pink noise component (red); d) This figure depicts samples of GPi to VoaVop transfer function magnitudes during baseline and during GPi-DBS at 55, 85, 185, 250 Hz stimulation frequencies, highlighting a significant increase in magnitude response across all bands (delta, theta, alpha, beta, and gamma) during the stimulation.

between two points at each individual frequency. In this study, in particular, we wanted to evaluate the changes in the magnitude response of transfer function representation of each pathway connecting two points between two electrodes. The transfer function between each two points is computed as the ratio of the output Fourier transform to the input Fourier transform [22, 113, 78]. The power spectral density (PSD) can be estimated as the value of the Fourier transform to the power of two, divided by 2 times the frequency spacing. Therefore we can estimate the transfer function magnitude by:

$$|H| = \frac{|FT(Y)|}{|FT(X)|} \approx \frac{PSD(Y)^{\frac{1}{2}}}{PSD(X)^{\frac{1}{2}}} = \frac{PSD(Y)^{\frac{1}{2}} PSD(X)^{\frac{1}{2}}}{PSD(X)} = \frac{|CPSD(X,Y)|}{PSD(X)} \tag{4.1}$$

Where $PSD(X)$ is the power spectral density of the input and $CPSD(X,Y)$ is the cross power spectral density between input and output. This single-input-single-output (SISO) transfer function model is a linear representation of each pathway, all of which can be combined to comprise a multiple-input-multiple-output (MIMO) system. However, here, we analyze each pathway individually, therefore H represents the pathway transfer function ($H(\omega)$) itself [108]. This model can characterize how each region affects the signal transmission within the whole network and how that network responds to exogenous stimulation (DBS) [108].

It is worthy to note that transfer functions that relate two signals are essentially different from their coherence. The coherence in a linear time-invariant (LTI) system is one and in that case the transfer function is a good estimator of relationship between two signals. Here, we assume that two signals have a unit coherence and we compensate for it by adding a regularization parameter that accounts for all the inputs to the system beside the actual input node. In addition, in the process of deriving transfer functions from PSDs, the incorporation of a regularization constant, ϵ, in the denominator is a critical step to ensure numerical

stability and accuracy. This need arises particularly at frequencies where the PSD of the input approaches zero, leading to potential numerical instability due to division by values close to zero. To mitigate this, a small value (ϵ) is added to the denominator, effectively ensuring that the transfer function remains well-defined across all frequencies. The value of ϵ was determined to be $5e-11$ through a trial-and-error approach, aiming to find the smallest constant that prevents numerical issues while minimally impacting the fidelity of the transfer function. The rationale behind adding a constant to the denominator is due to the assumption that any other inputs contributing to the output of the system follow a constant distribution, implying that the system's response at frequencies where the input PSD is very low is dominated by these other inputs. Consequently, the introduction of ϵ can be viewed as a representation of the baseline level of these other contributions, providing a more realistic and stable characterization of the system's behavior. This approach, while empirical, aligns with common practices in system identification and signal processing, where balancing the fidelity of the model with the practical limitations of real-world data is often necessary. Thus, the new transfer function equation is:

$$H = \frac{CPSD(X,Y)}{PSD(X)+\epsilon}, \tag{4.2}$$

where ϵ is the regularization constant.

For each subject, the PSD for each channel and the pairwise cross spectral density (CPSD) between the channels were computed in the DBS-on (separately for different frequencies) and DBS-off conditions using Welch's method with a $\sim 3\ s$ hamming window, 30% overlap, and over a frequency range of 1 to 50 Hz. The computed PSDs and CPSDs are contaminated with pink noise which is characterized by a fractional ($\frac{1}{F}$) decay. Therefore, we fitted a function, $\frac{a}{b+F}$, to all computed spectra and then subtracted that fractional trend from the data, as

illustrated in Figure 4.2 (c). Once pink noise was removed, the transfer function model of each pathway was constructed using Equation 4.2, for baseline and also all stimulating pairs.

The aim of this study is to assess the effect of different frequencies of stimulation on the transmission of low frequency oscillations (LFO) within deep brain networks. Due to the wide usage of low frequency bands in neurology, we analyze these effects in EEG standard frequency bands (delta [0.5-4 Hz], theta [4-8 Hz], alpha [8-13 Hz], beta [13-30 Hz], and low gamma [30-50 Hz]), as depicted in Figure. 4.2 (d). Therefore, the mean transfer function gain was computed at each of these frequency bands and the effect of stimulation at different frequencies was compared within each frequency band. Note that the frequencies analyzed for the transfer function analysis (0.5-50 Hz) are considerably lower than the stimulation frequencies (55-250 Hz), so the changes we analyze are likely to represent neural effects of stimulation rather than a direct electrical stimulation or blocking effect.

4.4 Results

We fitted linear mixed-effects models to the mean transfer function gain at each frequency band to estimate the effects of stimulation, including the impact of various stimulation frequencies, on these gains. After careful analysis and visualization of the data, we realized that the effect of stimulation frequency on these gains is not linear. Therefore, we treated the stimulation frequency as a discrete variable and we performed pairwise comparisons to assess the significance of the observed changes relative to the baseline transfer function gains, across all standard EEG frequency bands, and compared how they differ from each other. All reported p-values are Bonferroni-corrected for increased reliability of the results. The fitted nested linear mixed effect model in R to assess the effect of DBS frequency on different pathways' signal transmission was defined as:

$$\text{TF Gains} \sim \text{Frequency} * \text{Pathway} + (1|\text{Subject} : \text{Frequency}) + (1|\text{Subject} : \text{Pathway}) \quad (4.3)$$

where subjects are the random effects, which would account for individual variations. The stimulation frequency and the pathways served as both fixed effect and random effect nested within each subject in the models, contributing to the overall variance in the data and the within-subject intercept variability. We then performed a pairwise comparison between the changes of transfer function gains for all standard frequency bands during STN stimulation ($N = 12,\ R^2_{theta} = 0.44,\ R^2_{alpha} = 0.48,\ R^2_{beta} = 0.49,\ R^2_{gamma} = 0.49$) and during GPi Stimulation ($N = 13,\ R^2_{theta} = 0.48,\ R^2_{alpha} = 0.49,\ R^2_{beta} = 0.52,\ R^2_{gamma} = 0.52$). We excluded delta band due to contamination at the low frequency filter cutoff. Also one subject is excluded from STN Stimulation analysis as they did not have STN lead implanted. The significance of the estimated coefficients were tested by type III Analysis of Variance Table with Satterthwaite's method and the p-values were computed from the test statistic based on chi-squared distribution with threshold of 0.05. The results from the model show that stimulation in both STN and GPi increased transfer function gains significantly in all routes for all patients, regardless of the frequency bands as depicted in Figure 4.3.

We then performed a pairwise multiple comparison using Kenward-Roger's F-test with the emmeans [223] package to find the differences between each pathway (GPi-VoaVop, GPi-VA, and STN-GPi) and their interaction (conditional effect) with stimulation frequencies (0, 55, 85, 185, and 250 Hz). This method compares the estimated marginal means to discover the effect of stimulation frequency on the patterns of transmission.

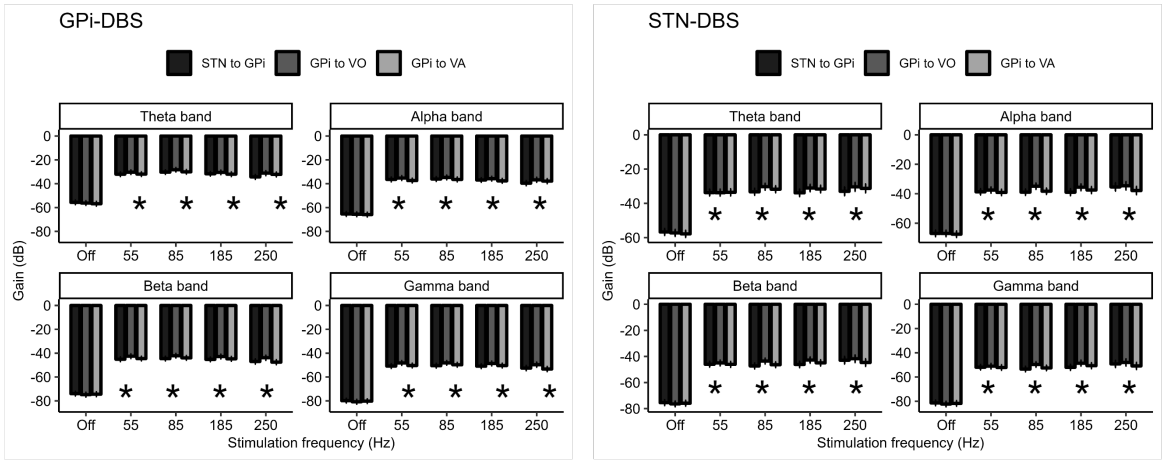

Figure 4.3: Transfer function gains of theta, alpha, beta, and gamma bands at the baseline activity and during 55, 85, 185, 250 Hz GPi-DBS and STN-DBS. All the transfer function gains during DBS are significantly larger than the gains during the baseline (DBS-off), illustraded with *.

4.4.1 GPi stimulation

Theta and Alpha bands: The results of pairwise comparison showed no significant changes within pathways at frequencies of stimulation.

Beta band: The results of pairwise comparison with respect to baseline showed that during all stimulation frequencies 55, 85, 185, and 250 Hz GPi-DBS, GPi-VoaVop beta band gains are significantly higher than that of STN-GPi (Estimates $_{\text{Beta}} = 2.59, 2.42, 2.38, 3.14$ respectively: $p - value < 0.01$) [1] and GPi-VA (Estimates $_{\text{Beta}} = 1.99, 1.82, 1.92, 3.70$: $p - value < 0.01$), while this gains are not significantly different at baseline activity.

Gamma band: Similar to the results at Beta band, the results of pairwise comparison with respect to baseline showed that during all stimulation frequencies 55, 85, 185, and 250 Hz GPi-DBS, GPi-VoaVop gamma band gains are significantly higher than that of STN-GPi (Estimates $_{\text{Gamma}} = 2.58, = 2.37, 2.25, 2.88$ respectively: $p - value < 0.01$) and GPi-VA (Estimates $_{\text{Gamma}} = 2.11, 1.59, 1.72, 3.70$: $p - value < 0.01$), while this gains are not

[1] "Estimates" are the estimates of the effect sizes.

significantly different at baseline activity.

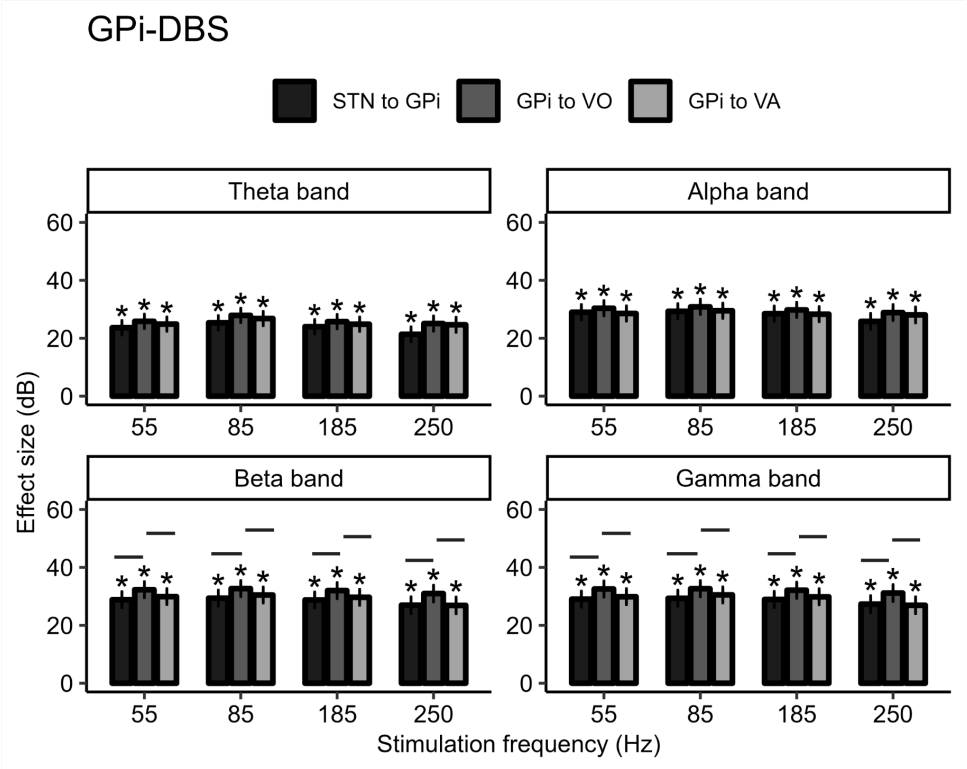

Figure 4.4: Statistical results: Effect of GPi-DBS on the transfer function gains within the pathways, with respect to the baseline transfer function gains. The lines indicate the significance within pathways and the *s indicate the significance of each bar with respect to baseline gains (DBS-off).

In summary, as shown in Figure 4.4, the the transfer function gains did not differ within the stimulation frequencies, specially the clinical effective stimulation frequency, 185 Hz. However, the results show that during all stimulation frequencies, GPi-VoaVop gains increased significantly compared to the GPi-STN and GPi-VA gains at beta and gamma bands, but not the theta and alpha bands. Moreover, the statistical analysis on the effect of GPi-DBS on the transfer function gains at each frequency band is shown in Figure 4.5. These results illustrate that the GPi-DBS has the lowest effect size (least increase) on the theta band transmission and the highest at beta and gamma band transmission. Meaning that the DBS facilitates transmission of beta and gamma more than the transmission of theta activity in

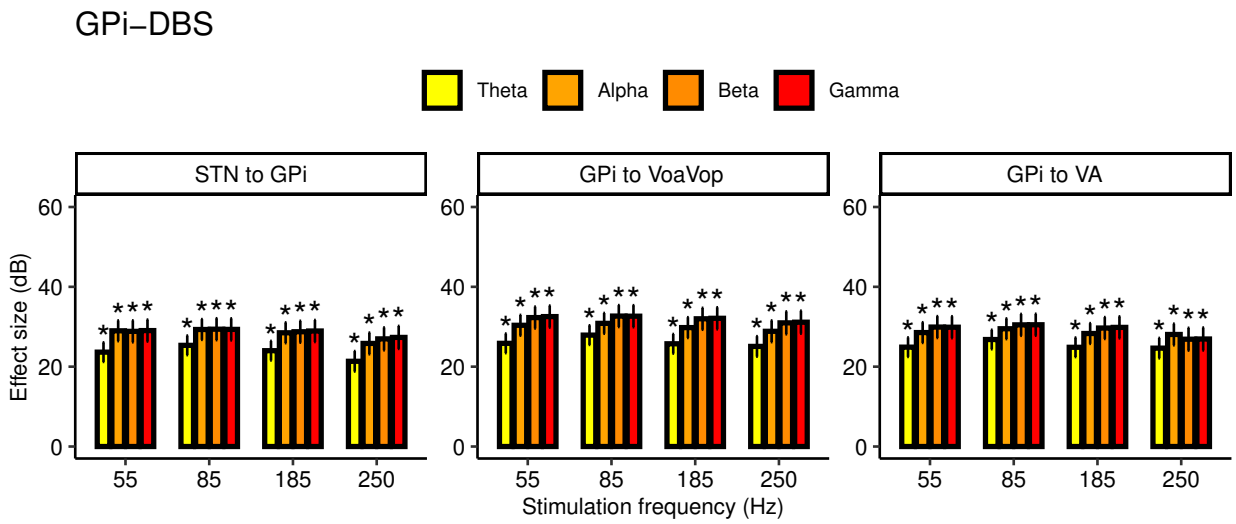

Figure 4.5: Statistical results: Effect of GPi-DBS on the transfer function gains within the frequency bands for each pathway.

pallido-thalamic network.

Clinically optimal versus non-optimal GPi-DBS setting:

We marked the optimal stimulation settings (stimulation macro-contacts, leads, and stimulation frequencies) for those patients that responded to GPi-DBS and performed the same statistical analysis. All thirteen patients responded to GPi DBS either at 185 or 55 Hz. We fitted a linear mixed effect model as:

$$\text{TF Gains} \sim \text{Setting} * \text{Pathway} + (1|\text{Subject} : \text{Pathway}) \tag{4.4}$$

where "setting" stands for the DBS setting regardless of the stimulation frequency and has three levels: 1. DBS-off, 2. non-optimal setting, 3. optimal setting. After we fitted the models for each frequency band gain ($N = 13$, $R^2_{theta} = 0.57$, $R^2_{alpha} = 0.62$, $R^2_{beta} = 0.64$, $R^2_{gamma} = 0.65$), we performed a pairwise comparison to determine whether the "optimal" and "non-optimal" settings had different effects on the transmission of signals within deep

brain regions. Figure 4.6 shows all the transfer function gains in for frequency bands (theta, alpha, beta, gamma) for all pathways. Each color represents one patient with their mean gain and standard deviation.

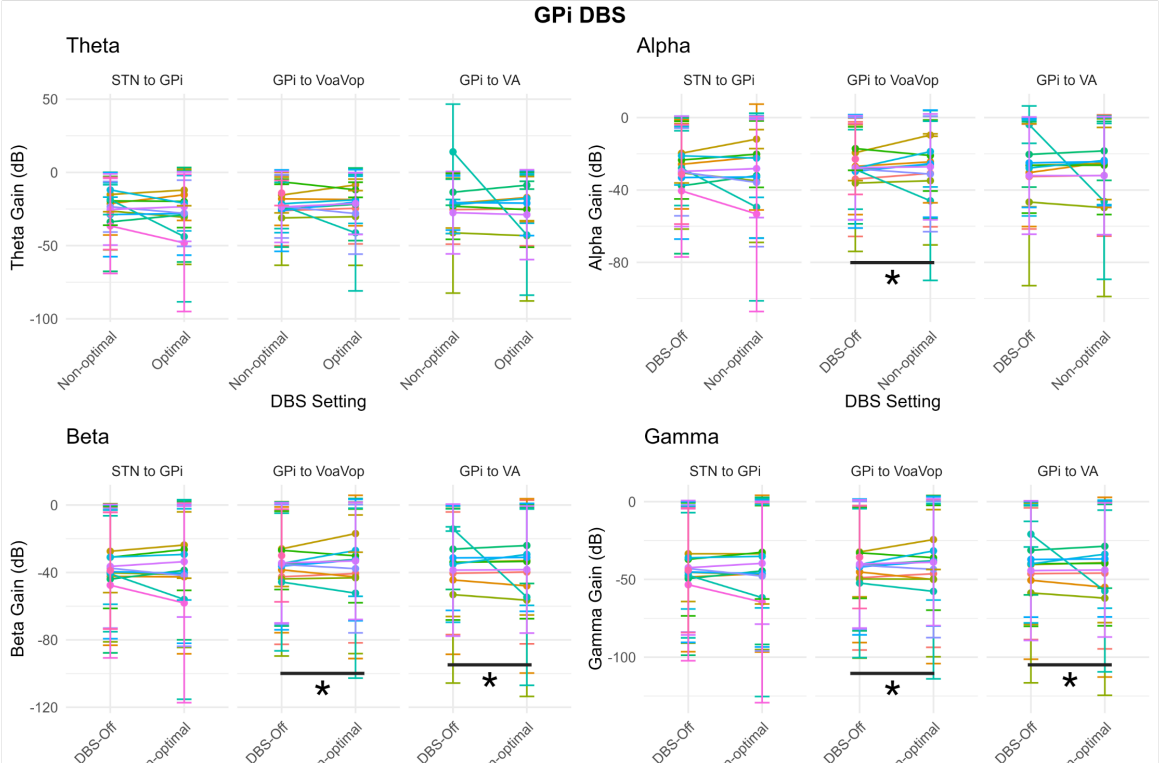

Figure 4.6: Effect of optimal versus non-optimal GPi-DBS setting of transfer function gains, shown for each pathway and frequency band, for all patients. Here, GPi DBS was effective clinically for all patients.

The results showed that there is no difference between the effect of optimal versus non-optimal DBS on the STN to GPi transfer transfer function gains, as shown in Figure 4.6. However, anova test revealed that the GPi-VO gain during the optimal DBS is significantly larger than that of non-optimal DBS, in alpha ($Estimte = 2.37; p - value < 0.01$), beta ($Estimte = 2.69; p - value < 0.01$), and gamma ($Estimte = 2.95; p - value < 0.01$) bands. Similar effect was seen in the GPi to VA transfer function gains in only beta ($Estimte = 1.28; p - value < 0.05$) and gamma ($Estimte = 1.32; p - value < 0.05$) bands. For simplicity of the figure we are not showing the significance between the DBS-off versus optimal and non-optimal stimulation setting.

4.4.2 STN stimulation

Theta band: The results of pairwise comparison showed no significant changes within pathways at frequencies of stimulation (Figure 4.7).

Alpha band: The results of pairwise comparison with respect to baseline showed that during 85 Hz STN stimulation, GPi-VoaVop alpha band gain is significantly higher than that of STN-GPi (Estimate = 4.01: $p - value < 0.01$) and GPi-VA (Estimate = 3,36: $p - value < 0.01$). In addition, during 185 Hz STN stimulation, GPi-VoaVop alpha band gain is significantly higher than that of STN-GPi (Estimate = 3.37: $p - value < 0.01$) but not GPi-VA, which could mean that it does not interfere with GPi-VA transmission. STN-DBS at 250 Hz imposed an increased GPi-VoaVop versus GPi-VA transmission (Figure 4.7).

Beta band: The results of pairwise comparison with respect to baseline showed that, similar to alpha band, during 85 Hz STN stimulation, GPi-VoaVop alpha band gain is significantly higher than that of STN-GPi (Estimate = 3.75: $p - value < 0.01$) and GPi-VA (Estimate = 2.79: $p - value < 0.01$). In addition, during 185 Hz STN stimulation, GPi-VoaVop alpha band gain is significantly higher than that of STN-GPi (Estimate = 3.40: $p - value < 0.01$) but not GPi-VA. However there was no significant change were observed within pathways due to 250 Hz STN-DBS (Figure 4.7).

Gamma band: The results of pairwise comparison with respect to baseline showed that, similar to alpha and beta band, during 85 Hz STN stimulation, GPi-VoaVop alpha band gain is significantly higher than that of STN-GPi (Estimate = 3.83: $p - value < 0.01$) and GPi-VA (Estimate = 2.85: $p - value < 0.01$). In addition, during 185 Hz STN stimulation, GPi-VoaVop alpha band gain is significantly higher than that of STN-GPi (Estimate = 3.41: $p - value < 0.01$) but not GPi-VA (Figure 4.7).

In summary, as shown in Figure 4.7, the GPi-VoaVop gains at the commonly used clinical

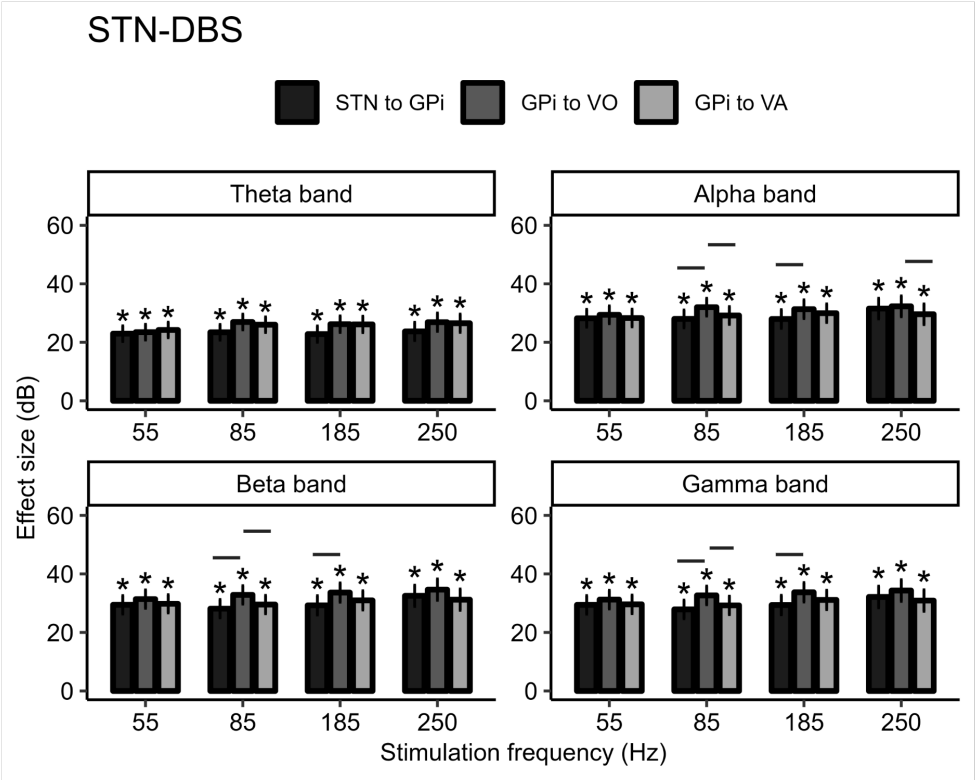

Figure 4.7: Statistical results: Effect of STN-DBS on the transfer function gains within the pathways.

stimulation frequencies for STN-DBS (85 and 185 Hz) are significantly larger than those of STN-GPi in alpha, beta, and gamma bands, but not the theta band. Moreover, the statistical analysis on the effect of STN-DBS on the transfer function gains at each frequency band is shown in Figure 4.8. These results illustrate that the STN-DBS has the lowest effect size (least increase) on the theta band transmission and the highest at beta and gamma band transmission. Meaning that the DBS facilitates transmission of beta and gamma more than the transmission of theta activity in pallido-thalamic network.

Clinically optimal versus non-optimal STN-DBS setting:

Similarly, we marked the optimal stimulation setting for those patients that responded to STN-DBS, and this time, instead of using stimulation frequency as a predictor we tested

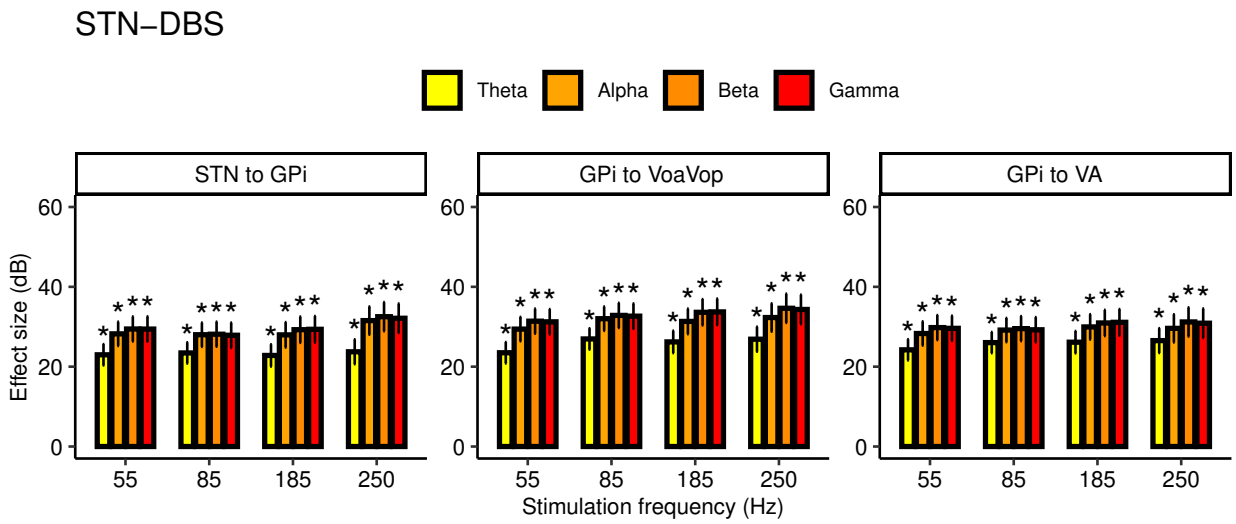

Figure 4.8: Statistical results: Effect of STN-DBS on the transfer function gains within the frequency bands for each pathway.

whether the "optimal" and "non-optimal" stimulation settings are different from each other and baseline. We only had 3 patients who responded to STN DBS. We used the same linear mixed effects model equation (Eq. 4.4) to fit the models. After the models were fit for each frequency band gain ($N = 3$, $R^2_{theta} = 0.15$, $R^2_{alpha} = 0.17$, $R^2_{beta} = 0.18$, $R^2_{gamma} = 0.17$), we performed a pairwise comparison to determine whether the "optimal" and "non-optimal" settings had different effects on the transmission of signals within deep brain regions. Figure 4.9 shows all the transfer function gains in four frequency bands (theta, alpha, beta, gamma), for all pathways. Each color represents one patient with their mean gain and standard deviation. No significant effect associated with the best clinical setting was observed due to STN-DBS; however, We cannot draw a definitive conclusion from these observations due to the small effect size and limited number of patients responsive to STN-DBS. For simplicity of the figure we are not showing the significance between the DBS-off versus optimal and non-optimal stimulation setting.

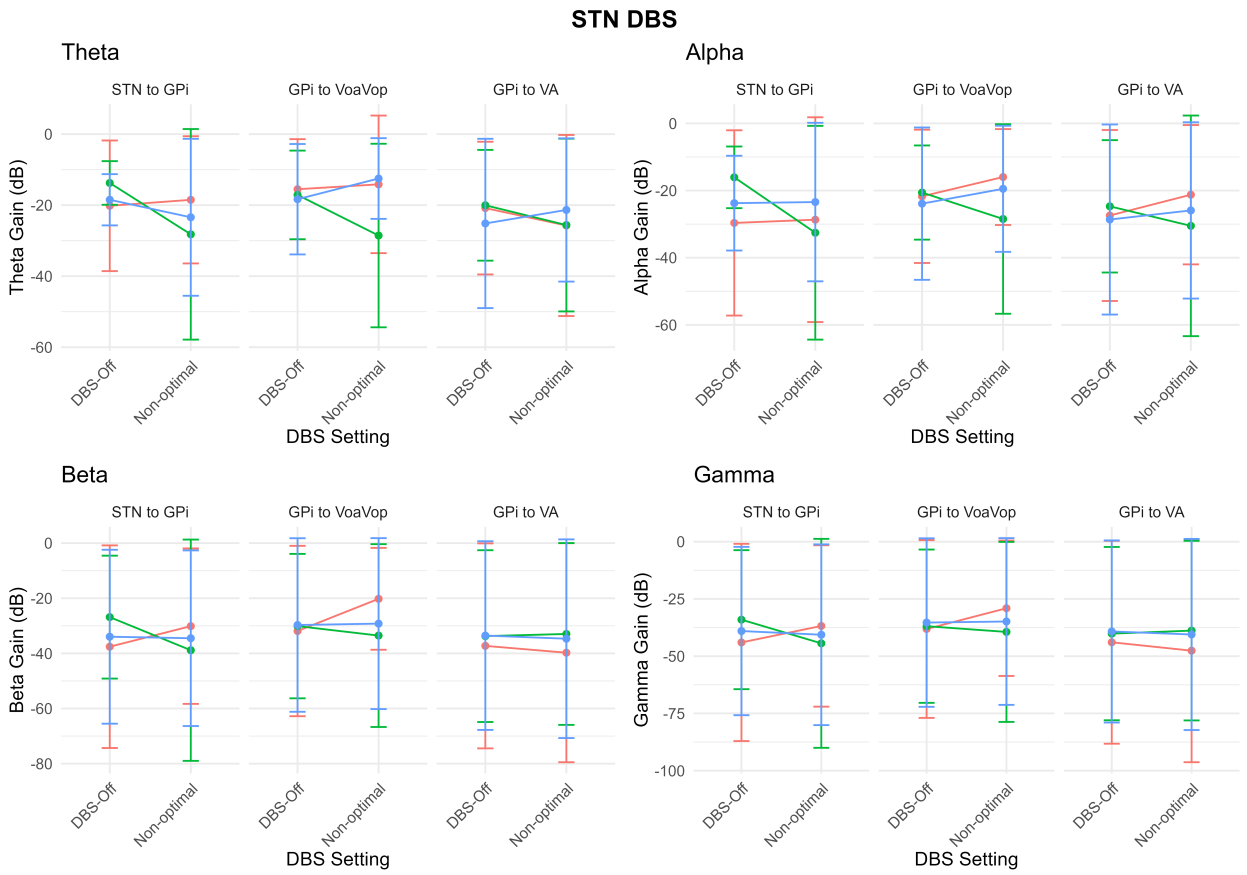

Figure 4.9: Effect of optimal versus non-optimal STN-DBS setting of transfer function gains, shown for each pathway and frequency band, for all patients.

Additional analysis: DBS modulates the oscillations associated with dystonic signals in deep brain regions

Previous studie of dystonic patients show abnormalities in low frequency activity in GPi and other motor sensory regions, such as STN, VoaVop and VA nuclei of thalamus. In this chapter we showed that DBS works in part by altering transmission of abnormal signals in low frequency bands between different brain regions. Here we want to examine and show that this effect can be both at the stimulation site (locally) and across deep brain regions (distant regions). In other words, we hypothesize that DBS modulates the abnormal projections onto thalamic motor subnuclei by changing the pattern of transmission in pallido-thalamic network, as a result of local and global changes in deep brain regions low frequency

oscillations. To test this hypothesis, we performed a similar analysis on the power spectra of each region with and without the DBS. Furthermore, to evaluate the differences between the optimal versus non-optimal DBS settings for our patients, we analyzed the effect of clinically effective DBS on the PSDs and compared that with the effect of non-optimal DBS. The results from the PSD analysis confirms an increase and decrease in power that are both local and global in all regions. We confirmed the presented results (increased transmission from GPi to VoaVop) by showing that while stimulating in GPi, the GPi power effectively decreases and the VoaVop and VA powers increase significantly from baseline, resulting in increased transfer function gains from GPi to thalamic subnuclei. This also can be confirmed by the known fact that GPi projections onto thalamic nuclei is inhibitory, therefore decreased GPi activity essentially leads to increased VoaVop activity and increased transfer function gain. The group analysis on the clinically effective setting showed that the clinical DBS decreases the oscillations in all regions. The optimal GPi DBS showed significantly smaller VA, VoaVop, and STN activity in all bands versus non-optimal setting. However, GPi-DBS in optimal setting led to a significantly higher GPi power in theta and alpha bands compared to the non-optimal setting, which again confirms our results from the transfer function study. These results elicit a better understanding of the mechanism and effects of DBS.

effect of stimulation frequency

4.4.3 optimal versus non-optimal stimulation setting effect on power

4.5 Discussion

DBS is commonly used as a neuromodulatory intervention for a various movement and neurological disorders [127], including Parkinson's disease, dystonia [207], essential tremor [143], epilepsy [250], and Alzheimer's disease [152], as well as psychiatric disorders such as obses-

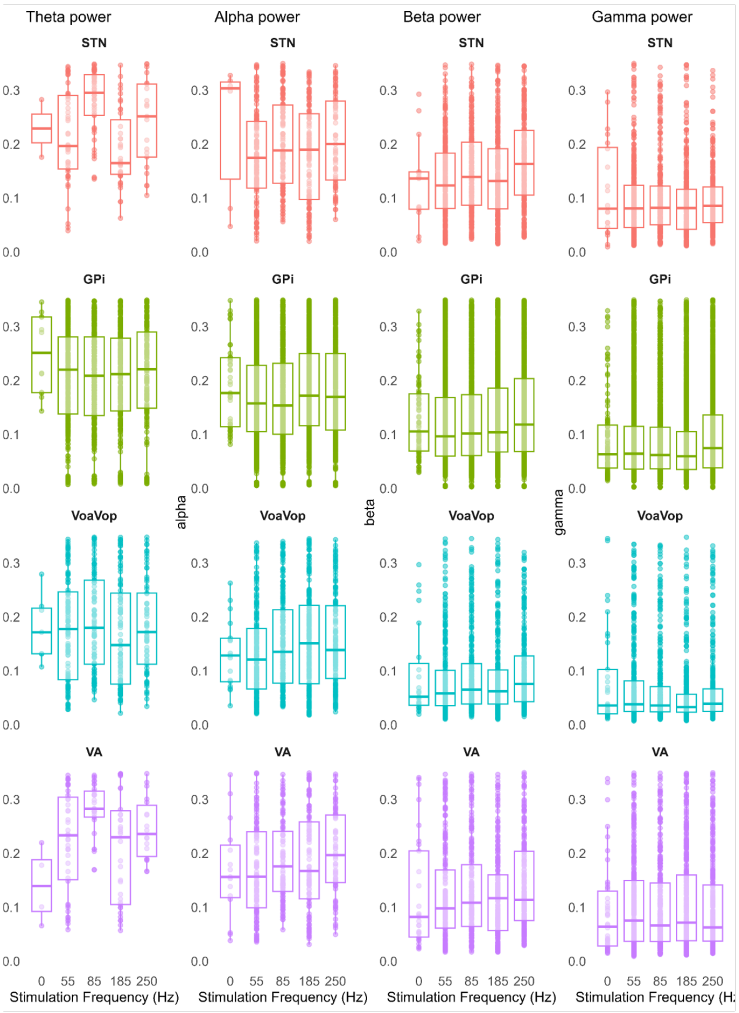

Figure 4.10: GPi stimulation: stimulation frequency effect on theta, alpha, beta, and gamma band powers in STN, GPi, VoaVop, and VA

sive compulsive disorder [148] and major depression disorder [55]. However, it is important to know that the mechanism of DBS remains largely unknown. The work done in this study suggests that GPi-DBS and STN-DBS affect the physiological connectivity and transmission patterns between deep brain areas in the motor circuitry, similar with the patterns of evoked responses across deep brain regions [220, 117, 103]. As such, a possible mechanism of DBS could be to restore balance in direct and indirect pathway gains through suppression or facilitation of indirect or direct pathway activity propagating between pallidum and thalamus.

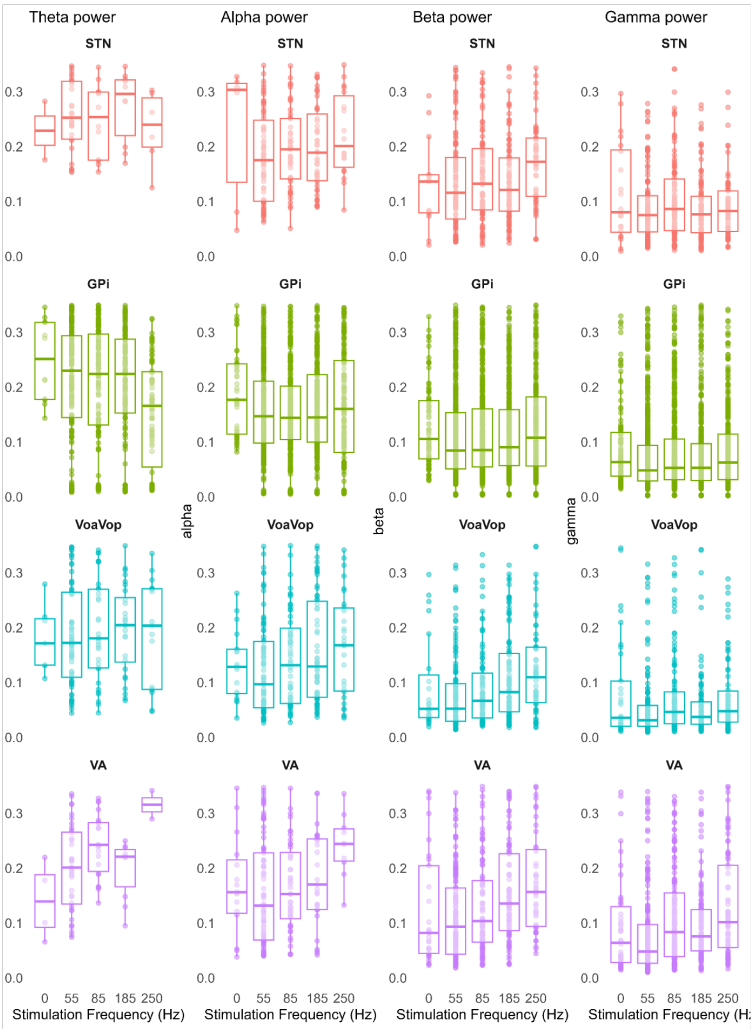

Figure 4.11: STN stimulation: stimulation frequency effect on theta, alpha, beta, and gamma band powers in STN, GPi, VoaVop, and VA

GPi-DBS affects the neural transmission from STN to GPi, GPi to VoaVoa, and GPi to VA, such that the transfer function gains during during all DBS settings, presented in this work, increase significantly from baseline. Our results supports that GPi-DBS increases the GPi-VoaVop gain more that it affects the other two pathways (STN to GPi and GPi to VA) in beta and gamma bands, but not in theta and alpha bands. This observations supports this hypothesis that GPi-DBS perhaps works by jamming the pallido-thalamic projection (GPi-VoaVop) by facilitating the transmission of higher frequency and blocking the transmission of lower frequencies, as supported by Figure 4.5. However, no significant effects of the stimulation frequencies were observed on these gains during GPi-DBS. To

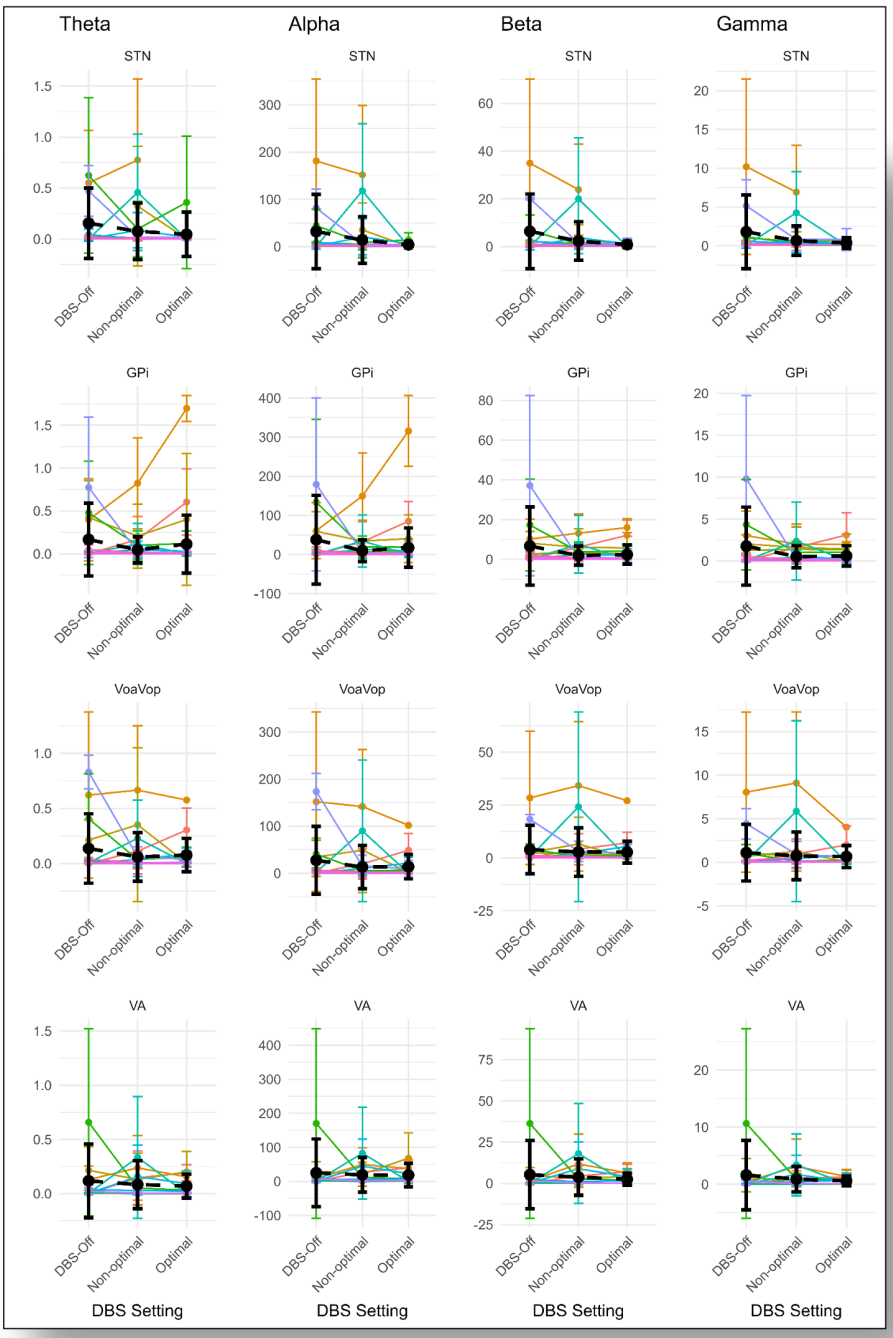

Figure 4.12: GPi stimulation: DBS-off, non-optimal, and optimal stimulation setting (stimulation frequency, stimulation lead contact and location): in theta, alpha, beta, and gamma bands (N=13)

summarize, during GPi-DBS, due to the excitatory output of STN and inhibitory output of GPi, the significant decreased STN-GPi gain with respect to the GPi-VoaVop could imply: 1)

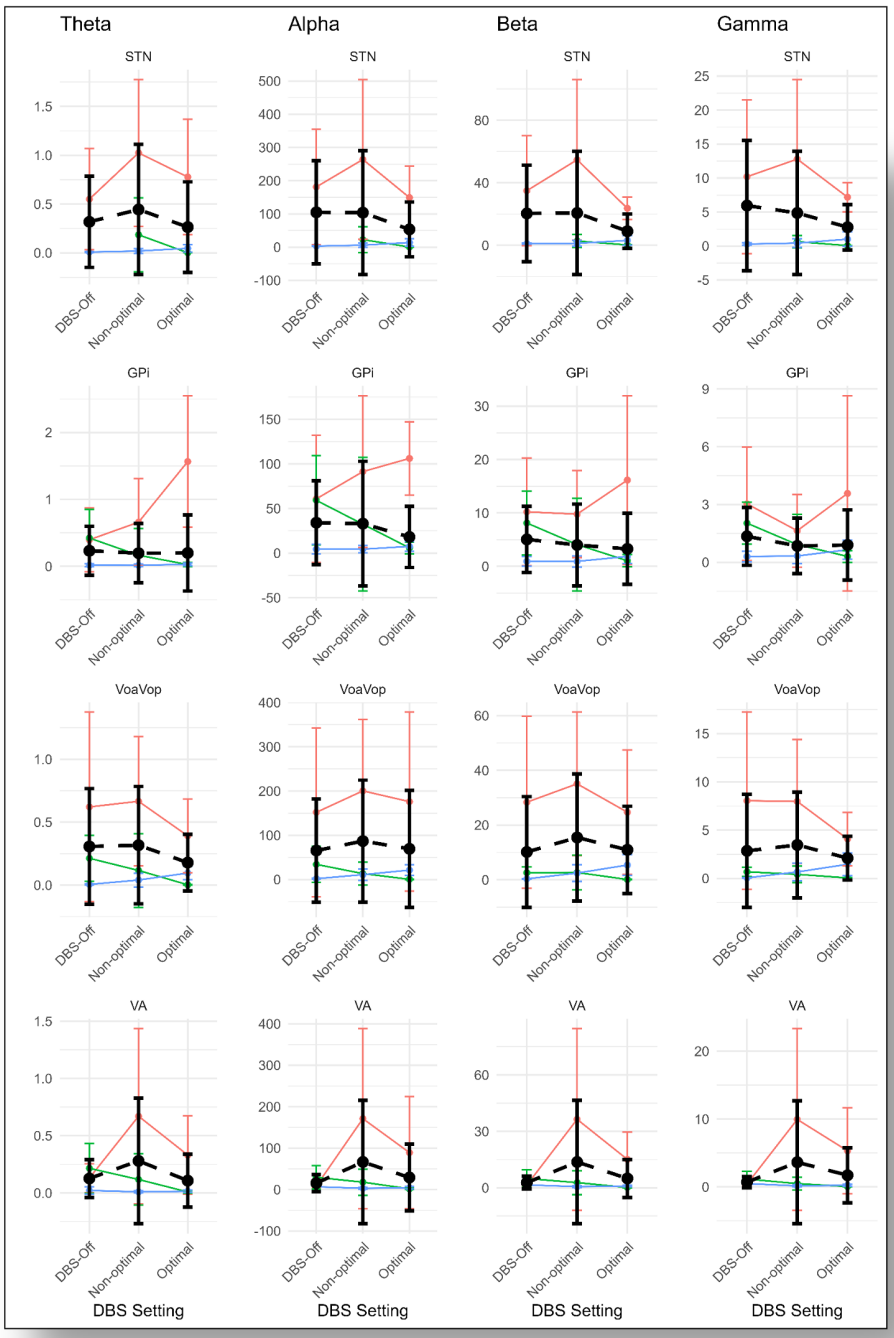

Figure 4.13: STN stimulation: DBS-off, non-optimal, and optimal stimulation setting (stimulation frequency, stimulation lead contact and location): in theta, alpha, beta, and gamma bands (N=3)

the GPi-DBS, potentially, reduces the excitability of GPi compared to other regions, resulting in disinhibition of thalamic subnuclei (VoaVop and VA). 2) GPi-DBS blocks the projections

of neural activity from GPi to thalamic nuclei by adding noise and decreasing the signal-to-noise ratio, rather than decreasing the abnormal signal projections in dystonia (theta band activity). 3) Decreased GPi activity or antidromically induced STN inhibtion, could lead to lower inhibition of thalamic nuclei, and subsequent increase in thalamic activity [39].

In addition, results from STN-DBS at 85 and 185 Hz, which are usually the chosen clinical stimulation frequencies for STN, showed significant increase of GPi-VoaVop gains in higher frequency bands, which means increased amplification of alpha, beta, and gamma signals from GPi to VoaVop. This means that perhaps STN DBS have more significant effect on downstream targets, decreasing GPi excitability, and as a result increasing the VoaVop activity in those specific bands. The group analysis and the analysis of the optimal clinical setting did not reveal any significant effect of STN-DBS on theta band. In addition, the fact that we did not observe significant changes in LFO transmission within pallido-thalamic network due to 55 and 250 Hz STN-DBS provides support for their therapeutic ineffectiveness. Another important feature of the STN-DBS results is facilitation of increased alpha, beta, and gamma transmission within all nuclei compared to the theta transmission. This may suggest that increasing the transmission of disorder-irrelevant activities (alpha, beta, and gamma) could lead to jamming the pathway to not allow for transmission of dystonic signals (theta band activity).

The limitations of this study includes the heterogeneity of the patients in terms of their symptomatology, underlying disease etiology, and their treatment approach (e.g. not everyone had VA lead or not all had VoaVop recording), leading to diverse effect of DBS across regions. However, the heterogeneity of subjects also provides justification for use of this technique in a wide range of patients. Moreover, we should consider that the methodology contains assumptions of linearity of the system which may not be true. The transmitted information between two regions in the control system model do not indicate that neural signals are actually transmitted through a direct pathway between those regions. For exam-

ple transmitted information, presented by the transfer function gains, could even be due to a common input to both nuclei. However, the regularization parameter used in the calculation of the transfer function accounts for other inputs to the output nuclei of the transfer function and correct for such errors, allowing us to infer valuable information from the computed transfer functions.

Another limitation is the presence of noise in low frequency bands especially close to the filter cutoff frequency (1 Hz), therefore the results of the delta band was not as reliable as results from higher frequency bands. In addition, important information may not be limited to the analyzed frequency bands (1-50 Hz).

In our method for calculation of the transfer functions we only calculate the signal amplification by computing the spectrum and magnitude of cross-spectrum of two signals; therefore, we do not take phase information into account. This is appropriate to our hypothesis which seeks to predict total information transmission and amplification between regions which is most affected by the transfer function gains. However, we acknowledge that the transfer function phase is important and contain very useful information about how the stimulation affects the phase; since it is highly possible that DBS introduces not only amplitude changes but also phase shifts that could affect the pattern of neural transmission. This will be an important topic for future analysis.

The use of data from micro-contacts is unique in this study, as most recorded information from DBS is either available from intraoperative microelectrode recordings, or postoperative macro-contact LFPs. Micro-contacts are likely to sample from a smaller target region than macro contacts and thus may provide more specificity to the analysis of information transmission, at the cost of sampling from a smaller target region. Comparison of this technique between micro-contacts and macro-contacts is an additional important topic for future work.

Chapter 5

Local field potential signal transmission is correlated with the anatomical connectivity measured by diffusion tractography

5.1 Abstract

In this chapter, we examine the correlation between diffusion tensor imaging (DTI) parameters of anatomical connectivity and characteristics of signal transmission obtained from patient-specific transfer function models. Here, we focused on elucidating the correlation between structural and functional neural connectivity within a cohort of patients diagnosed with dystonia. DTI images were obtained from twelve patients with dystonia prior to the deep brain stimulation (DBS) surgery. For each patient we processed the imaging data to estimate anatomical measures including fractional anisotropy (FA), axial diffusivity (AD),

number of fiber tracts per unit area (N), and fiber tract length (L). After the implantation of temporary depth leads for each patient as part of their treatment plan, intracranial signals were recorded. Transfer function models and the corresponding measures of functional connectivity were computed for each patient using local field potential (LFP) recordings. Generalized Linear Model (GLM) was then employed to determine the relationship between transfer function measures and DTI parameters. Our results illustrate a positive correlation between FA, AD, and intrinsic neural transmission measures, representing amplification and spread of intrinsic neural oscillations, obtained from the transfer functions models. However, no significant correlation was found between the functional connectivity and number of fiber tracts or fiber lengths. Our findings suggest that white matter integrity, as measured by FA and AD, can potentially reflect the amplification and spread of intrinsic brain signals throughout the network. This study underscores the significant relationship between structural and functional connectivity, offering valuable insights into propagation of neural activity in the brain network and potential implications for optimizing noninvasive treatments and planning for neurological disorders. The preprint of this chapter is available on MedRxiv (*doi: https://doi.org/10.1101/2024.04.14.24305803*).

5.2 Introduction

Advancements in neuroimaging techniques have fundamentally changed our understanding of brain functional and anatomical connectivity [248, 121]. Diffusion Tensor Imaging (DTI), as an advanced magnetic resonance imaging (MRI) modality, enables us to visualize white matter tracts that connect cortical and subcortical structures by measuring the motion of water molecules and provide us with valuable insights into the structural connectivity of the brain. With its capacity to reveal complex details of brain microstructure, DTI plays a significant role in optimizing procedures like deep brain stimula-

tion (DBS) [89, 47, 179, 146, 45, 2, 180, 46, 9, 48, 44, 43, 217, 8, 19, 26]. DBS procedure can be finely tuned by utilizing DTI to precisely map neural pathways and understand microstructural connections, promising improved treatment protocols and outcomes for patients suffering from neurological disorders [179].

Studying the relationship between structural and functional connectivity is an important domain of research for understanding the brain as a complex network of interconnected regions [124, 198, 197, 31, 77]. Previous studies have explored the complex relationships and communication patterns between different brain areas in various neurological disorders. For example such analysis in epilepsy helps to map the seizure network by exploring the relationships between the structural and functional networks responsible for conduction of epileptic activity [31]. Moreover, such studies have been conducted on healthy subjects to find the correlation between DTI measures and resting state functional MRI (fMRI). fMRI has lower spatial resolution than electrophysiology data and it does not capture the deep brain activity. On the other hand, it clearly reveals the cortical functional connectivity. This study showed that functional connectivity reflects structural connectivity to a large degree in cortical regions, although there is not a definite one-to-one mapping [80]. Despite all the research endeavors that provide invaluable insights into the interaction between structural and functional connectivity, the relationship between the two for transmission of non-epileptic brain signals remains unclear.

Transfer functions have been widely used to study the signal transmission and physiological connectivity within brain regions [196, 109]. For example, Kamali et al. [109] utilized characteristics of patient specific transfer function models of pathways in order to localize the seizure onset zones. In our previous studies, we have shown that transfer function models of deep brain regions can be used to replicate the evoked responses from DBS, informing us of existence of some relationship between the transmission of DBS pulses through neural pathways and the functional connectivity [113]. Moreover, we have shown that the DBS changes

the transfer function gains of deep brain regions meaning that DBS pulses have some effects on the functional connectivity. Building upon these fundamental studies that use transfer function methods, we aim to compute measures of signal transmission using patient specific transfer function models and find their relationship with structural characteristics provided by DTI measures, including fractional anisotropy (FA), axial diffusivity (AD), fiber length (L), and number of fibers per unit area (N), in basal ganglia and thalamic subnuclei. We hypothesize that the measures of signal amplification and transmission computed from transfer functions are positively correlated with the FA and AD. In other words, we hypothesise that the white matter integrity of the fibers and the diffusivity of neural pathways are reflected in functional connectivity represented by the transfer function measures.

In order to do so, we recorded signals from deep brain regions in twelve patients with dystonia, who underwent DBS procedure as part of their clinical evaluation. MRI, CT and DTI images were acquired and the DTI anatomical measures were calculated. Transfer functions representing each pathway for all patients were computed. We then compared the DTI measures and the transfer function signal transmission quantities using generalized linear model (GLM). Understanding the correlation and mapping between DTI parameters that can be calculated noninvasively and characteristics of transfer function models, which require invasive measurements from deep brain regions, offers invaluable insights into the relationship of brain structure and function and results in improvement of treatment protocols, planning, and outcomes.

5.3 Materials and Methods

5.3.1 Subjects and data

LFP recordings and imaging data from 12 patients (S2-3, S6-8, S12, s17-19, and s21-23 in Table 1) are used in this study.

5.3.2 Structural Connectivity

Structural image acquisition and processing

Preoperative MRI T1-weighted (structural MRI), DTI, and postoperative CT scans were obtained. Subsequently, the following steps were taken: 1) Pre-processing to correct distortions and motion artifacts of the DTI scans based on TOPUP and Eddy Current Correction algorithms [236]; 2) Co-registration of the DTI and postoperative CT images to the T1 anatomic volume; 3) Segmentation of all the subregions of the thalamus and pallidum; 4) Localization of sEEG leads using the attenuation in CT images; and 5) Estimation of micro-contacts' coordinates based on a linear model of the sEEG lead and assigning 3 mm diameter to the effective area [3].

Fiber tracking and DTI parameter estimation

In this study, DTI was employed to explore fiber orientations and measure diffusion properties. Micro-contact regions within each nucleus served as both origin and target regions for fiber tracking, enabling visualization of the anatomic pathways connecting the origin and the target. Using the diffusion tensor we computed several metrics to further characterize the fiber tracts linking these regions: 1) AD, calculated as the first eigenvalue (λ_1) of the

diffusion tensor, reflects water molecule diffusion along the principal axis of fiber tracts, indicating axonal integrity. Changes in AD can indicate axonal degeneration or demyelination [244]. 2) FA, a measure derived from the variance of eigenvalues (λ_1, λ_2, λ_3), quantifies the degree of anisotropy in water diffusion, offering insights into the coherence and density of fiber tracts. The calculation of FA is given by Equation 5.1, which is scaled between 0 (isotropic diffusion) and 1 (highly anisotropic diffusion). This provides direct insight into the structural integrity of axonal fibers [1]. 3) Number of fiber tracts per unit area (N) estimates the count of individual fiber bundles connecting two regions of interest and offers information about the density of fibers within that area [105]. 4) Fiber tract length indicates the total length of individual fiber tracts connecting two regions of interest and provides insights into the spatial extent or reach of neural pathways [51].

$$FA = \sqrt{\frac{1}{2}} \cdot \sqrt{\frac{(\lambda_1 - \lambda_2)^2 + (\lambda_2 - \lambda_3)^2 + (\lambda_3 - \lambda_1)^2}{\lambda_1^2 + \lambda_2^2 + \lambda_3^2}} \tag{5.1}$$

5.3.3 Functional Connectivity

Electrophisological data processing

The general data collection, protocols, and preprocessing are explained earlier in general methods.

Transfer Function Computation

The empirical transfer function of a system is computed as the ratio of the system's output Fourier transform (FT(Y)) to the system's input Fourier transform (FT(X)) which can be estimated as:

$$H(\omega) = \frac{FT(Y)}{FT(X)} \approx \frac{CPSD(X,Y)}{PSD(X) + \epsilon} \tag{5.2}$$

Similar to the transfer functions computed in chapter 4, PSD(X) is the power spectral density of the input, CPSD(X,Y) is the cross power spectral density between input signal and output signal, with complex numbers, and ϵ is a regularization constant. We computed the single input-single output (SISO) transfer function model between each two bipolar recording channels. After constructing the SISO transfer function models for each pair of channels, we want to investigate whether properties of magnitude of these transfer functions correlate with the anatomical features derived from DTI data. In other words, we want to evaluate how the characteristics of these transfer functions, representing functional connectivity, are related to the anatomical connectivity in the brain and to confirm whether they contain useful information about the anatomical features of the neural fibers. Note that the computed transfer functions are complex functions, which includes information about the phase and magnitude. Here, we only use the magnitude of these transfer function, and not the phase shifts and delays [113].

We computed two parameters representing the characteristics of intrinsic signal transmission from transfer function models as depicted in Figure 5.1. First parameter is the peak gain or the maximum transfer function gain (P_1 in Figure 5.1), which represents the maximum level of amplification of the transmitted input signal. In other words, it is a metric that quantifies how much input signals can be amplified and spread in the network at the maximum gain frequency. The larger the gain, the more propagation and amplification of neural activity throughout the network at that frequency. The second parameter is the peak-to-floor (PF) ratio which represents the large system responses and its fast magnitude drop-off [109]. PF ratio is calculated as the ratio between peak of the frequency response and its magnitude

at the roll-off frequency (P_2 in Figure.5.1). The roll-off frequency is the boundary where the energy flowing through a system begins to drop, defined as the frequency at which the dB magnitude is 3dB below the gain at frequency 0 $\omega = 0$ (DC gain) or where the power drops to half the power at $\omega = 0$, as P_2 in Fig.5.1. For a given pathway, we calculated the frequency response magnitude of all the SISO transfer functions as quantified by the magnitude of $H(\omega)$. Thereafter, we computed the PF ratio as:

$$PF\ ratio = log_{10}\frac{|H(\omega_{\mathrm{p}})|}{|H(\omega_{\mathrm{f}})|} \tag{5.3}$$

where ω_{p} represents the frequency at which maximum gain ($H(\omega_{\mathrm{p}})$) is achieved and ω_{f} is roll-off frequency and $H(\omega_{\mathrm{f}})$ is the transfer function gain at the roll-off frequency. All these measure were computed for each pair of electrodes, per hemisphere.

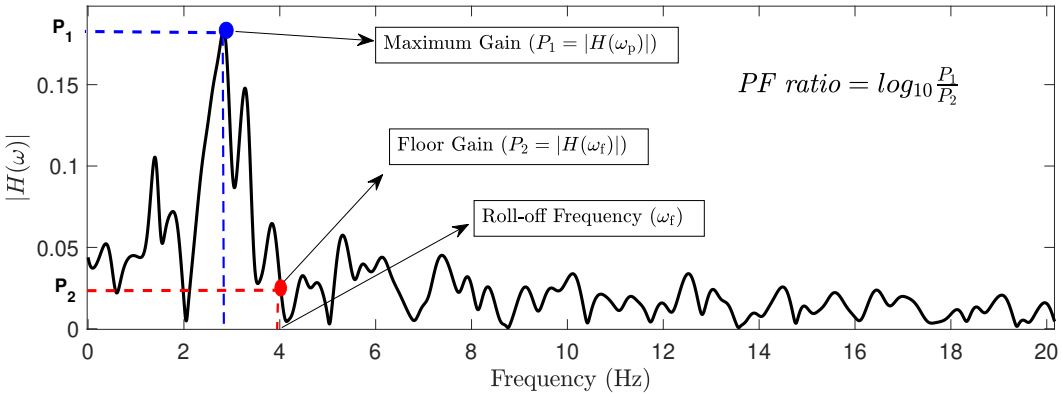

Figure 5.1: This figure illustrates the magnitude plot of a sample transfer function, showcasing key parameters including maximum gain, floor gain, and roll-off frequency. The PF ratio is determined by calculating the ratio between P_1 and P_2.

5.4 Results

In order to evaluate the relationship between the DTI and transfer function measures, first, all the variables were standardized. For each patient, we removed the outliers and kept the samples within 3 standard deviation from the mean. We removed the samples for which the max gain occurs below 2Hz as the data could be distorted in vicinity of 1 Hz cutoff frequency. We employed a GLM from the Gaussian family to model the PF ratio and the maximum gain in relation to FA, AD, N, and L for group analysis. Each predictor variable was chosen based on theoretical considerations and previous empirical findings suggesting their relevance to the functional connectivity. In addition, GLM allowed us to accommodate the normal distribution of our response variables, providing a robust framework for examining and assessing the strength and significance of the linear relationships between our predictors (FA, AD, N, and L) and our outcomes of interest (maximum gain and PF ratio). Our analysis aimed to elucidate the complex relationship between these variables with the PF ratio and maximum gain. Figure 5.2 shows a visualization of three distinct pathways from the GPi to VoaVop in a single patient, exemplifying such relationship. The significance of the estimated coefficients were then tested by Wald statistic and the p-values were computed from the test statistic based on chi-squared distribution with threshold of 0.05. We adjusted all the p-values using Bonferroni method after. In addition, the Variance Inflation Factors (VIF) were calculated to ensure that collinearity is negligible in the models, affirming the robustness and reliability of our statistical results. All the statistical analysis were done in R-studio.

Evaluation of the relationship between the PF ratio ($R^2 = 0.018$) and maximum gain ($R^2 = 0.019$) with FA, AD, N, and L indicated a significant positive correlation between both the PF ratio and maximum gain with FA and AD, as illustrated in Fig. 5.3 and Fig. 5.4. Conversely, the analysis showed no statistically significant correlation between PF ratio and maximum gain with either fiber length (L) or the number of fibers per unit area (N) (Figures 5.3

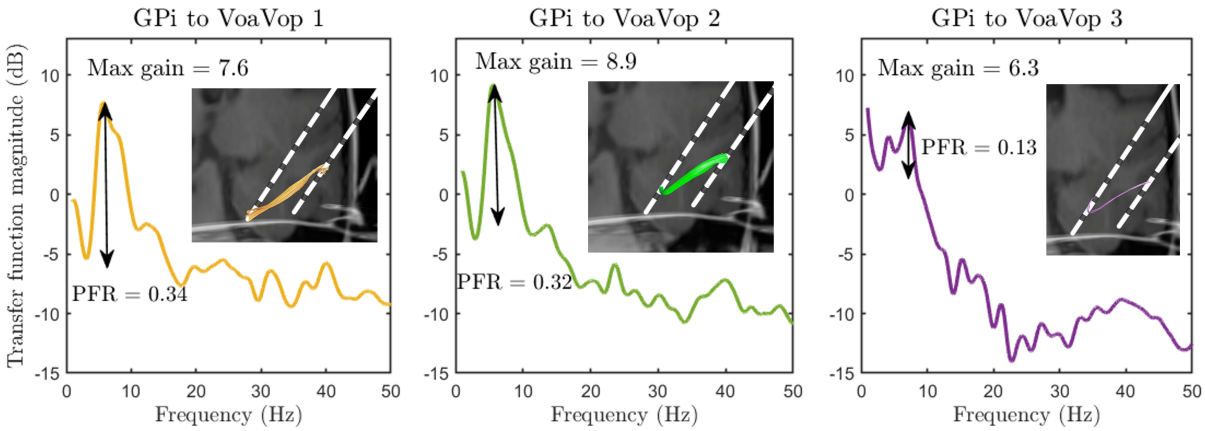

Figure 5.2: This figure illustrates a sample of three unique neural pathways from GPi to VoaVop for one patient, each characterized by varying fiber sizes and integrity levels. Accompanying each pathway is its respective transfer function magnitude plot. Maximum gain and the PF ratio are annotated on each plot for clarity. The larger fibers represented in the left ($FA = 0.40,\ AD = 1.35,\ L = 16.5,\ total\ N = 3$) and middle ($FA = 0.42,\ AD = 1.38,\ L = 18.8,\ total\ N = 132$) plots exhibit higher maximum gain and PF ratio values. Conversely, the pathway depicted in the right ($FA = 0.38,\ AD = 1.2,\ L = 20.07,\ total\ N = 45$) plot, characterized by smaller FA and AD has lower maximum gain and PF ratio, underscoring the relationship between the structural characteristics and functional connectivity.

Table 5.1: Statistical outcomes from the Generalized Linear Model (GLM) fitting for PF ratio and maximum gain in relation to FA, AD, N, and L.

DTI measures	Intercept [CI]	FA [CI]	AD [CI]	N [CI]	L [CI]	R^2
PF ratio	**-0.07** [-0.12, -0.03]	**0.07** [0.02, 0.13]	**0.11** [0.04, 0.17]	-0.07 [-0.14, 0]	-0.06 [-0.12, 0.01]	.018
Maximum gain	**-0.07** [-0.12, -0.02]	**0.11** [0.05, 0.16]	**0.08** [0.02, 0.15]	-0.03 [-0.10, 0.05]	-0.02 [-0.09, 0.04]	.019

and 5.4). The results of this GLM analysis are presented in Table 5.1, where we detail the estimated effects, confidence intervals, and statistical significance of each predictor.

5.5 Discussion

Several research studies to date focused on integrating structural and functional connectivity in order to understand how they correlate and the mutual information they share with one another [134, 12, 75, 194, 97, 218, 120, 135]. These investigations predominantly depend on

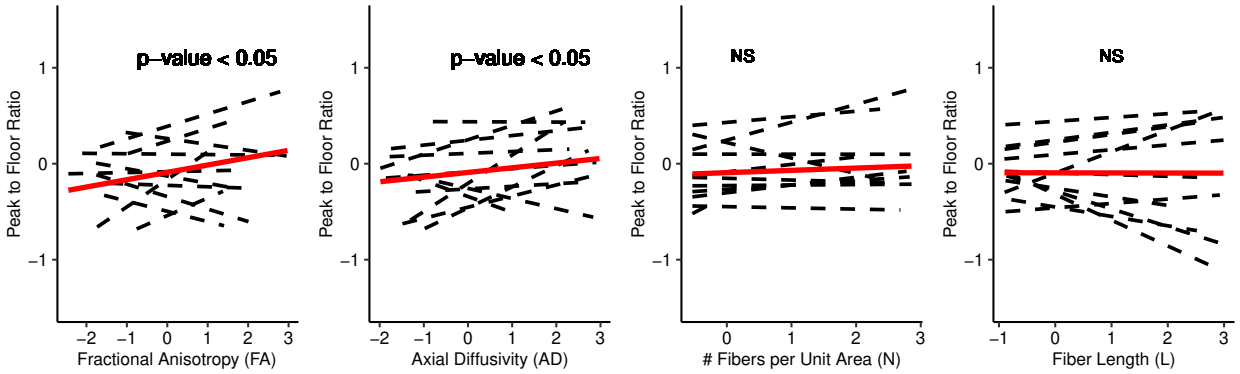

Figure 5.3: Illustration of the GLM fits and the statistical significance between the PF ratio and DTI measures. Individual subject PF ratios are depicted by dashed black lines and the solid red lines represent the GLM fit for group analysis. The figure highlights the significant correlation ($p - value < 0.05$) of PF ratio with Functional Anisotropy (FA) and Axial Diffusivity (AD) and the absence of significant correlation (NS) between PF ratio with number of tracts per unit area (N) and fiber length (L).

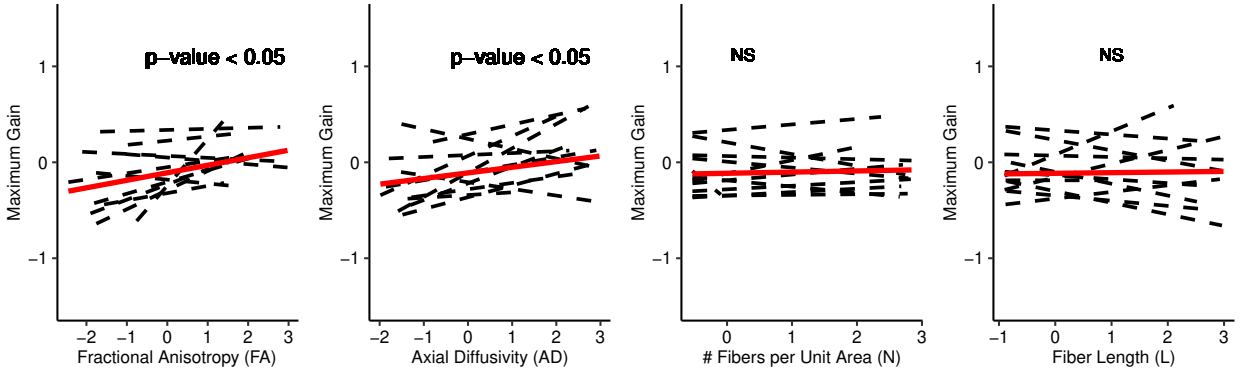

Figure 5.4: Illustration of the GLM fits and the statistical significance between the maximum gains and DTI measures. Individual subject maximum gains are depicted by dashed black lines and the solid red lines represent the GLM fit for group analysis. The figure highlights the significant correlation ($p - value < 0.05$) of maximum gain with Functional Anisotropy (FA) and Axial Diffusivity (AD) and the absence of a correlation between maximum gain with number of tracts per unit area (N) and fiber length (L).

modalities such as electro-encephalography (EEG) and fMRI for assessing functional connectivity, while employing DTI to assess structural connectivity. However, despite significant insights offered by these studies, this relationship is still poorly understood. Notably, limitations such as the relatively low spatial resolution of EEG and the low temporal resolution of fMRI prevents us from conducting precise localization and capturing of rapid neural dynam-

ics while assessing functional connectivity [76, 25]. Thus, it seems necessary to employ other modalities to fully address the relationship between structural and functional connectivity in the brain.

Here in this paper, we aimed to study the relationship between DTI parameters and characteristics of patient-specific transfer function models obtained from brain intrinsic neural activity. Thus, we investigated the correlation between FA, AD, Number of fiber tracts per unit area (N), and fiber tract length (L) as DTI parameters with maximum transfer function gain and PF ratio. Our results, consistent with previous works done on the relationship between the functional and anatomical connectivity [134, 12, 75, 194, 97, 218, 120, 135], provide further evidence of the relationship between anatomical and functional connectivity. In particular, our results highlight positive correlation between FA and AD with both characteristic of transfer function models (i.e., PF ratio and maximum gain). Significant positive correlation between FA and maximum transfer function gain shows that axonal fibers with higher integrity can better amplify and spread an intrinsic brain signal throughout the brain network. FA significant positive correlation with PF ratio suggests that axonal fibers with higher integrity have the capacity to provide larger system response and signal transmission. Significant positive correlation of maximum transfer function gain and PF ratio with AD suggests that the maximum level of signal amplification and fast magnitude drop-offs happen with higher magnitudes of diffusion parallel to fiber tracts.

In addition, Abe et al. previously provided evidence on the correlation between DTI parameters (i.e., FA, tract length, and tract diameter) and characteristics of DBS evoked potentials (EPs) [3]. Their results suggest that the integrity of white matter tracts plays a crucial role in determining the efficiency, strength, and transmission speed of DBS-induced signals. Moreover, Kasiri et al. [113] demonstrated through a patient-specific transfer function approach that DBS pulses travel along normal pathways from the stimulation site to distant targets in the brain. These studies collectively highlight the varied role of DTI parameters,

such as FA and AD, not only in providing insights into anatomical connectivity, but also in explaining information about neural signal transmission in the brain.

5.6 Limitation

As a non-invasive imaging technique, DTI provides valuable information about the white matter micro-structure which enables their visualization in 3D and facilitates studies on brain injures. However, similar to any imaging technique it has certain limitations. First, such computations of anatomical connectivity relies on the orientation of fibers which might result in inaccuracies in regions where the fibers interactions are complex [104]. Second, DTI has low image resolution, limiting its ability to identify single nerve fibers or small fiber bundles. Moreover, it is sensitive to noise and artifacts; therefore we require precise motion control and post-processing approaches. To better utilize DTI, integration with other imaging techniques and clinical data is necessary [104]. This is why we, previously, used DBS measurements to validate and confirm the effectiveness and accuracy of our DTI measurements for clinical applications [3].

In addition, it is crucial to acknowledge the limitations associated with Linear Time-Invariant (LTI) models, including transfer function analysis, which we employed to model the signal transmission between different nuclei in the deep brain regions. LTI models may not fully and accurately capture the dynamic and nonlinear nature of brain function. The brain's complex and adaptive nature might involve time-varying dynamics that cannot be adequately addressed by LTI models.

Moreover, the transfer function gains here do not indicate that the information is transmitted through a direct pathway from input to the output of the pathway's system. Such measure can also indicate a common input to both system's input and output (two ends of

a pathway), whether there is a fiber between them or not. However, in this study, since we are investigating the correlation of anatomical connectivity with the functional connectivity, there always exists a tract between the input and output. Therefore, this concern in not valid here, although it is a valid concern in general.

5.7 Conclusion

In conclusion, our study into the relationship between DTI parameters and characteristics of patient-specific transfer function models provides further evidence for the existence of significant relationship between structural and functional connectivity, offering valuable insights into how white matter integrity affects intrinsic neural activity propagation in the brain network.

Chapter 6

Additional chapter: Effect of EMG-activated vibrotactile biofeedback on skill learning

6.1 Abstract

Dystonia is a movement disorder characterized by repeated and sustained muscle contractions causing abnormal movements. Dystonia distorts the voluntary pattern of muscle activity during movement and can interfere with performance of tasks. Furthermore, practice of movements does not lead to improved performance. Theoretical results suggest that sensory deficits may be a contributor to lack of improvement with practice. Prior results showing the presence of sensory deficits in children with secondary dystonia suggests that this may contribute to their impairment; thereforeimprovement of sensory function might improve motor performance. In this work, we propose that an augmented vibrotactile biofeedback may improve the motor learning in children with secondary dystonia by sensory awareness,

but not in children with primary dystonia, who do not have associated sensory deficits. We tested this hypothesis by measuring performance and examining the effects of a vibrotactile biofeedback, applied on a task-relevant muscle, on motor learning in children with both primary (genetic) and secondary (acquired) dystonia and healthy children during a point-to-point reaching movement as well as a cyclic trajectory-following task. The results from this study shows that the vibrotactile device can become an effective method of movement improvement only for cyclic and smooth tasks but not for point-to-point task in children with sensory dystonia.

This work was supported by the US National Institutes of Health (grant 1R01HD081346-01A and Subaward USC-POLIMI: 61430868) and by the Italian Ministry of Health (Ricerca Corrente 2015/2022 to E. Biffi). This was a joint research collaboration between multiple cites including Politecnicno de Milano, ISTITUTO CARLO BESTA, Milan, Italy; University of Southern California, Children's hospital, Los Angeles, California, USA; and IRCCS Eugenio Medea, Bosisio Parini, Italy.

6.2 Introduction

In the past decades, sensory awareness has shown to be an effective way to improve the motor performance [171, 14, 99, 33]. Previous studies suggest that we need to further investigate the artificial sensory feedback mechanism of action as a noninvasive option for improvement of skill learning [211]. On the other hand, to better understand the effect of brain network disorders on motor learning, it is important to first, identify the effect of sensory deficits on motor learning. It is evident from previous works that artificial augmentation of sensory function is effective in some adults' rehabilitation [211, 13], however, its effectiveness has not been explored in children with dystonia. Dystonia is a movement disorder that can be primary (genetic) or secondary (acquired, due to another underlying disorder such as

Cerebral Palsy) [5, 208, 209]. While medication and in some cases surgery can be effective at ameliorating motor symptoms, noninvasive non-medical treatments would be a welcome adjunct. Physical therapy is often ineffective at improving motor function in children with dystonia and one reason for this has been postulated as the "failure of motor learning" theory [201, 27]. This theory predicts that in the absence of sufficient sensory feedback during the performance of movement, practice will fail to improve performance despite adequate repetition.

Sensory deficits have been shown in several forms of dystonia, including adult-onset focal hand dystonia and in children with dystonia due to dyskinetic cerebral palsy (CP) [211], but not in primary generalized dystonia. Therefore, we conjecture that failure to improve function with practice in some children with dystonia may be due to the associated sensory deficits. If this is the case, then biofeedback would be predicted to enhance the sensory perception of movement and improve motor learning in children with dyskinetic CP, who have been shown to have sensory deficits [211]. Conversely, biofeedback would be predicted to have little or no effect when sensory deficits are not present. Here, we explore the possibility that an EMG-activated vibrotactile biofeedback device could improve symptoms in children with secondary dystonia [5], by measuring their motor performance and compare them with a group of healthy children and a group with genetic dystonia.

The speed-accuracy trade-off of Fitts' law explains the relationship between the speed of movement and the endpoint accuracy during a "fast" movement to a target [63, 144]. One of the explanations for this phenomenon is that the trade-off represents compensation for signal-dependent noise, so that moving more slowly reduces noise and therefore, increases accuracy [63, 144, 231, 210, 141]. In previous studies, it has been shown that speed-accuracy trade-off, which is a constraint for human movement, can be modified by practice and the quantitative relationship between speed and accuracy may be an indicator of skill in some tasks [141, 112, 202, 18, 40]. Moreover, in earlier work, we showed that children with ac-

quired dystonia are aware of their limitations and adjust their movements based on the large signal-dependent noise in their movement [210, 112, 87]; Because of the increased motor variability in children with dystonia, Fitts law is a good measure of the effect of dystonia on performance [141, 112, 18, 40, 142]. This, too, would be particularly relevant to children with dystonia, because improvement in the speed-accuracy relationship would represent a reduction in a deficit associated with dystonia.

We employed the principles of speed-accuracy trade-off, known as Fitt's law [63], to investigate whether augmented sensory feedback on a muscle can, potentially, be helpful to improve the movement of children with dystonia in performing two different tasks. In particular, we ask whether, in the presence of biofeedback, subjects can improve their maximum speed for a given accuracy or can improve their accuracy for a given speed. Furthermore, we evaluated their performance by looking into various measures related to kinematic data, governed by quantified speed-accuracy relationship, and muscle recruitment to discover whether there is a significant improvement associated with the vibrotactile biofeedback.

In this study, two sets of experiment protocols were designed; one of which is a point-to-point task, constrained by trajectory. In this task, the subject must carry a reflective marble with a spoon between two targets without dropping it, which forces trajectories with a smooth velocity profile. In addition, the vertical placement of the targets limits forward and lateral acceleration [141, 112] . The other experiment is a cyclic task, constrained by the speed of movement [142]. In the cyclic task, the participant must follow a figure-8 trajectory with their index finger while the speed of movement is controlled by a metronome [142]. By varying the task difficulty (parameters of the task constraints), the participants were free to choose their velocity profile in the first task [112] and choose their accuracy in the second task. Both cases will show improved performance if subjects are able to learn an improved speed-accuracy relationship; thus, we compared the learning and performance in children with acquired and genetic dystonia with healthy children, with and without the sensory

vibrotactile device.

6.3 Materials and methods

6.3.1 Patient selection

Total of forty-six children and young adults (ages 15.5 ± 4.4) were recruited to perform the experiments with their preferred (dominant or less dystonic) arm. Twenty-two of which were healthy subjects, thirteen were diagnosed with acquired dystonia due to cerebral palsy and eleven were diagnosed with genetic dystonia. Subjects were diagnosed by a pediatric movement disorder specialist using standard criteria [102] in Children's hospital, Los Angeles (CHLA), in California, USA, Istituto Carlo Besta in Milan Italy, and IRCCS Medea in Ponte Lambro, Italy. They were selected for the study if they were able to perform the experimental tasks with either of their upper limbs. All patients provided signed informed consent for Health Insurance Portability and Accountability Act (HIPAA) authorization for the research use of protected health information if they were recruited in CHLA. Parents of participants recruited at IRCCS Medea signed a written informed consent. The protocol of the study was approved by the IRB of CHLA (reference number: CCI-11-00002) and the Ethical Committees of the Scientific Institute E. Medea (reference number: 054/14-CE; Date: 01-04-2015) and Istituto Carlo Besta. The experiments took place in three locations, University of Southern California (USC), and IRCCS Medea, and NearLab in Politecnico di Milano.

6.3.2 Experiment design and data recording

Subjects were asked to perform two tasks that are different in nature: In the spoon task, there is a smoothness constraint ("do not drop the marble") and subjects are asked to move as fast as possible [141]. In the figure-8 task, there is a time constraint indicated by a metronome, and subjects are asked to follow the trajectory as accurately as possible [142]. We executed testing and training blocks in five consecutive days with or without the vibrotactile device. After four weeks, they were asked to return and perform the same tasks for another 5 consecutive days. Those who performed the first week with the device, performed the second week without the device [32] and vice versa. The choice of the week to use the device was random to account for the learning effect. On each week (block of five days), they performed a testing trial on the beginning of the first day and ending of the fifth day in three different conditions (difficulties) for each task. They practiced the task after the testing trial on the first day, on days two, three, and four, and before the testing trial on day five [32]. See Figure 6.1 for a schematic of the experiment protocol.

Four Vicon Nexus 1.8.5 motion capture cameras (© Vicon Motion Systems Ltd, UK) at USC and eight optoelectronic cameras by BTS Bioengineering at Medea were placed around the subject to track the upper body kinematic data during both tasks, while the subjects were executing the tasks. The cameras were calibrated with a calibration wand and sampled at 100 Hz (USC) and 60 Hz (Medea). The cameras tracked 13-15 NDI Vicra Polaris passive reflective markers placed on the upper extremity muscles and joints. In addition, total of 8 surface electromyography (EMG) sensors were also placed on flexor carpi radialis (FCR), extensor carpi ulnaris (ECU), biceps, triceps, supraspinatus, anterior, posterior, and lateral deltoids. The EMGs were recorded using the Biometrics 8-channel wireless EMG system, sampled at 1000 Hz. In addition, we recorded the subjects' maximum voluntary contraction (MVC) for all 8 muscles, every day, prior to the onset of experiments. To record the MVC for each individual muscle, we positioned the subject in a way that facilitates the isolation of

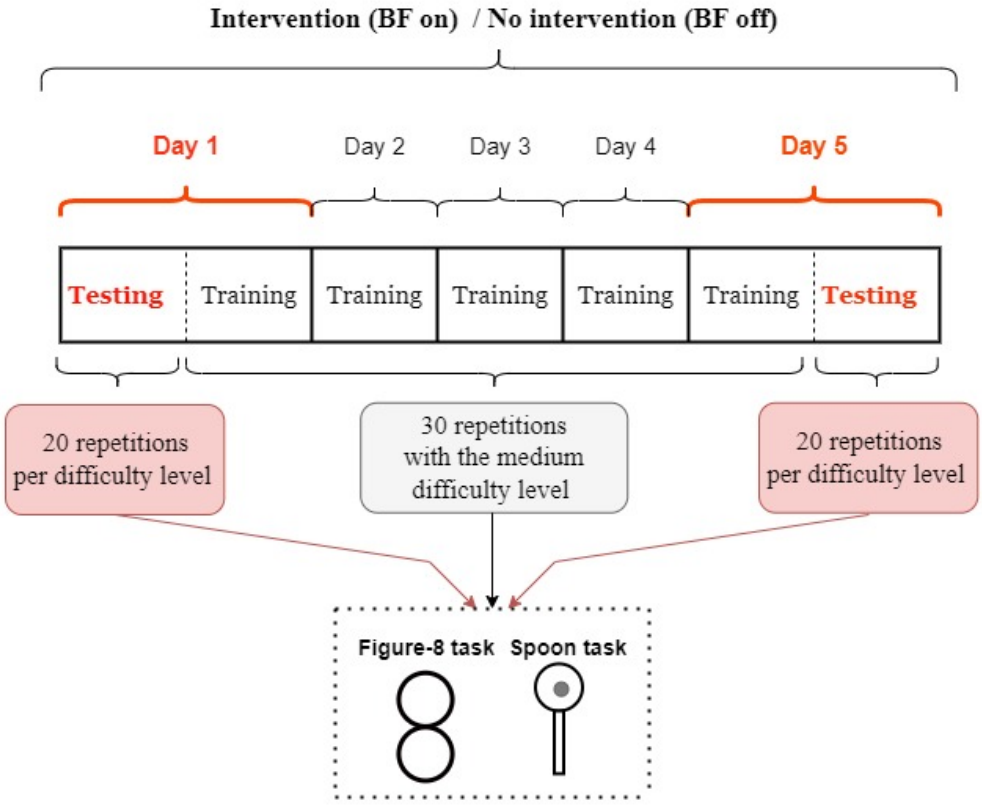

Figure 6.1: Experiment protocol sequences for week with or without intervention (biofeedback device). On each day they performed both spoon and figure-8 task. On the training days, they only practiced with the medium task difficulty (medium sized spoon and the middle metronome speed). On the testing days, they were tested with two additional easier and harder task difficulties.

that muscle. Initially, we recorded the baseline EMG, followed by instructing the participants to contract the isolated and stabilized muscle against resistance, maintaining an isometric contraction, for 5 seconds. The EMGs and motion capture system were synchronized by a trigger at the start of the movement. More accurate synchronization was done with signal processing and cross correlation of the signals. The EMG and motion capture sensors setup and placement are shown in Figure 6.2 A.

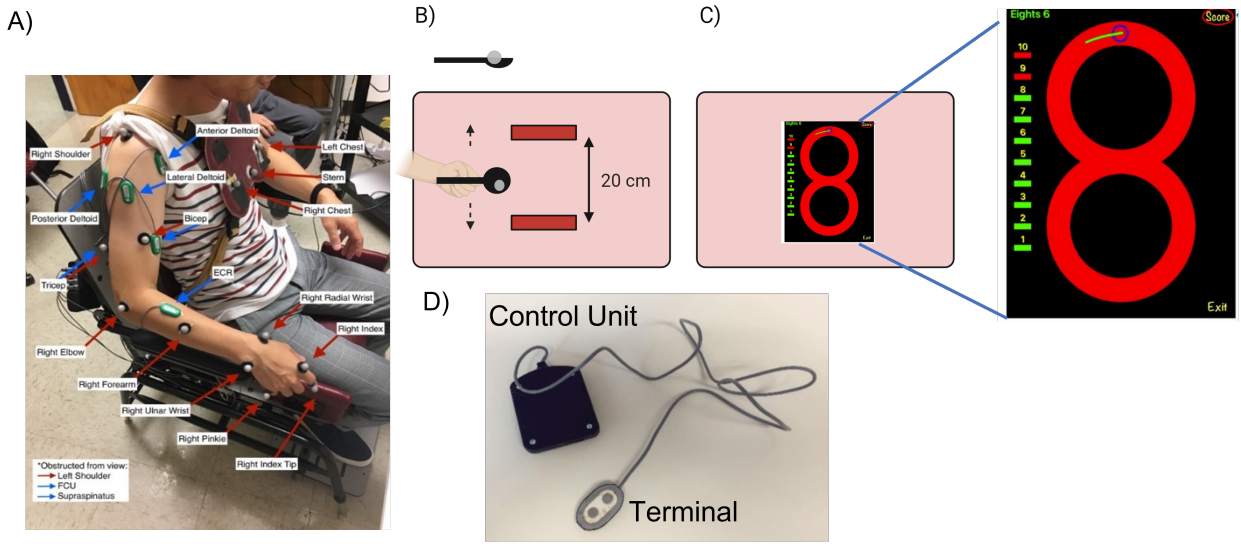

Figure 6.2: A. Kinematic reflective markers and EMG sensors placement. Total of 12 reflective markers were attached to the joints and limb to record the kinematic data. One additional marker was attached to the index finger in the figure 8 task to capture the finger trajectory. For the spoon task, one additional marker was attached to the spoon and one sphere marker was used as the marble in the spoon (total of 14); B. Spoon task setup: A board with two plastic blocks attached to it was placed on the table. The distance between blocks is 20 cm along the vertical axis. The participants started the task at the upper target while fully extending their arm; C. Figure-8 task setup and the iPad application: The scores are shown on the left side of the iPad app GUI. The subjects started the task at the blue dot above the figure-8, while fully extending their arm, and followed the red figure-8 trajectory line. They had to adjust their speed in a way to be on the top blue dot at each beep of the metronome; D. The vibrotactile biofeedback device; the terminal head contains the filtering circuit and the vibrating motor, and it would be attached to the target muscle. The control unit consists of the microcontroller and the circuit for battery recharging [32].

6.3.3 Spoon task

The subjects were seated upright on an adjustable chair and the severely affected dystonic subjects used their own wheelchair. A board with two targets was placed on a desk in front of them. The board's position was adjusted in a way that the subjects had to extend their arm fully to reach the more distant target. Each target was bounded by two plastic blocks and the distance between the center lines of these blocks was 20 cm along the direction of movement. A passive reflective marker was attached to the spoon, and an additional untethered spherical reflective marker was used as the marble carried by the spoon. The

Depth (mm)	3	6	9	12	15	18	30	33	66
IoD	6.33	3.16	2.11	1.58	1.26	1.05	0.63	0.57	0.28

Table 6.1: Details of spoon depths and their computed index of difficulty. The inner diameter of each spoon is 19mm. The index of difficulty is then computed as the ratio of diameter to depth of each spoon.

subjects were instructed to hold the reflective marble in the spoon and move the spoon back and forth between the two targets as fast as they could without dropping the marble. The experiment setup is shown in Figure 6.2 B [141, 112].

Nine different circular spoons of varying depth were designed in SolidWorks 2016 (Dassault Systems SOLIDWORKS Corporation) and were 3D printed. The index of difficulty for each trial was calculated based on the spoon dimensions [63, 141, 112]. For each spoon, we calculate the "index of difficulty (IoD)" as the ratio of the spoon diameter to its depth, noting that the marble size and the spoon diameter is constant. Therefore, the IoD is only dependent to the depth of each spoon. In other words, the index of difficulty is greater for shallower spoons, because stabilization of the marble in the spoon without dropping requires more precise attention to smoothness of the trajectory. The details of the spoon sizes and IoDs are reported in 6.1.

Each subject participated for 5 days on each week. On days one and five, both practice and performance testing occurred to determine baseline and improvement with practice. On days 2, 3, and 4, only practice occurred, as shown in Figure 6.1. Prior to initiating the experiment for each subject, performance was tested on a range of different spoon difficulties. Easy, medium, and difficult spoons sizes were chosen for each subject. The difficult spoon was chosen as the largest IoD for which the subject could successfully transport the marble dropping it on fewer than 30% of trials. The medium and easy spoons were the next 1 and 2 spoon difficulties below. Testing was performed on all three spoon sizes. Training took place only with the medium spoon size for each participant. Note that no specific cost was associated with dropping the marble, however if they dropped the marble three times or

more out of ten repetitions, they would be asked to redo the trial [141, 112].

We also asked the subjects to perform the task without the marble which allowed us to measure the maximum unconstrained speed and represents the true Fitt's law, based only on accuracy at the target endpoint without a constraint during the experiment. Note that unlike the standard Fitts' law formulations [63], the IoD used here reflects a property of the spoon, not a property of the target and target distance, and we have shown in previous work that this task follows the Fitt's law [141]. Furthermore, while increasing index of difficulty reflects the task difficulty at a given speed, there is no simple relationship between IoD and performance across all subjects, in part because there is a ceiling effect for the easiest spoons, and some subjects are unable to perform the task at all for the hardest spoons. Therefore, while there is a speed accuracy relationship, we do not expect this relationship to be linear.

6.3.4 Figure-8 task

The subjects were seated in a position similar to that of the spoon experiment. An iPad was placed in front of them, and they were instructed to follow a figure-8 trajectory on the iPad with their index finger, as depicted in Figure 6.2 C. The iPad's position was adjusted in a way that the subjects had to extend their arm fully to reach top point of the figure-8 trajectory with their index finger, maintaining the finger in contact with the surface of the screen. The figure-8's borders were of width 1 cm and they had to follow the trajectory clockwise or counter clockwise depending on the arm that they were performing the task with. In addition to the upper extremity markers, one extra marker was attached to the tip of their index finger to capture the finger movement trajectory [142, 32].

The experiment setup and protocol of testing and training was similar to that of the spoon task experiment. Similarly, prior to initiating the experiment for each subject, performance was tested on a range of different speeds (10 to 45 bmp), controlled by a metronome. The

fastest tempo was chosen as the most difficult task for which the subject could successfully follow the figure-8 with fewer than 30% failure of following the trajectory line. The medium and easy levels were the next lower 5 and 10 bpm. The figure-8 application on the iPad could detect if they are moving out of the allowed borders of the figure-8 and would mark that repetition as a failed one. It also saved the finger trajectory during the figure-8 task performance. Testing is performed on all three speeds, but training was performed only with the medium speed, and they were asked do the figure-8 for 10 repetitions on each trial. The first 5 repetitions were done with the metronome on and the next 5 repetitions we turned off the metronome and they had to remember the speed of movement. This was done so that subjects would move smoothly and continuously at several different speeds without stopping and waiting for the metronome pulse between each cycle. In addition, they were encouraged to make continuous movements, not stopping at any point on the iPad.

6.3.5 Vibrotactile biofeedback device

The vibrotactile biofeedback device, shown in Figure 6.2 D, contains a vibration motor and active differential electrode head that records the activity of the target muscle [32]. The vibration motor is at the head of the device so that the feedback is applied directly at the site of muscle-electrode contact for a clear and relevant stimulus. This electrode head is connected to a control unit that computes the amplitude of the recorded EMG signal through Bayesian estimation and controls the silent vibration motor with a rotation speed and amplitude proportional to the magnitude of the EMG. The processor and the nonlinear filter in the device are designed to allow for proportional biofeedback [203, 32]. In this study, we randomly selected the target muscle (the muscle that received the vibrotactile feedback), for each participant. The muscles were either the lateral or anterior deltoid. The selection of these two muscles was based on two consideration. First, they both play a role in performing both tasks, meaning that they are task relevant muscles. Second, it allowed us to confirm or

reject whether the choice target muscle is important in the effectiveness of the treatment.

6.3.6 Data processing and outcome measures

The data processing was performed in MATLAB R2020a (The MathWorks, Inc., Natick, MA, USA). All EMG signals were band-pass filtered at 2-200 Hz and normalized to the MVC. The kinematic data were reconstructed and interpolated using the Cortex 5.5 software (Motion analysis corp., Rohnert Park, CA, USA). After applying a low-pass filter at 5 Hz on the kinematic data, 2D joint coordinates were extracted from the 3D joint coordinates by applying principal component analysis (PCA) and using the first two principal components. The kinematic data and EMG were synchronized using the "xcorr" function in MATLAB, resampled to 1000 Hz, and divided into the repetitions of figure-8 or spoon task movement using the position of index finger or spoon. The segments of the spoon task where they dropped the marble and those segments of the figure-8 task where they removed their finger from the iPad were marked as outliers and removed from the dataset for the statistical analysis. Samples of a preprocessed EMG and kinematic data for for a healthy and a dystonic subject in one trial of spoon task are shown in Figure 6.3. Finally, The average movement time in two directions (x and y) were computed for every repetition. We then computed the following outcome measures derived from these segments and performed statistical analysis.

Spoon task outcome measures

Index of Performance (IP): We fitted a regression line to the movement time (MT) and the IoD and calculated the index of performance as the inverse of the MT-IoD linear equation slope for each subject [112]. The index of performance is used as a measure to evaluate if their improvement was significantly higher on the "biofeedback week (BF on)" compared to the "no-biofeedback week (BF off)" [63, 144, 231, 210, 141].

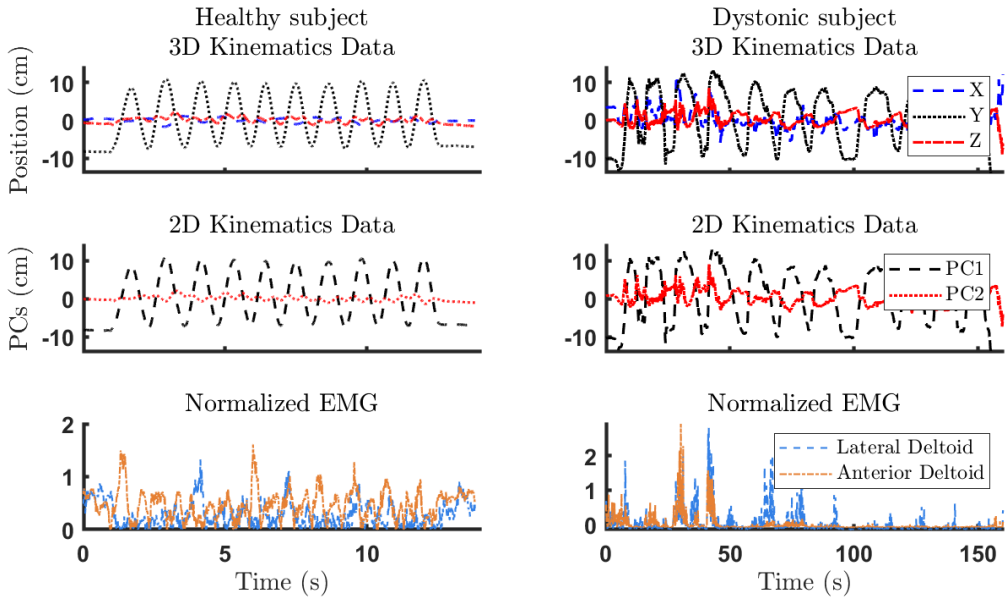

Figure 6.3: Samples of kinematic data and EMGs for a full trial of spoon task for a healthy (left) and a dystonic subject (right); (top) 3D kinematics data recorded during performance of the spoon task, in X, Y, and Z directions. (middle) First two principal components of X, Y, Z recordings. These two PCs were used throughout the alanysis. (bottom) Corresponding EMG recordings of anterior and lateral deltoid.

Co-contraction index (CCI): Co-contraction index is a useful parameter to evaluate the muscles' performance, especially in point-to-point tasks. Muscles co-activation plays an important role performing these tasks as sudden change of direction requires accurate and in-time activation of agonist and antagonist muscles [158]. This measure for a pair of agonist muscle and antagonist muscle at each repetition is computed as [199]:

$$CCI = mean\Big(\frac{min(EMG_i, EMG_j)}{max(EMG_i, EMG_j)}\Big) * \Big(min(EMG_i, EMG_j) + max(EMG_i, EMG_j)\Big) \quad (6.1)$$

in which, CCI is the co-contraction index, "min" is the minimum and "max" is the maximum of an EMG pair (EMG_i and EMG_j) at an instant in time.

In Figure 6.4 spectrums of X and Y for the healthy subject show peaks at 0.48 and 0.24

Hz, one exactly twice the other. The spectrums of the AD EMG only peaks at 0.24 Hz contributing the the movement only in X direction, while the LD EMG peaks at both task frequencies, contributing to movement in both X and Y directions. Although the spectrum of X and Y for dystonic subjects show two distinct peaks, the identified peaks are not as sharp as thos of healthy subjects and their frequency of occurrence are not exactly twice each other. The PSD of the LD and AD show two peaks only 0.51 and 0.21 Hz, contributing to the movements in both directions. Some overflow of activity in the LD is also observable at around 0.7 Hz.

Figure-8 task outcome measures

Time $*$ Error: This measure was computed as time $*$ error based on the Schmidt's law, a variation of Fitt's law, which studied how movement changes with speed in open-loop motions within thin lines (negligible trajectory width) [219]. It is computed by assuming that the movement is cyclic and is controlled with a metronome. Time in this formula and our experiment is the time required to complete a single figure-8 repetition, even if the subject goes outside the track. In this experiment the error is computed as [219, 253]:

$$\text{Error} = \sqrt{\frac{1}{N} * \sum_{t=1}^{N} d(t)^2} \tag{6.2}$$

Here, N is the number of samples, and $d(t)$ is given by:

$$d(t) = \frac{min(d_U, d_L) - \text{radius}}{\text{radius}} \tag{6.3}$$

in which d_U and d_L are the distances between the position and the upper and lower circles, respectively. The smaller the time $*$ error, the better the performance. Therefore, it should decrease with skill learning [219]. We compared this measure in figure-8 task with index of performance (IP) in the spoon task for the final evaluations.

Task correlation index (TCI): The figure-8 task is designed to capture both the task-relevant and task-irrelevant frequencies in the kinematic and EMG signals, as depicted in Figure 6.4. Since the task trajectory is symmetric, the frequency of the X component should be double that of the Y component, where for every four crossings in the x-direction, the subject makes two crossings in the y-direction. The significance of this is that it allows for the separation of the dystonic (task-irrelevant) frequencies from the task-relevant frequencies in the EMG or kinematic signals. This index is computed as:

$$TCI_i = \left(\frac{PSD_{EMGi}|f_x + PSD_{EMGi}|f_y}{PSD_{EMGi}}\right) \tag{6.4}$$

in which PSD_{EMGi} is the total power of the muscle i's EMG signal. $PSD_{EMGi}|f_x$ and $PSD_{EMGi}|f_y$ are the peak powers in X and Y directions, as marked in Figure 6.4. In other words, they are peak powers at the task frequencies. This index is bounded within 0 and 1 and the increased movement-muscle correlation means that the performance is better [142].

6.3.7 Statistical analyses

The statistical analyses on all the outcome measures were performed using lme4 [16] and emmeans [223] packages in R-studio (R core team, 2021). A Linear mixed effect model with repeated measures was employed to test the effect of practice on motor learning, with and without the vibrotactile biofeedback, for all outcome measures. For the spoon task outcome

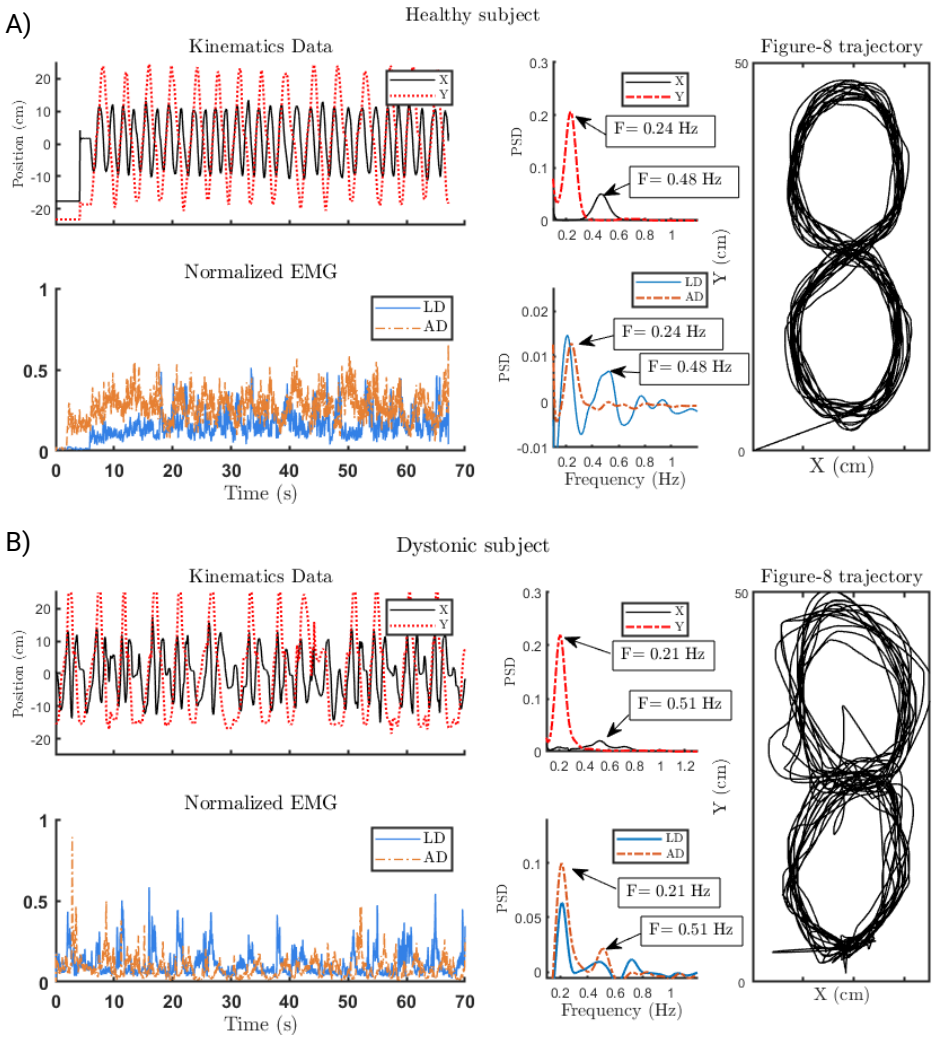

Figure 6.4: Recorded data during performance of the figure-8 task for a (A) healthy and a (B) dystonic subject. For each subject (top) 2D kinematics data in X and Y directions and their normalized spectrum, (bottom) the corresponding EMG recordings of anterior and lateral deltoid and their spectrum, and (right) their corresponding movement trajectory are depicted.

measures, we assessed the effect of biofeedback device (week 1 versus week 2), group (i.e., primary dystonia, secondary dystonia or healthy), testing day (i.e., day 1 or day 5), index of difficulty (IoD) and their interactions, as independent variables (fixed effects), on all the outcome measure by fitting a linear mixed effect model to the data. In this model, random effects are assumed to be intercepts for subjects and by-subject random slopes for the effect

of index of difficulty (equation 6.5). We, then, performed analysis of variance test (anova) and pairwise comparison to obtain the significance of each effect.

$$\text{Outcome measure} \sim \text{Testing day} * \text{Group} * \text{Week} * \text{IoD} \; + \; (\text{IoD} \mid \text{Subject}) \tag{6.5}$$

All the figure-8 task measures were normalized based on the speed of movement to remove the effect of task difficulty on our measures. Thereafter, we built the linear mixed effect model with the fixed and random effects chosen similar to that of the spoon task(Equation 6.6). We then performed anova and pairwise comparison to obtain the significance of each independent variables.

$$\text{Outcome measure} \sim \text{Testing day} * \text{Group} * \text{Week} + (1 \mid \text{Subject}) \tag{6.6}$$

6.4 Results

Spoon task:

The regression lines of movement time versus the index of difficulty ($R^2 = 0.96$) showed a significant p-value for all healthy children and children with acquired dystonia when there was no intervention during the practice (BF off week), which indicates learning. However, it seems that the children with secondary dystonia have not benefited from the sensory biofeedback in the spoon task experiment as shown in Figure 6.5a.

Due to the ineffectiveness of the biofeedback device on the spoon task performance, we then

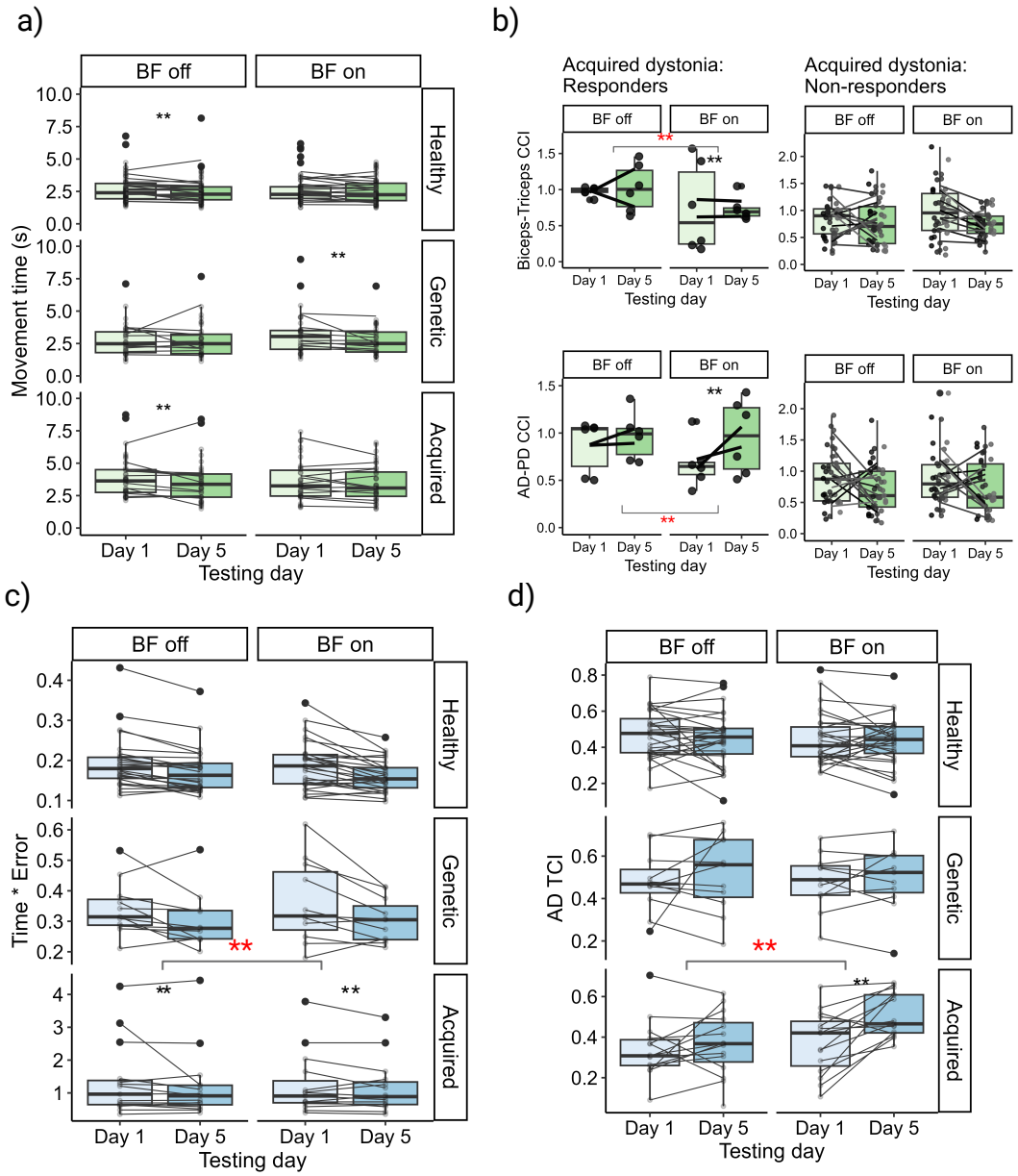

Figure 6.5: Statistical results of motor learning during the spoon task (a and b) and the figure-8 task (c,d); a) Average movement time, b) Biceps-triceps (top) and anterior-posterior (bottom) deltoid co-contraction indices for the acquired dystonic responder (left) and non-responder (right) groups, c) time $*$ error measurement, d) Anterior deltoid task correlation index, over three task difficulties before (day 1) and after (day 5) training with the biofeedback device (BF on) and without the biofeedback device (BF off) for healthy children, children with genetic (primary) and acquired (secondary) dystonia.

evaluated the change in co-contraction index (CCI) of FCR-ECU ($R^2 = 0.72$), biceps-triceps ($R^2 = 0.64$), and anterior-posterior deltoid ($R^2 = 0.72$), for a reponder group and a non-responder group of children with acquired dystonia. In order to do so, we separated those subjects who responded to the biofeedback (N=2) and those who did not (N=11). The pairwise comparison for each group revealed that the sensory biofeedback did not affect the CCIs in the non-responder group; however a significant pattern of change was observed in the responder group in both biceps-triceps and anterior-posterior deltoid CCIs ($p-vallue < 0.01$) as shown in Figure 6.5 (b).

In both tasks, the effect of the outcome measure calculated on the target muscle (vibrated muscle) was not significantly different from other muscles.

Figure-8 task

The linear fit ($R^2 = 0.88$) and the pairwise comparison for time∗error revealed that the this outcome measure decreased significantly ($p - value < .01$) for the children with acquired dystonia with the biofeedback device on, compared to the week that they practiced without the biofeedback ($mean_{\text{BF off vs BF on}} = 0.13$, $SE = 0.02$). Two other groups (healthy and primary dystonia) did not show sensitivity to the biofeedback device, however learning occurred on the BF-off week. The task correlation index for the anterior deltoid muscle ($R^2 = 0.57$) increased significantly ($p - value < .01$) for the children with acquired dystonia while performing the figure-8 task with the biofeedback device ($mean_{\text{Day 1 vs Day 5, BF on}} = 0.11$, $SE = 0.02$; $mean_{\text{BF off vs BF on}} = 0.05$, $SE = 0.01$) as shown in Figure 6.5. However, this measure did not change significantly in other muscles.

6.5 Discussion

In this study, we hypothesized that the vibrotactile device would be an effective device to improve skill learning in children with acquired dystonia because of their sensory deficit. But our results suggest that this hypothesis is only partially correct. In other words, our results show that the vibrotactile biofeedback device improved the motor learning in figure-8 task (continuous task), but not the spoon task (point-to-point task), meaning that children with acquired dystonia learned the figure-8 task significantly better, practicing with the biofeedback device. This device seemed to decrease the time or movement variation in children with acquired dystonia, which could possibly be the reason why we observed increased task correlation index of the anterior deltoid (task relevant muscle) in this group. On the other hand, this device does not seem to be very effective in improvement of learning the spoon task. There was no significant change in the smoothness or movement variation following the practice with the biofeedback device in children with dystonia as reported in the supplementary material. Nonetheless, it is observed that learning took place in the week without any intervention (BF off), as also shown in our previous study [112]. These results could be explained by the different nature of the two experimental tasks. The figure-8 task is a cyclic and continuous task which does not require very accurate muscle control and co-contraction, while the spoon experiment is a point-to-point task which requires more accurate muscle control, timing, and controlled agonist-antagonist co-contraction in order to change the direction of movement at each end of a forward or backward movements. Previous studies have shown that children with dystonia have failure in the timing of co-contraction, which is due to the involuntary activation of an antagonist muscle during the movement [249, 160], leading to increased co-contraction during the movement.

The analysis of co-contraction in acquired dystonic responder and non-responder group, in the spoon task, revealed that the biofeedback device affected the co-contraction of biceps-triceps and anterior-posterior deltoid pairs significantly in the responder group (whether

increased or decreased), while this effect was not significant in the non-responder group. We further hypothesize that in order for the treatment to be effective, the muscle co-contractions pattern have to change, and this change may be inconsistent among the subjects, as each has a different baseline, adopt a different approach, and their dystonia manifests onto different muscles. However, this must be tested as we only observed this in two participants (N-responder =2).

Another possibility is that the marble is effectively a biofeedback signal for movement, and this may have been more important in performance (drawing the attention to perform the task without dropping the marble) than the muscle EMG biofeedback, effectively drowning out any possible effect.

In this study, biofeedback enhanced performance in the figure-8 task but exhibited no improvement in the spoon task, indicating that mere practice is not adequate for achieving peak performance. The results in primary dystonia showed lack of improvement in either task. While this could occur due to multiple mechanisms, it is consistent with the hypothesis that biofeedback will improve movement only when a sensory deficit is at least partly responsible for poor movement and skill learning. This supports our initial hypothesis that secondary dystonia deficits might be partially due to learning failures stemming from sensory deficits. This proposition raises the potential for noninvasive treatments for secondary dystonia that center on augmenting sensation.

Chapter 7

Additional chapter: Improvement of speed-accuracy trade-off during practice of a point-to-point task

7.1 Abstract

The trade-off between speed and accuracy is a well-known constraint for human movement, but previous work has shown that this trade-off can be modified by practice, and the quantitative relationship between speed and accuracy may be an indicator of skill in some tasks. We have previously shown that children with dystonia are able to adapt their movement strategy in a ballistic throwing game to compensate for increased variability of movement. Here, we test whether children with dystonia can adapt and improve skills learned on a trajectory task. We use a novel task in which children move a spoon with a marble between two targets. Difficulty is modified by changing the depth of the spoon. Our results show that both healthy children and children with acquired dystonia move more slowly with the

more difficult spoons, and both groups improve the relationship between speed and spoon difficulty following 1 week of practice. By tracking the marble position in the spoon, we show that children with dystonia use a larger fraction of the available variability, whereas healthy children adopt a much safer strategy and remain farther from the margins, as well as learning to adapt and have more control over the marble's utilized area by practice. Together, our results show that both healthy children and children with dystonia choose trajectories that compensate for risk and inherent variability, and that the increased variability in dystonia can be modified with continued practice. This research was funded by NIH (1R01HD081346-01A1; 2013-2019; Subaward: 61430868) and it is a joint project and collaboration between multiple cites including Politecnicno de Milano, ISTITUTO CARLO BESTA, Milan, Italy; University of Southern California, Children's hospital, Los Angeles, California, USA; and IRCCS Eugenio Medea, Bosisio Parini, Italy. This chapter is published in *Journal of Neurophysiology, Volume 130, Issue 4, Pages 931-940 in October 2023.*

7.2 Introduction

The speed-accuracy trade-off known as Fitts'law is ubiquitous in human movement [63]. This law is typically formulated as a relationship between the speed of movement and the endpoint accuracy following a rapid or ballistic movement to the target [63, 40, 49, 87]. Although many possible explanations have been proposed, one of the more enduring possibilities is that the trade-off represents compensation for activity-dependent noise (signal-dependent noise), so moving more slowly may reduce noise and permit increased accuracy [40, 49, 87, 210, 141, 119]. More recently, it has been shown that Fitts'law also applies in tasks where the accuracy of the trajectory matters rather than only the accuracy at the final target [141]. Moreover, the quantitative relationship between speed and accuracy for any individual may be modifiable by practice, suggesting that this relationship may be related to the skill of

performance in trajectory-following tasks. A trajectory-following task involves a pre-specified movement and may not fully capture the subject's ability to plan a trajectory [49, 141]. Therefore, we have developed a novel task in which subjects must transport a marble in a spoon from one target to another [141]. By varying the depth of the spoon, the task can be made difficult, and subjects are free to choose not only the speed of movement but the complete velocity profile of the trajectory to reach the target as rapidly as possible. The size of the target is not varied, so the choice of trajectory is entirely determined by the spoon's difficulty. We have previously shown that this task exhibits a robust speed-accuracy trade-off [141], that is, the participants slow down in performing the more difficult tasks to not drop the marble. Previous work has shown that the speed-accuracy trade-off for a trajectory-following task can be modified with practice [49, 141, 202, 231]. Here, we test whether this trade-off can also be modified by practice for the marble-spoon task by analyzing the marble trajectory in the spoon area. We test this in both healthy children and children with acquired dystonia [235, 23, 5]. Dystonia is a disorder characterized by increased variability of movement and increased signal-dependent noise [202, 141, 235, 23]. Children with dystonia are aware of their increased noise and compensate appropriately in a ballistic target task [49, 87, 202, 141]. Here, we test how children in these two groups with different levels of signal-dependent noise adapt to the trajectory-following task by investigating if they adapt their strategy to lower the risk of movement [204, 178]. We also compared how performance in the two groups is affected by learning during practice over a period of 5 days.

Subjects	Diagnosis	Tested Arm BAD Score
Sb1*	Generalized dystonia due to hypoxic ischemic event	L3
Sb2	Chorea with underlying dystonia	R2
Sb3	Generalized dystonia s/p selective dorsal rhizotomy	L3
Sb4	Left-side dystonia due to mild periventricular leukomalacia (PVL)	L1
Sb5	Generalized dystonia; cerebral palsy	R3
Sb6	Generalized dystonia due to delayed C-section for maternal eclampsia	R3
Sb7	Encephalitis	R3
Sb8	Dyskinetic tetraplegic cerebral palsy due to ischemic injury	R3
Sb9	Generalized dystonia; ADEM	R3
Sb10	Emergency C-section; generalized dystonia	L3
Sb11	Generalized dystonia; cerebral palsy	R3
Sb12	Generalized dystonia; cerebral palsy	R2
Sb13	Encephalitis	L3

Table 7.1: Subjects' demographics: Participants are 8–20 yr old, including 12 males and 1 female subject. BAD, Barry–Albright Dystonia scale; L, left arm; R, right arm. *Subject 1 had deep brain stimulation electrodes in place; however, it was off during the experiment.

7.3 Materials and methods

7.3.1 Subjects

In this study, the data from 21 children and adolescents out of the 46 participants (aged 15.5 ± 3.4 yr) were used. We only included the participants for whom we had the recordings of the marble trajectory within the spoon (the marble kinematic recordings were not available for all the participants.). Eight (5 females and 3 males) were healthy subjects, while 13 (1 female and 12 males) were diagnosed with acquired dystonia. Details of the participants with secondary dystonia are provided in Table 7.1.

We only used the recordings of the spoon task, during the week without any intervention (no biofeedback). We proved that learning occurred on the week without the intervention, practicing the spoon task in both healthy children and those with acquired dystonia, in previous chapter. Here, we assess what measures change in these two groups to improve

motor learning. Therefore, we analyzed the kinematics of the marble inside the spoon as well as speed coefficient of variation and smoothness.

7.3.2 Speed-accuracy trade-off (Fitt's law)

We first tested the effect of IoD on speed and determined how this effect changed following practice [63]. We fitted a regression line to the movement time (MT) and the IoD and calculated the index of performance (IP) as the inverse of the MT-IoD linear equation slope for each subject. The index of performance [63, 210] is used as a measure to evaluate if their performance improved in day 5 compared with day 1. Statistical analyses were done by lme4 [16], emmeans [223] packages in R-studio (R core team, 2021). A Linear mixed effects model with repeated measures was used to analyze the effect of practice on performance. We assessed the effect of IoD, group (i.e., dystonia or healthy), and testing day (i.e., pre [day 1] or post [day2]), and their interactions as independent variables (fixed effects) on MT and speed of movement (dependent variables) by fitting a linear mixed effect model [16] to the data. In our model, random effects are assumed to be intercepts for subjects and by-subject random slopes for the effect of IoD. In the MT model, we assumed uncorrelated slopes and intercepts (Eq 7.1); however,we assumed correlated slopes and intercepts for the speed of movement linear model due to the singularity of fit (Eq. 7.2). We then performed an analysis of variance test (ANOVA) and pairwise comparison to obtain the significance of each effect.

$$MT \sim Testing\ day * group * IoD + (IoD \mid\mid subject) \tag{7.1}$$

$$Speed\ of\ movement \sim Testing\ day * group * IoD + (IoD \mid subject) \tag{7.2}$$

7.3.3 Marble kinematic analysis

If movement speed is limited by the risk of dropping the marble, then speed can be maximized by allowing the marble to move as much as possible within the spoon. We thus analyzed the marble position within the spoon during movement to determine whether maximal areas were used, or whether other considerations such as reduction of risk or physical constraints on movement speed were affecting the performance. The position of the marble inside the spoon lies approximately within an ellipse; thus, an ellipse was fitted to the marble trajectory for each repetition (one forward and one backward movement). This method enabled us to estimate how much of the spoon area is used to achieve the desired accuracy or speed.The eigenvalues of the movement trajectory (the ellipse diameter along the semi-major and the semi-minor axes) were then computed. We computed a safety margin with the two main eigenvalues, "a" and "b", as a measure to investigate the variability along the first eigenvector of the movement trajectory (e_1), and along the second eigenvector of the movement trajectory (e_2), respectively. This safety margin is computed based on Eqs. 7.3 and 7.4 to determine how sensitive each subject is to the risk of movement, before and after practice. Therefore, a smaller safety margin means that the subject is risk-seeking and therefore they use more of the available variability. Similarly, a larger safety margin means that the subject is risk-averse, and they use less of the available variability [178].

$$e_1\ safety\ margin = 100 * (1 - \frac{a}{spoon\ diameter}) \tag{7.3}$$

$$e_2\ safety\ margin = 100 * (1 - \frac{b}{spoon\ diameter}) \tag{7.4}$$

We explored how these ratios change with respect to speed of movement, IoD, and practice, for each subject. We used a repeated measure analysis with a linear mixed effect model to derive the statistical results of the change in these ratios with respect to the speed and IoDwith practice. In the mixed effect model, IoD, testing day, speed, and their interactions are the fixed effects. Similar to previous models, random effects are the intercepts for subjects and by-subject random slopes for the effect of the index of difficulty (Eq. 7.5). An analysis of variance test (ANOVA) and pairwise comparison were performed to obtain the significance of each effect.

$$Safety\ margin \sim Testing\ day * group * IoD + (IoD \mid subject) \tag{7.5}$$

7.3.4 Smoothness and coefficient of variation

In addition to analyzing the marble trajectory and movement time, we assessed the effect of practice on change in smoothness and variability. Dimensionless jerk score is a useful measure to investigate movement smoothness which was computed based on Eq. 7.6

$$Jerk\ score = \left(\int_{t_1}^{t_2} \dddot{x}(t)^2\, dt \right) \frac{D^5}{A^2}\ , \tag{7.6}$$

in which $D = t_2$–t_1 is the duration and A is the amplitude of movement (distance) [95]. In

addition, the coefficient of variation (CV) was derived as the ratio of the speed standard deviation (SD) to its mean for each repetition ($CV\% = \frac{SD(v)}{v}$) [191]. Similarly, a linear mixed effect model with repeated measures analysis was used to compare the smoothness and the coefficient of variation (CV) with respect to the groups, IoD, testing day, and their interactions.

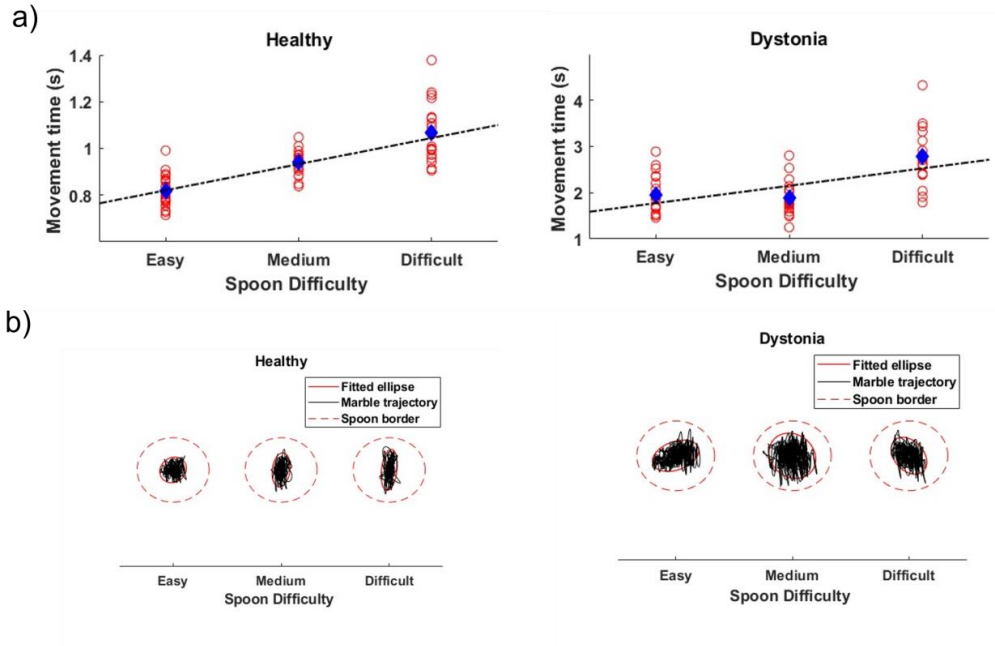

Figure 7.1: A: the movement time with respect to spoon sizes (easy, medium, and difficult) for a subject with dystonia (right) and a healthy subject (left) is shown with red dots for each repetition. The blue dot shows the average movement time for all repetitions in one trial and the dashed black regression line shows the increasing trend of movement time with respect to the spoon difficulty. B: the marble trajectory (black line) within the spoon border (dashed red line) and the fitted ellipse (solid red line) to that trajectory is shown for each spoon difficulty for one healthy subject (left) and one subject with dystonia (right) in one trial.

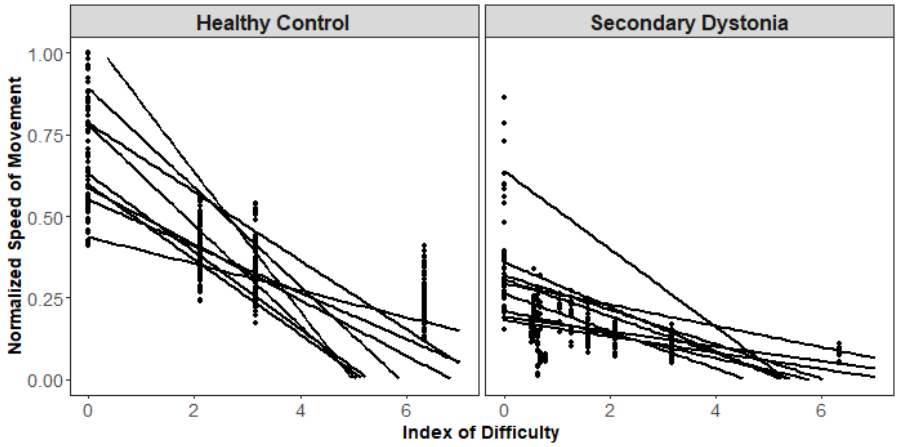

Figure 7.2: Normalized speed of movement versus the index of difficulty (IoD) (higher IoDindicates the more difficult task and zero IoD indicates the no-marble condition) for the healthy control and dystonia group is shown in dots. Each dot represents the speed for one repetition of task with the corresponding IoD, before the training (day 1). Regression lines for the speed of movement vs. the IoDfor each subject ($p - value < 0.01$ for all except two children with dystonia) are shown for both groups.The decreasing trend of movement with respect to the IoDindicates that all the subjects follow Fitts'law and adjust their speed based on the task difficulty.

7.4 Results

We fitted a linear mixed effect model to assess the effect of task difficulty on MT and speed of movement (Figure 7.1 a). The marble trajectory and the fitted ellipse for a patient with dystonia and a healthy subject is shown in Figure 7.1 b. This figure illustrates how they adjust the trajectory with respect to the movement time and index of difficulty. As illustrated in Figure 7.2 and consonant with earlier results on this task [141], the movement speed decreases in all subjects with the increase in task difficulty. Task difficulty is not a limiting factor for the speed of movement as the movement speeds without the marble (IoD= 0 in Figure 7.2) are faster than the other task difficulties. Within group comparison of movement speed showed that the subjects with dystonia ($R^2{}_{IoD} = 0.88, p - value < 0.001$) had a significant increase in their speed of movement in all three spoons with practice (day 1 vs. day 5, Figure 7.3). There was no significant change in the speed of movement of healthy

children with the easier spoon, however, the model predicted an increase in speed with practice in higher task difficulties (medium and difficult) $[({R^2}_{spoon} = 0.88,\ p - value_{easy} = 0.48,\ p - value_{medium} = 0.02,\ p - value_{difficult} = 0.04), ({R^2}_{IoD} = 0.77,\ p - value < 0.05)]$. Figure 7.3 shows the average speed and the standard deviation on day 1 versus day 5 for the healthy children and those with acquired dystonia in all three task difficulties. Similar results were obtained by performing ANOVA using type II Wald χ^2 test for dystonia group $[Pr(> \chi^2) < 0.01]$ and for the healthy group $[Pr(> \chi^2) < 0.01]$, showing the significant effect of the index of difficulty and the testing day on the speed of movement. The regression lines of the movement time versus the index of difficulty for day 1 and day 5 is shown for in each group in Figure 7.6 (only three subjects are shown for clarity). All the regression lines except two patients with acquired dystonia had a slope significantly different from zero $(p - value < 0.05)$, meaning the MT changed significantly with the difficulty (they followed the Fitts'law of speed-accuracy trade-off). The pairwise comparison to estimate the marginal means for the fitted model on the movement time revealed a significant improvement in the index of performance (inverse of the slopes) in healthy group $({R^2}_{IoD} = 0.73,\ p - value < 0.01)$ and the dystonia group $({R^2}_{IoD} = 0.89,\ p - value < 0.01)$ with practice (Figure 6). Analysis of variance (ANOVA) using type II Wald chi-square test performed on the linear models revealed a significant effect $[Pr(> \chi^2) < 0.01]$ of testing day and IoDbut not their interaction (testing day IoD).Based on the protocol, the spoon sizes that each subject practiced with are consistent throughout the whole experiment from day 1 to day 5; therefore, changes in IP are entirely due to changes in the speed of movement. Movement speed improved significantly for each of the spoon sizes individually in the children with dystonia, but the change in speed for the healthy children was only significant when combining performance across multiple spoon sizes.

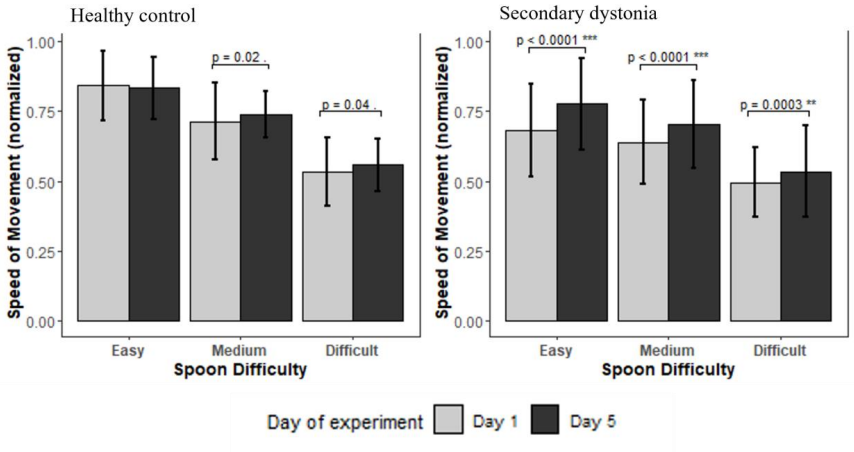

Figure 7.3: Statistical result of the improvement in the speed of movement in each group with three different task difficulties. The figure depicts the averaged normalized speed of movement and the standard deviation versus the testing day for three spoon sizes in the healthy (left) and dystonia (right) groups, predicted by the linear mixed effect model.

7.4.1 Marble Kinematics Analysis

The safety margin in the direction of first eigenvector (e_1 safety margin):

The statistical tests performed on thee1safety margin reveal that there was a significant decrease of e1 safety margin with practice in the healthy control group. The linear model explains 76 percent of variance in the data ($R^2 = 0.76$)and the ANOVA test revealed that all the variables and their interactions except day movement speed have a significant effect on thee1safety margin [$Pr(> \chi^2) < 0.01$]. On the other hand, the effects of these parameters on the e_1 safety margin were shown to be negligible in children with dystonia. The fitted linear mixed effect model ($R^2 = 0.57$) and the performed ANOVA test showed that there is no significant change in e_1 safety margin with practice and with the change of movement speed or IoD, in children with dystonia. These results are illustrated in Figure 7 with respect to spoon difficulty for each group. Figure 8 shows the regression lines for three subjects in each group with respect to IoDand speed of movement, respectively.

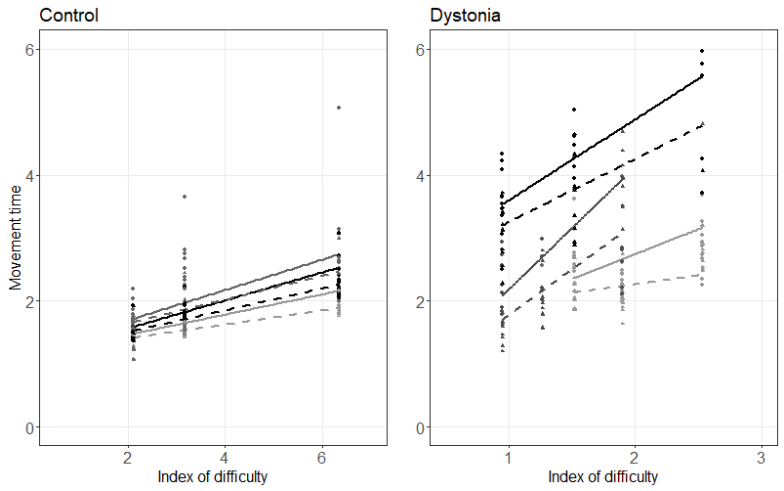

Figure 7.4: Change in movement time (MT) for three participants in each group (healthy control and dystonia) with respect to the index of difficulty (IoD) for day 1 (solid line) and day 5 (dashed line). Please note that the IoD axis scale is different for healthy children and children with dystonia due to their different capabilities. The slope of each line indicates the inverse of the index of performance for the corresponding subject on either day 1 (solid line) or day 5 (dashed line).

The safety margin in the direction of second eigenvector (e_2 safety margin):

We fitted linear mixed effect models and performed pairwise comparisons on them for the healthy control group ($R^2 = 0.49,\ p-value = 0.50$) and the dystonia group ($R^2 = 0.77,\ p-value = 0.43$). The analysis of variance showed only a significant effect of IoDspeed [$Pr(>\chi^2) < 0.01$] for the healthy control group (Figure 9). No other significant effects were observed on e_2 safety margin as illustrated in Figure 9.

Smoothness and Coefficient of Variation Analysis

Smoothness and Coefficient of Variation Analysis We performed the same analysis on the jerk scores in both groups. The models explained 79 percent and 53 percent or variance of jerk scores in healthy control and the dystonia group, respectively. The analysis of variance

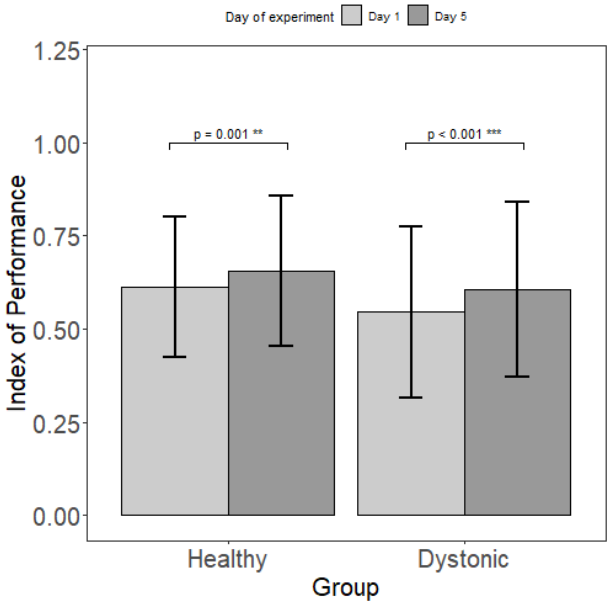

Figure 7.5: Statistical result of the normalized index of performance (IP) comparison before and after training in each group. An increase in the IP measures the effect of practice on learning.

showed a significant decrease of jerkiness (increased smoothness) with practice in children with dystonia $[Pr(> \chi^2) < .01]$ for the easy task difficulty (7.9a). The result is consistent with the pairwise comparison of means that revealed a significant decrease of jerkiness with practice ($p - value = 0.01$) in children with acquired dystonia with the easy task (day 1 mean = 0.4; day 5 mean = 0.14). A similar analysis was done on the coefficient of variation of movement in both groups. The models explained 30% and 51% or variance of CV in healthy control and the dystonia group, respectively. The pairwise comparison of mean in group analysis showed there is only a significant change of CV in difficult task (highest IoD) in children with dystonia ($p - value = 0.003$), however this slope is only significant ($Pvalue < 0.05$) for six participants of 13 as shown in Figure 10B (day 1 mean= 56.5, day 5 mean = 53).

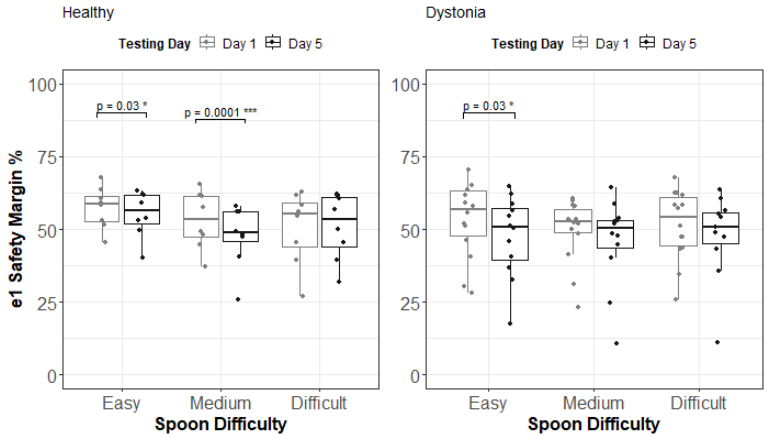

Figure 7.6: e_1 safety margin group analysis for healthy control group and dystonia group. This ratio does not change with respect to the index of difficulty; however, pairwise comparison revealed that the healthy control group showed a significant decrease in this ratio with practice, performing with easy and medium spoon difficulty; and this ratio only decreased in children with dystonia performing with easy spoon difficulty.

7.5 Discussion

In this study, we found that children with acquired dystonia and healthy children were able to improve their performance with practice on a trajectory task constrained only by the risk of dropping the marble. This constraint imposes a limitation on the maximum variability during the task performance, without specifying a particular desired trajectory or endpoint accuracy. It may therefore more closely reflect some aspects of normal movement behavior when tracking or tracing is not the purpose. For example, it may represent some of the challenges faced by children as they attempt to feed themselves with a spoon. Improvement in performance is reflected in the improvement in the speed-accuracy trade-off, as measured by increased speed for each level of difficulty, as well as IP. To increase speed without dropping the marble, it is necessary to reduce the movement variability within each trajectory or to decrease the maximum acceleration and jerk of the spoon that would lead to the marble exceeding the bounds of the spoon edge. We found that smoothness (evaluated by jerk-score)

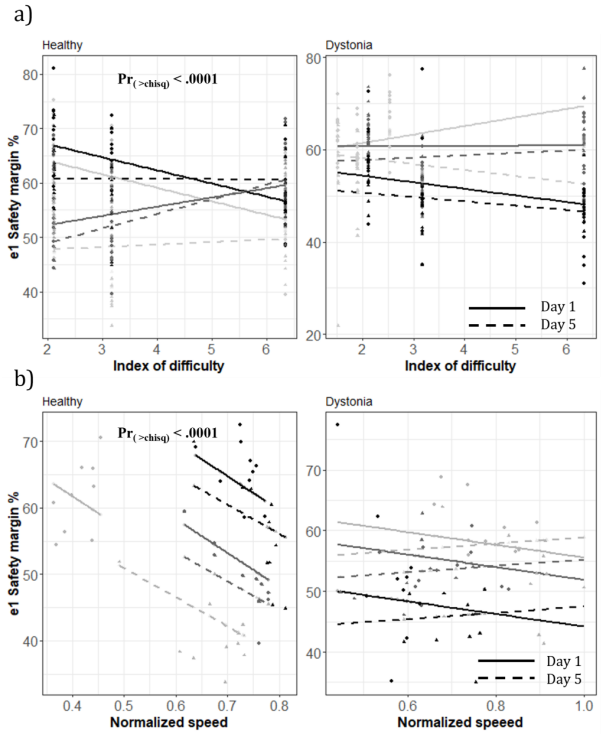

Figure 7.7: Fitted linear model. A: this figure shows the fitted lines for three subjects (three shades of gray) from each group with respect to index of difficulty (IoD). The fitted lines are consistent with earlier data shown in Figure 7.6; we see a higher decrease in this ratio in smaller indices of difficulty in the healthy control group [$Pr(> \chi^2) < 0.01$]. B: this figure shows the same fitted lines for those subjects with respect to the speed of movement. It clearly shows that the slopes are significant [$Pr(> \chi^2) < 0.01$] for the healthy control group, as well as the extent of the drop in this ratio.

in the lowest task difficulty and speed coefficient of variation in the highest task difficulty improved significantly in children with dystonia but not in healthy children. Although we would have expected a decrease in healthy children, in fact, some of their improvement in performance may have occurred due to a decrease in their initial large e_1 safety margin. In other words, healthy children tended to maintain the marble closer to the center of the spoon, thus perhaps not achieving the maximum speed that could be achieved; therefore, with practice, greater confidence in performance may have allowed them to reduce the safety margin and allow higher levels of variability without exceeding the bounds of the spoon. In contrast, children with dystonia had much less of a safety margin at baseline to begin with,

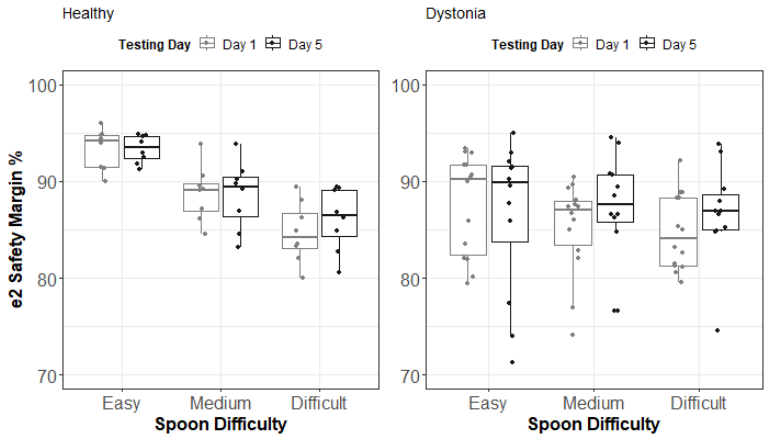

Figure 7.8: e_2 safety margin group analysis for the healthy control group and dystonia group. There was no change in this measure associated with the practice; however, in the healthy control group there is a significant decay of this measure with respect to spoon difficulty, consistent with the results of ANOVA on the effect of index of difficulty (IoD) * speed of movement $[Pr(> \chi^2) < 0.01]$; The e_2 safety margin decreases as the IoDincreases in the healthy control group.

perhaps due to their higher intrinsic variability. The only way that children with dystonia could thus improve performance would be to improve the smoothness and movement variability itself (reflected in either speed coefficient of variation and e_2 safety margin) because thee1safety margin could not be safely reduced without dropping the marble.In conclusion, we have shown that both healthy children and children with acquired dystonia improve skill as measured by the speed-accuracy trade-off on a trajectory task where variability is constrained by the physics of the task rather than adherence to a target trajectory. Although improvement of performance with practice is not surprising in healthy children, it is nevertheless interesting to note that this is reflected in a change in the speed-accuracy trade-off, indicating that Fitts'law is not immutable but rather represents the current level of skill and task performance [63, 40, 119]. Improvement of performance in children with acquired dystonia is interesting because this suggests that the higher level of signal-dependent noise can be controlled through repetition and learned strategies, and this provides an avenue for

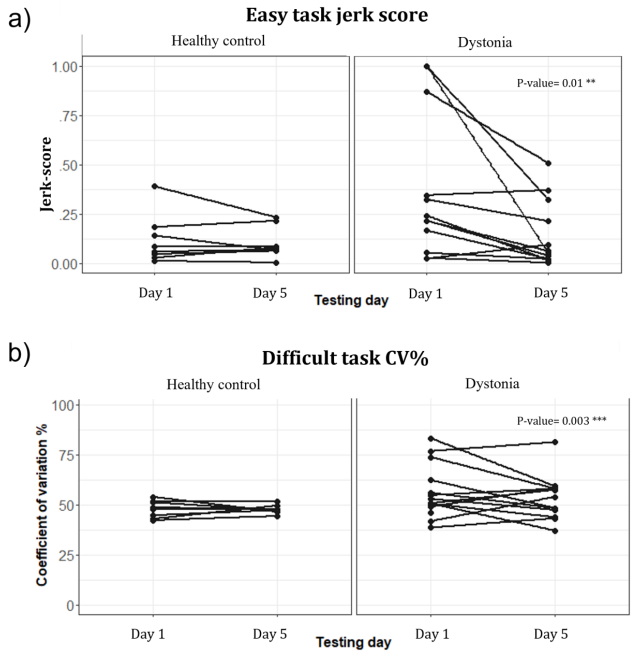

Figure 7.9: a) practicing decreased the lowest task difficulty jerk score in the dystonia group ($p - value = 0.01$) but the jerk score did not change significantly with practice in healthy children. b) practicing decreased the highest task difficulty coefficient of variation (CV) in the dystonia group ($p - value = 0.03$) but the variability did not change significantly with practice in healthy children.

the quantitative evaluation of rehabilitation strategies in this otherwise highly challenging group [49, 87, 210, 231].The significant increase in the index of performance arises from different approaches in the two different subject groups. Healthy children improved by reducing the safety margin, and perhaps maintaining the same level of signal-dependent noise, whereas the children with dystonia maintained the same safety margin but reduced their noise and movement variability. Children with dystonia appropriately adjust their speed to compensate for the level of variability, consistent with prior results [40]. Prior research has shown that the origins of signal-dependent noise may be different in these two groups, and perhaps only the noise in the children with dystonia is amenable to reduction with practice [40, 210]. Further study of modifications of the speed-accuracy trade-off in this and other tasks are warranted to evaluate the potential for improvement in skill with practice

in children with acquired dystonia.The limitations of this work include the random choice of task difficulties for each subject, however we confirmed that this variable did not have a significant effect on the final results by comparing the outcome variables with respect to both spoon number (task difficulties; easy, medium, and difficult) and IoD. In addition, due to the different capabilities of participants, we observed a ceiling effect in the speed of movement in some subjects, however, this was only limited to some repetitions, and the effect was canceled out by fitting linear models.

Bibliography

[1] Chapter 7 - new image contrasts from diffusion tensor imaging: Theory, meaning, and usefulness of dti-based image contrast. In S. Mori and J.-D. Tournier, editors, *Introduction to Diffusion Tensor Imaging (Second Edition)*, pages 53–64. Academic Press, San Diego, second edition edition, 2014.

[2] K. N. AAQ. Improving surgical outcome using diffusion tensor imaging techniques in deep brain stimulation. front surg. 2017; 4: 1–11, 2017.

[3] S. Abe, J. Vidmark, E. Hernandez-Martin, M. Kasiri, R. Sorouhmojdehi, S. A. S. Mousavi, and T. D. Sanger. Diffusion tractography predicts deep brain stimulation evoked potential amplitude and delay. *medRxiv*, 2024.

[4] E. L. Air, J. L. Ostrem, T. D. Sanger, and P. A. Starr. Deep brain stimulation in children: Experience and technical pearls. clinical article. *Journal of Neurosurgery: Pediatrics*, 8(6):566–574, 2011.

[5] A. Albanese, K. Bhatia, S. B. Bressman, M. R. Delong, S. Fahn, V. S. Fung, M. Hallett, J. Jankovic, H. A. Jinnah, C. Klein, A. E. Lang, J. W. Mink, and J. K. Teller. Phenomenology and classification of dystonia: A consensus update, 6 2013.

[6] R. L. Albin, A. B. Young, and J. B. Penney. The functional anatomy of basal ganglia disorders, 1989.

[7] T. R. Anderson, B. Hu, K. Iremonger, and Z. H. Kiss. Selective attenuation of afferent synaptic transmission as a mechanism of thalamic deep brain stimulation-induced tremor arrest. *Journal of Neuroscience*, 26(3):841–850, 2006.

[8] J. Anthofer, K. Steib, C. Fellner, M. Lange, A. Brawanski, and J. Schlaier. The variability of atlas-based targets in relation to surrounding major fibre tracts in thalamic deep brain stimulation. *Acta neurochirurgica*, 156:1497–1504, 2014.

[9] J. M. Anthofer, K. Steib, C. Fellner, M. Lange, A. Brawanski, and J. Schlaier. Dti-based deterministic fibre tracking of the medial forebrain bundle. *Acta neurochirurgica*, 157:469–477, 2015.

[10] G. AP. Relations between parameters of step-tracking movements and single cell discharge in the globus pallidus and subthalamic nucleus of the behaving monkey. *J Neurosci*, 3:1586–1598, 1983.

[11] M. Åström, E. Diczfalusy, H. Martens, and K. Wårdell. Relationship between neural activation and electric field distribution during deep brain stimulation. *IEEE Transactions on Biomedical Engineering*, 62(2):664–672, 2014.

[12] P. Babaeeghazvini, L. M. Rueda-Delgado, J. Gooijers, S. P. Swinnen, and A. Daffertshofer. Brain structural and functional connectivity: A review of combined works of diffusion magnetic resonance imaging and electro-encephalography. *Frontiers in Human Neuroscience*, 15:721206, 2021.

[13] T. Bao, W. J. Carender, C. Kinnaird, V. J. Barone, G. Peethambaran, S. L. Whitney, M. Kabeto, R. D. Seidler, and K. H. Sienko. Effects of long-term balance training with vibrotactile sensory augmentation among community-dwelling healthy older adults: A randomized preliminary study. *Journal of NeuroEngineering and Rehabilitation*, 15, 1 2018.

[14] T. Bao, B. N. Klatt, W. J. Carender, C. Kinnaird, S. Alsubaie, S. L. Whitney, and K. H. Sienko. Effects of long-term vestibular rehabilitation therapy with vibrotactile sensory augmentation for people with unilateral vestibular disorders-a randomized preliminary study. *Journal of Vestibular Research: Equilibrium and Orientation*, 29:323–334, 2020.

[15] I. Bar-Gad, S. Elias, E. Vaadia, and H. Bergman. Complex locking rather than complete cessation of neuronal activity in the globus pallidus of a 1-methyl-4-phenyl-1, 2, 3, 6-tetrahydropyridine-treated primate in response to pallidal microstimulation. *Journal of Neuroscience*, 24(33):7410–7419, 2004.

[16] D. Bates, M. Mächler, B. M. Bolker, and S. C. Walker. Fitting linear mixed-effects models using lme4. *Journal of Statistical Software*, 67:1–48, 10 2015.

[17] E. E. Benarroch. Effects of acetylcholine in the striatum. *Neurology*, 79(3):274–281, 2012.

[18] M. Bertucco, N. H. Bhanpuri, and T. D. Sanger. Perceived cost and intrinsic motor variability modulate the speed-accuracy trade-off. *PLoS ONE*, 10, 10 2015.

[19] K. D. Bhatia, L. Henderson, G. Ramsey-Stewart, and J. May. Diffusion tensor imaging to aid subgenual cingulum target selection for deep brain stimulation in depression. *Stereotactic and functional neurosurgery*, 90(4):225–232, 2012.

[20] J. J. Binney, N. J. Dowrick, A. J. Fisher, and M. E. Newman. *The theory of critical phenomena: an introduction to the renormalization group*. Oxford University Press, 1992.

[21] BioRender. Created with biorender.com. `https://www.biorender.com`, 2024. Accessed: [Insert date of access].

[22] A. W. Bowman and A. Azzalini. Applied smoothing techniques for data analysis, 1997.

[23] X. O. Breakefield, A. J. Blood, Y. Li, M. Hallett, P. I. Hanson, and D. G. Standaert. The pathophysiological basis of dystonias. *Nature Reviews Neuroscience*, 9:222–234, 2008.

[24] N. Brüggemann. Contemporary functional neuroanatomy and pathophysiology of dystonia. *Journal of Neural Transmission*, 128(4):499–508, 2021.

[25] B. Burle, L. Spieser, C. Roger, L. Casini, T. Hasbroucq, and F. Vidal. Spatial and temporal resolutions of eeg: Is it really black and white? a scalp current density view. *International Journal of Psychophysiology*, 97(3):210–220, 2015.

[26] C. R. Butson, S. E. Cooper, J. M. Henderson, and C. C. McIntyre. Predicting the effects of deep brain stimulation with diffusion tensor based electric field models. In *Medical Image Computing and Computer-Assisted Intervention–MICCAI 2006: 9th International Conference, Copenhagen, Denmark, October 1-6, 2006. Proceedings, Part II 9*, pages 429–437. Springer, 2006.

[27] G. Caithness, R. Osu, P. Bays, H. Chase, J. Klassen, M. Kawato, D. M. Wolpert, and J. R. Flanagan. Failure to consolidate the consolidation theory of learning for sensorimotor adaptation tasks. *Journal of Neuroscience*, 24:8662–8671, 10 2004.

[28] V. D. Calhoun and T. Adali. Time-varying brain connectivity in fmri data: whole-brain data-driven approaches for capturing and characterizing dynamic states. *IEEE Signal Processing Magazine*, 33(3):52–66, 2016.

[29] G. L. Camera. The mean field approach for populations of spiking neurons. *Advances in experimental medicine and biology*, 1359:125–157, 2021.

[30] C. Cao, Y. Pan, D. Li, S. Zhan, J. Zhang, and B. Sun. Subthalamus deep brain stimulation for primary dystonia patients: A long-term follow-up study. *Movement Disorders*, 28(13):1877–1882, 2013.

[31] S. J. Carr, A. Gershon, N. Shafiabadi, S. D. Lhatoo, C. Tatsuoka, and S. S. Sahoo. An integrative approach to study structural and functional network connectivity in epilepsy using imaging and signal data. *Frontiers in integrative neuroscience*, 14:491403, 2021.

[32] C. Casellato, E. Ambrosini, A. Galbiati, E. Biffi, A. Cesareo, E. Beretta, F. Lunardini, G. Zorzi, T. D. Sanger, and A. Pedrocchi. Emg-based vibro-tactile biofeedback training: Effective learning accelerator for children and adolescents with dystonia? a pilot crossover trial. *Journal of NeuroEngineering and Rehabilitation*, 16, 11 2019.

[33] R. S. Causby, M. N. McDonnell, L. Reed, and S. L. Hillier. A randomised controlled trial of sensory awareness training and additional motor practice for learning scalpel skills in podiatry students. *BMC Medical Education*, 16, 12 2016.

[34] L. Centen, D. Oterdoom, M. Tijssen, I. Lesman-Leegte, M. van Egmond, and J. van Dijk. Bilateral pallidotomy for dystonia: A systematic review. *Movement Disorders*, 36(3):547–557, Mar 2021.

[35] C.-T. Chen. *Linear System Theory and Design*. Oxford University Press, Inc., 3rd edition, 1998.

[36] T. Cheung, A. M. Noecker, R. L. Alterman, C. C. McIntyre, and M. Tagliati. Defining a therapeutic target for pallidal deep brain stimulation for dystonia. *Annals of Neurology*, 76(1):22–30, 2014.

[37] S. Chiken and A. Nambu. High-frequency pallidal stimulation disrupts information flow through the pallidum by gabaergic inhibition. *Journal of Neuroscience*, 33(6):2268–2280, Feb. 2013. PMID: 23392658; PMCID: PMC6619164.

[38] S. Chiken and A. Nambu. Disrupting neuronal transmission: Mechanism of dbs?, 2014.

[39] S. Chiken and A. Nambu. Mechanism of deep brain stimulation: Inhibition, excitation, or disruption? *The Neuroscientist*, 22(3):313–322, 2016. Epub 2015 Apr 17. PMID: 25888630; PMCID: PMC4871171.

[40] V. W. T. Chu, D. Sternad, and T. D. Sanger. Healthy and dystonic children compensate for changes in motor variability. *Journal of Neurophysiology*, 109:2169–2178, 2013.

[41] L. Cif, V. Gonzalez-Martinez, X. Vasques, A. Corlobé, A. M. Moura, A. Bonafé, and P. E. Coubes. Staged implantation of multiple electrodes in the internal globus pallidus in the treatment of primary generalized dystonia: Clinical article. *Journal of Neurosurgery*, 116(5):1144 – 1152, 2012. Cited by: 33.

[42] W. S. Cleveland. Robust locally weighted regression and smoothing scatterplots. *Journal of the American Statistical Association*, 74(368):829–836, 12 1979. doi: 10.1080/01621459.1979.10481038.

[43] V. Coenen, C. Jenkner, C. Honey, and B. Mädler. Electrophysiologic validation of diffusion tensor imaging tractography during deep brain stimulation surgery. *American Journal of Neuroradiology*, 37(8):1470–1478, 2016.

[44] V. A. Coenen, N. Allert, and B. Mädler. A role of diffusion tensor imaging fiber tracking in deep brain stimulation surgery: Dbs of the dentato-rubro-thalamic tract (drt) for the treatment of therapy-refractory tremor. *Acta neurochirurgica*, 153:1579–1585, 2011.

[45] V. A. Coenen, N. Allert, S. Paus, M. Kronenbürger, H. Urbach, and B. Mädler. Modulation of the cerebello-thalamo-cortical network in thalamic deep brain stimulation for tremor: a diffusion tensor imaging study. *Neurosurgery*, 75(6):657–670, 2014.

[46] V. A. Coenen, B. Mädler, H. Schiffbauer, H. Urbach, and N. Allert. Individual fiber anatomy of the subthalamic region revealed with diffusion tensor imaging: a concept to identify the deep brain stimulation target for tremor suppression. *Neurosurgery*, 68(4):1069–1076, 2011.

[47] V. A. Coenen and M. Reisert. Dti for brain targeting: Diffusion weighted imaging fiber tractography—assisted deep brain stimulation. In *International Review of Neurobiology*, volume 159, pages 47–67. Elsevier, 2021.

[48] V. A. Coenen, B. Varkuti, Y. Parpaley, S. Skodda, T. Prokop, H. Urbach, M. Li, and P. C. Reinacher. Postoperative neuroimaging analysis of drt deep brain stimulation revision surgery for complicated essential tremor. *Acta Neurochirurgica*, 159:779–787, 2017.

[49] R. G. Cohen and D. Sternad. Variability in motor learning: relocating, channeling and reducing noise. *Experimental brain research*, 193:69–83, 2 2009.

[50] A. Conte, G. Defazio, M. Hallett, G. Fabbrini, and A. Berardelli. The role of sensory information in the pathophysiology of focal dystonias. *Nature Reviews Neurology*, 15(4):224–233, Apr 2019.

[51] S. Correia, S. Y. Lee, T. Voorn, D. F. Tate, R. H. Paul, S. Zhang, S. P. Salloway, P. F. Malloy, and D. H. Laidlaw. Quantitative tractography metrics of white matter integrity in diffusion-tensor mri. *NeuroImage*, 42(2):568–581, 2008.

[52] P. Coubes, B. Echenne, A. Roubertie, N. Vayssière, S. Tuffery, V. Humbertclaude, G. Cambonie, M. Claustres, and P. Frerebeau. Treatment of early-onset generalized dystonia by bilateral chronic electrical stimulation of the internal globus pallidus. case report. *Neurochirurgie*, 45(2):139 – 144, 1999. Cited by: 126.

[53] P. Coubes, A. Roubertie, N. Vayssiere, S. Hemm, and B. Echenne. Treatment of dyt1-generalised dystonia by stimulation of the internal globus pallidus. *The Lancet*, 355(9222):2220–2221, 2000.

[54] J. Daunizeau, K. E. Stephan, and K. J. Friston. Stochastic dynamic causal modelling of fmri data: Should we care about neural noise? *NeuroImage*, 62:464–481, 2012.

[55] S. Delaloye and P. Holtzheimer. Deep brain stimulation in the treatment of depression. *Dialogues Clin Neurosci*, 16(1):83–91, 2014.

[56] M. R. DeLong. Primate models of movement disorders of basal ganglia origin. *Trends in neurosciences*, 13(7):281–285, 1990.

[57] J.-M. Deniau, B. Degos, C. Bosch, and N. Maurice. Deep brain stimulation mechanisms: beyond the concept of local functional inhibition. *European Journal of Neuroscience*, 32(7):1080–1091, 2010.

[58] J. L. Devito and M. E. Anderson. An autoradiographic study of efferent connections of the globus pallidus in macaca mulatta*, 1982.

[59] J. O. Dostrovsky and A. M. Lozano. Mechanisms of deep brain stimulation. *Movement disorders: official journal of the Movement Disorder Society*, 17(S3):S63–S68, 2002.

[60] Y. Erez, H. Czitron, K. McCairn, K. Belelovsky, and I. Bar-Gad. Short-term depression of synaptic transmission during stimulation in the globus pallidus of 1-methyl-4-phenyl-1, 2, 3, 6-tetrahydropyridine-treated primates. *Journal of neuroscience*, 29(24):7797–7802, 2009.

[61] S. Ewert, P. Plettig, N. Li, M. M. Chakravarty, D. L. Collins, T. M. Herrington, A. A. Kühn, and A. Horn. Toward defining deep brain stimulation targets in mni space: a subcortical atlas based on multimodal mri, histology and structural connectivity. *Neuroimage*, 170:271–282, 2018.

[62] B. Fischl. Freesurfer. *Neuroimage*, 62(2):774–781, 2012.

[63] P. M. Fitts. the information capacity of the human motor system in controlling the amplitude of movement. *Journal of Experimental Psychology*, 47:381–391, 1954.

[64] E. T. Fonoff, W. K. Campos, M. Mandel, E. J. L. Alho, and M. J. Teixeira. Bilateral subthalamic nucleus stimulation for generalized dystonia after bilateral pallidotomy. *Movement Disorders*, 27(12):1559–1563, 2012.

[65] R. Frackowiak, K. Friston, C. Frith, R. Dolan, and J. Mazziotta, editors. *Human Brain Function*. Academic Press USA, 1997.

[66] D. Franz, A. Richter, and R. Köhling. Electrophysiological insights into deep brain stimulation of the network disorder dystonia. *Pflugers Arch*, 475(10):1133–1147, Oct 2023.

[67] K. Friston, J. Kilner, and L. Harrison. A free energy principle for the brain. *Journal of Physiology Paris*, 100:70–87, 7 2006.

[68] K. Friston, J. Mattout, N. Trujillo-Barreto, J. Ashburner, and W. Penny. Variational free energy and the laplace approximation. *NeuroImage*, 34:220–234, 1 2007.

[69] K. Friston and W. Penny. Post hoc bayesian model selection. *NeuroImage*, 56:2089–2099, 6 2011.

[70] K. J. Friston, L. Harrison, and W. Penny. Dynamic causal modelling. *NeuroImage*, 19:1273–1302, 8 2003.

[71] K. Fujita and D. Eidelberg. Imbalance of the direct and indirect pathways in focal dystonia: A balanced view. *Brain*, 140:3075–3077, 12 2017.

[72] W. K. Fung and K. J. Peall. What is the role of the cerebellum in the pathophysiology of dystonia? *Journal of Neurology*, 266:1549–1551, 6 2019.

[73] R. Gelineau-Morel, M. C. Kruer, J. F. Garris, A. Abu Libdeh, D. A. N. Barbosa, K. A. Coffman, D. Moon, C. Barton, A. Zea Vera, A. B. Bruce, T. Larsh, S. W. Wu, D. L. Gilbert, and J. A. O'Malley. Deep brain stimulation for pediatric dystonia: A review of the literature and suggested programming algorithm. *J Child Neurol*, 37(10-11):813–824, Oct. 2022. Epub 2022 Sep 2.

[74] X. Geng, J. Zhang, Y. Jiang, K. Ashkan, T. Foltynie, P. Limousin, L. Zrinzo, A. Green, T. Aziz, P. Brown, and S. Wang. Comparison of oscillatory activity in subthalamic nucleus in parkinson's disease and dystonia. *Neurobiology of Disease*, 98:100–107, 2017.

[75] E. Gleichgerrcht, A. S. Greenblatt, T. S. Kellermann, N. Rowland, W. A. Vandergrift, J. Edwards, K. A. Davis, and L. Bonilha. Patterns of seizure spread in temporal lobe epilepsy are associated with distinct white matter tracts. *Epilepsy research*, 171:106571, 2021.

[76] G. H. Glover. Overview of functional magnetic resonance imaging. *Neurosurgery Clinics*, 22(2):133–139, 2011.

[77] J. Goñi, M. P. Van Den Heuvel, A. Avena-Koenigsberger, N. Velez de Mendizabal, R. F. Betzel, A. Griffa, P. Hagmann, B. Corominas-Murtra, J.-P. Thiran, and O. Sporns. Resting-brain functional connectivity predicted by analytic measures of network communication. *Proceedings of the National Academy of Sciences*, 111(2):833–838, 2014.

[78] R. A. González, P. E. Valenzuela, C. R. Rojas, and R. A. Rojas. Optimal enforcement of causality in non-parametric transfer function estimation. *IEEE Control Systems Letters*, 1(2):268–273, 2017.

[79] D. Graham, S. Paget, and N. Wimalasundera. Current thinking in the health care management of children with cerebral palsy. *Medical Journal of Australia*, 210(3):129–135, Feb 2019.

[80] M. D. Greicius, K. Supekar, V. Menon, and R. F. Dougherty. Resting-state functional connectivity reflects structural connectivity in the default mode network. *Cerebral cortex*, 19(1):72–78, 2009.

[81] W. M. Grill, M. B. Cantrell, and M. S. Robertson. Antidromic propagation of action potentials in branched axons: implications for the mechanisms of action of deep brain stimulation. *Journal of computational neuroscience*, 24:81–93, 2008.

[82] W. M. Grill and C. C. Mclntyre. Extracellular excitation of central neurons: implications for the mechanisms of deep brain stimulation. *Thalamus & Related Systems*, 1(3):269–277, 2001.

[83] W. M. Grill, A. N. Snyder, and S. Miocinovic. Deep brain stimulation creates an informational lesion of the stimulated nucleus. *Neuroreport*, 15(7):1137–1140, 2004.

[84] I. Hamada and M. R. DeLong. Excitotoxic acid lesions of the primate subthalamic nucleus result in transient dyskinesias of the contralateral limbs. *Journal of Neurophysiology*, 68(5):1850–1858, 1992. PMID: 1479448.

[85] N. Hammoud and J. Jankovic. Botulinum toxin in the treatment of cervical dystonia: Evidence-based review. *Dystonia*, 1, 2022.

[86] M. Hariz. Pallidotomy for dystonia: A neglected procedure? *Movement Disorders*, 36(3):533–534, Mar 2021.

[87] C. M. Harris and D. M. Wolpert. Signal-dependent noise determines motor planning. *Nature*, 394:780–784, 8 1998.

[88] T. Hashimoto, C. M. Elder, M. S. Okun, S. K. Patrick, and J. L. Vitek. Stimulation of the subthalamic nucleus changes the firing pattern of pallidal neurons. *Journal of neuroscience*, 23(5):1916–1923, 2003.

[89] J. M. Henderson. "connectomic surgery": diffusion tensor imaging (dti) tractography as a targeting modality for surgical modulation of neural networks. *Frontiers in integrative neuroscience*, 6:15, 2012.

[90] E. Hernandez-Martin, E. Arguelles, R. Deshpande, and T. D. Sanger. Evoked potentials during peripheral stimulation confirm electrode location in thalamic subnuclei in children with secondary dystonia. *Journal of Child Neurology*, 35:799–807, 2020. PMID: 32567481.

[91] E. Hernandez-Martin, E. Arguelles, M. Liker, A. Robison, and T. D. Sanger. Increased movement-related signals in both basal ganglia and cerebellar output pathways in two children with dystonia. *Frontiers in Neurology*, 13, 2022.

[92] E. Hernandez-Martin, M. Kasiri, S. Abe, J. MacLean, J. Olaya, M. Liker, J. Chu, and T. D. Sanger. Globus pallidus internus activity increases during voluntary movement in children with dystonia. *iScience*, 26, 6 2023.

[93] A. L. Hodgkin and A. F. Huxley. Currents carried by sodium and potassium ions through the membrane of the giant axon of loligo. *The Journal of Physiology*, 116(4):449–472, 1952.

[94] A. L. Hodgkin and A. F. Huxley. A quantitative description of membrane current and its application to conduction and excitation in nerve. *The Journal of Physiology*, 117(4):500–544, 1952.

[95] N. Hogan and D. Sternad. Sensitivity of smoothness measures to movement duration, amplitude, and arrests. *Journal of motor behavior*, 41:529–534, 11 2009.

[96] P. Hok, T. Veverka, P. Hluštík, M. Nevrlý, and P. Kaňovský. The central effects of botulinum toxin in dystonia and spasticity. *Toxins (Basel)*, 13(2):155, 2021.

[97] H. Huang and M. Ding. Linking functional connectivity and structural connectivity quantitatively: a comparison of methods. *Brain connectivity*, 6(2):99–108, 2016.

[98] A. Husch, M. V. Petersen, P. Gemmar, J. Goncalves, and F. Hertel. Pacer-a fully automated method for electrode trajectory and contact reconstruction in deep brain stimulation. *NeuroImage: Clinical*, 17:80–89, 2018.

[99] Y. P. Ivanenko, R. Grasso, and F. Lacquaniti. Influence of leg muscle vibration on human walking, 2000.

[100] R. Jech, D. Urgošík, J. Tintěra, A. Nebuželskỳ, J. Krásenskỳ, R. Liščák, J. Roth, and E. Ržička. Functional magnetic resonance imaging during deep brain stimulation: a pilot study in four patients with parkinson's disease. *Movement disorders: official journal of the Movement Disorder Society*, 16(6):1126–1132, 2001.

[101] M. Jenkinson, C. F. Beckmann, T. E. Behrens, M. W. Woolrich, and S. M. Smith. Fsl. *Neuroimage*, 62(2):782–790, 2012.

[102] H. A. Jinnah and S. A. Factor. Diagnosis and treatment of dystonia, 2015.

[103] K. A. Johnson, J. N. Cagle, J. L. Lopes, J. K. Wong, M. S. Okun, A. Gunduz, A. W. Shukla, J. D. Hilliard, K. D. Foote, and C. de Hemptinne. Globus pallidus internus deep brain stimulation evokes resonant neural activity in Parkinson's disease. *Brain Communications*, 5(2):fcad025, 02 2023.

[104] D. K. Jones. Challenges and limitations of quantifying brain connectivity in vivo with diffusion mri. *Imaging in Medicine*, 2:341–355, 2010.

[105] D. K. Jones, T. R. Knösche, and R. Turner. White matter integrity, fiber count, and other fallacies: The do's and don'ts of diffusion mri. *NeuroImage*, 73:239–254, 2013.

[106] M. JW. Basal ganglia motor control. ii. late pallidal timing relative to movement onset and inconsistent pallidal coding of movement parameters. *J Neurophysiol*, 65:301–329, 1991.

[107] J. F. Kaiser. On a simple algorithm to calculate the'energy'of a signal. In *International conference on acoustics, speech, and signal processing*, pages 381–384. IEEE, 1990.

[108] G. Kamali, R. J. Smith, M. Hays, C. Coogan, N. E. Crone, J. Y. Kang, and S. V. Sarma. Transfer function models for the localization of seizure onset zone from cortico-cortical evoked potentials. *Frontiers in Neurology*, 11, 2020.

[109] G. Kamali, R. J. Smith, M. Hays, C. Coogan, N. E. Crone, J. Y. Kang, and S. V. Sarma. Transfer function models for the localization of seizure onset zone from cortico-cortical evoked potentials. *Frontiers in Neurology*, 11:579961, 2020.

[110] G. Kang and M. M. Lowery. Effects of antidromic and orthodromic activation of stn afferent axons during dbs in parkinson's disease: a simulation study. *Frontiers in computational neuroscience*, 8:32, 2014.

[111] S. Karimi, P. Cosman, C. Wald, and H. Martz. Segmentation of artifacts and anatomy in ct metal artifact reduction. *Medical physics*, 39(10):5857–5868, 2012.

[112] M. Kasiri, E. Biffi, E. Ambrosini, A. Pedrocchi, and T. D. Sanger. Improvement of speed-accuracy tradeoff during practice of a point-to-point task in children with acquired dystonia. *Journal of Neurophysiology*, 130(4):931–940, 2023. PMID: 37584081.

[113] M. Kasiri, J. W. Hillman, E. Hernandez-Martin, S. A. S. Mousavi, and T. D. Sanger. Endogenous signals during active movement predict deep brain stimulation evoked potential pathways: Results of a transfer function analysis. *medRxiv*, pages 2023–04, 2023.

[114] M. Kasiri, S. Javadzadeh, J. Nataraj, S. A. S. Mousavi, and T. Sanger. Correlated activity in globus pallidus and thalamus during voluntary reaching movement in three children with primary dystonia. *Dystonia*, 2:2023.05.11.23289830, 2 2023.

[115] J. R. Keen, A. Przekop, J. E. Olaya, A. Zouros, and F. P. K. Hsu. Deep brain stimulation for the treatment of childhood dystonic cerebral palsy clinical article. *Journal of Neurosurgery: Pediatrics*, 14(6):585 – 593, 2014. Cited by: 54.

[116] H. Khoo, J. Hall, F. Dubeau, N. Tani, S. Oshino, Y. Fujita, J. Gotman, and H. Kishima. Technical aspects of seeg and its interpretation in the delineation of the epileptogenic zone. *Neurological Surgery (Tokyo)*, 60(12):565–580, 2020. Epub 2020 Nov 6.

[117] A. Kibleur and O. David. Electroencephalographic read-outs of the modulation of cortical network activity by deep brain stimulation. *Bioelectronic Medicine*, 4(1):2, 2018. Accessed: date.

[118] S. J. Kiebel, M. I. Garrido, R. J. Moran, and K. J. Friston. Dynamic causal modelling for eeg and meg. *Cognitive Neurodynamics*, 2:121–136, 6 2008.

[119] T. Kitago, J. Liang, V. S. Huang, S. Hayes, P. Simon, L. Tenteromano, R. M. Lazar, R. S. Marshall, P. Mazzoni, L. Lennihan, and J. W. Krakauer. Improvement after constraint-induced movement therapy: Recovery of normal motor control or task-specific compensation? *Neurorehabilitation and Neural Repair*, 27:99–109, 7 2012. doi: 10.1177/1545968312452631.

[120] M. A. Koch, D. G. Norris, and M. Hund-Georgiadis. An investigation of functional and anatomical connectivity using magnetic resonance imaging. *Neuroimage*, 16(1):241–250, 2002.

[121] L. Kong, Q. He, Q. Li, R. Schreiber, K. I. Kaitin, and L. Shao. Rapid progress in neuroimaging technologies fuels central nervous system translational medicine. *Drug Discovery Today*, page 103485, 2023.

[122] A. Koy, J.-P. Lin, T. D. Sanger, W. A. Marks, J. W. Mink, and L. Timmermann. Advances in management of movement disorders in children. *The Lancet Neurology*, 15(7):719–735, 2016.

[123] J. L. Lanciego, N. Luquin, and J. A. Obeso. Functional neuroanatomy of the basal ganglia. *Cold Spring Harbor perspectives in medicine*, 2(12):a009621–a009621, 12 2012.

[124] E. W. Lang, A. M. Tomé, I. R. Keck, J. Górriz-Sáez, and C. G. Puntonet. Brain connectivity analysis: a short survey. *Computational intelligence and neuroscience*, 2012:8–8, 2012.

[125] C. M. Laymon, D. S. Minhas, C. R. Becker, C. Matan, M. J. Oborski, J. C. Price, and J. M. Mountz. Image-based 2d re-projection for attenuation substitution in pet neuroimaging. *Molecular Imaging and Biology*, 20:826–834, 2018.

[126] M. Le Bellac, F. Mortessagne, and G. G. Batrouni. *Equilibrium and non-equilibrium statistical thermodynamics*. Cambridge University Press, 2004.

[127] D. J. Lee, C. S. Lozano, R. F. Dallapiazza, and A. M. Lozano. Current and future directions of deep brain stimulation for neurological and psychiatric disorders: Jnspg 75th anniversary invited review article. *Journal of neurosurgery*, 131(2):333–342, 2019.

[128] K. Lehnertz, C. Geier, T. Rings, and K. Stahn. Capturing time-varying brain dynamics. *EPJ Nonlinear Biomedical Physics*, 5:2, 2017.

[129] L. Leistritz, K. Schiecke, L. Astolfi, and H. Witte. Time-variant modeling of brain processes. *Proceedings of the IEEE*, 104(2):262–281, 2015.

[130] F. A. Lenz, C. J. Jaeger, M. S. Seike, Y. C. Lin, S. G. Reich, M. R. Delong, J. L. Vitek, and M. R. DeLong. Thalamic single neuron activity in patients with dystonia: Dystonia-related activity and somatic sensory reorganization, 1999.

[131] R. Levy, P. Ashby, W. D. Hutchison, A. E. Lang, A. M. Lozano, and J. O. Dostrovsky. Dependence of subthalamic nucleus oscillations on movement and dopamine in Parkinson's disease. *Brain*, 125(6):1196–1209, 06 2002.

[132] M. Liker and T. Sanger. Pediatric deep brain stimulation in secondary dystonia using stereotactic depth electrode targeting. In *MOVEMENT DISORDERS*, volume 34, pages S534–S535. WILEY 111 RIVER ST, HOBOKEN 07030-5774, NJ USA, 2019.

[133] M. A. Liker, T. D. Sanger, J. A. MacLean, J. Nataraj, E. Arguelles, M. Krieger, A. Robison, and J. Olaya. Stereotactic awake basal ganglia electrophysiological recording and stimulation (sabers): A novel staged procedure for personalized targeting of deep brain stimulation in pediatric movement and neuropsychiatric disorders. *Journal of Child Neurology*, 0(0):08830738231224057, 0. PMID: 38409793.

[134] M. C. Litwińczuk, N. Muhlert, L. Cloutman, N. Trujillo-Barreto, and A. Woollams. Combination of structural and functional connectivity explains unique variation in specific domains of cognitive function. *NeuroImage*, 262:119531, 2022.

[135] H. Liu, G. Fan, K. Xu, and F. Wang. Changes in cerebellar functional connectivity and anatomical connectivity in schizophrenia: a combined resting-state functional mri and diffusion tensor imaging study. *Journal of magnetic resonance imaging*, 34(6):1430–1438, 2011.

[136] J. Liu, H. Ding, K. Xu, D. Wang, J. Ouyang, Z. Liu, and R. Liu. Micro lesion effect of pallidal deep-brain stimulation for meige syndrome. *Scientific Reports*, 12(1):19980, 2022.

[137] E. Lowet, K. Kondabolu, S. Zhou, R. A. Mount, Y. Wang, C. R. Ravasio, and X. Han. Deep brain stimulation creates informational lesion through membrane depolarization in mouse hippocampus. *Nature Communications*, 13(1):7709, 2022.

[138] B. Luber, S. W. Davis, Z.-D. Deng, D. Murphy, A. Martella, A. V. Peterchev, and S. H. Lisanby. Using diffusion tensor imaging to effectively target tms to deep brain structures. *NeuroImage*, 249:118863, 2022.

[139] M. S. Luciano, A. Robichaux-Viehoever, K. A. Dodenhoff, M. L. Gittings, A. C. Viser, C. A. Racine, I. O. Bledsoe, C. W. Pereira, S. S. Wang, P. A. Starr, and J. L. Ostrem. Thalamic deep brain stimulation for acquired dystonia in children and young adults: a phase 1 clinical trial. *Journal of Neurosurgery: Pediatrics*, 27(2):203–212, 2021.

[140] D. E. Lumsden, M. Kaminska, H. Gimeno, K. Tustin, L. Baker, S. Perides, K. Ashkan, R. Selway, and J.-P. Lin. Proportion of life lived with dystonia inversely correlates with response to pallidal deep brain stimulation in both primary and secondary childhood dystonia. *Developmental Medicine & Child Neurology*, 55(6):567–574, 2013.

[141] F. Lunardini, M. Bertucco, C. Casellato, N. Bhanpuri, A. Pedrocchi, and T. D. Sanger. Speed-accuracy trade-off in a trajectory-constrained self-feeding task: A quantitative index of unsuppressed motor noise in children with dystonia. *Journal of Child Neurology*, 30:1676–1685, 6 2015.

[142] F. Lunardini and [et al.]. Increased task-uncorrelated muscle activity in childhood dystonia. *Journal of Neuroengineering and Rehabilitation*, 12:52, 2015.

[143] K. Lyons and R. Pahwa. Deep brain stimulation and tremor. *Neurotherapeutics*, 5(2):331–338, 2008.

[144] I. S. MacKenzie. A note on the information-theoretic basis for fitts' law. *Journal of Motor Behavior*, 21:323–330, 9 1989. doi: 10.1080/00222895.1989.10735486.

[145] J. A. MacLean, J. Nataraj, J. Davies, A. Zakharova, J. Kurtz, M. A. Liker, J. Olaya, and T. D. Sanger. Novel utilization of deep brain stimulation in the pedunculopontine nucleus with globus pallidus internus for treatment of childhood-onset dystonia. *Frontiers in Human Neuroscience*, 17, 2023.

[146] B. Mädler and V. Coenen. Explaining clinical effects of deep brain stimulation through simplified target-specific modeling of the volume of activated tissue. *American Journal of Neuroradiology*, 33(6):1072–1080, 2012.

[147] N. Malfait and T. D. Sanger. Does dystonia always include co-contraction? a study of unconstrained reaching in children with primary and secondary dystonia. *Experimental Brain Research*, 176:206–216, 1 2007.

[148] L. Mar-Barrutia, E. Real, C. Segalás, S. Bertolín, J. Menchón, and P. Alonso. Deep brain stimulation for obsessive-compulsive disorder: A systematic review of worldwide experience after 20 years. *World J Psychiatry*, 11(9):659–680, 2021.

[149] E. Marinari, G. Parisi, and F. Zuliani. Four-dimensional spin glasses in a magnetic field have a mean-field-like phase. *Journal of Physics A: Mathematical and General*, 31(4):1181, 1998.

[150] V. Marmarelis. *Analysis of physiological systems: The white-noise approach*. Springer Science & Business Media, 2012.

[151] C. D. Marsden and J. A. Obeso. The functions of the basal ganglia and the paradox of stereotaxic surgery in Parkinson's disease. *Brain*, 117(4):877–897, 08 1994.

[152] A. E. Martinez-Nunez, M. B. Justich, M. S. Okun, and A. Fasano. Emerging therapies for neuromodulation in parkinson's disease. *Neurotherapeutics*, 21(3):e00310, 2024.

[153] K. W. McCairn and R. S. Turner. Deep brain stimulation of the globus pallidus internus in the parkinsonian primate: local entrainment and suppression of low-frequency oscillations. *Journal of neurophysiology*, 101(4):1941–1960, 2009.

[154] V. M. McClelland, A. Valentin, H. G. Rey, D. E. Lumsden, M. C. Elze, R. Selway, G. Alarcon, and J.-P. Lin. Differences in globus pallidus neuronal firing rates and patterns relate to different disease biology in children with dystonia. *Journal of Neurology, Neurosurgery & Psychiatry*, 87(9):958–967, 2016.

[155] C. C. McIntyre and T. J. Foutz. Computational modeling of deep brain stimulation. *Handbook of clinical neurology*, 116:55–61, 2013.

[156] C. C. McIntyre, M. Savasta, L. Kerkerian-Le Goff, and J. L. Vitek. Uncovering the mechanism (s) of action of deep brain stimulation: activation, inhibition, or both. *Clinical neurophysiology*, 115(6):1239–1248, 2004.

[157] J. Mink and W. Thach. Basal ganglia motor control. i. nonexclusive relation of pallidal discharge to five movement modes. *Journal of neurophysiology*, 65(2):273–300, 1991.

[158] J. Mink and W. Thach. Basal ganglia motor control. iii. pallidal ablation: normal reaction time, muscle cocontraction, and slow movement. *Journal of neurophysiology*, 65(2):330–351, 1991.

[159] J. W. Mink. The basal ganglia: Focused selection and inhibition of competing motor programs, 1996.

[160] J. W. Mink. The Basal Ganglia and Involuntary Movements: Impaired Inhibition of Competing Motor Patterns. *Archives of Neurology*, 60(10):1365–1368, 10 2003.

[161] J. W. Mink and T. Thach. Basal ganglia intrinsic circuits and their role, 1993.

[162] S. Miocinovic, C. de Hemptinne, W. Chen, F. Isbaine, J. T. Willie, J. L. Ostrem, and P. A. Starr. Cortical potentials evoked by subthalamic stimulation demonstrate a short latency hyperdirect pathway in humans. *Journal of Neuroscience*, 38(43):9129–9141, 2018.

[163] S. Mitchell, R. Richardson, F. Baker, and M. DeLong. The primate nucleus basalis of meynert: neuronal activity related to a visuomotor tracking task. *Experimental brain research*, 68(3):506–515, 1987.

[164] C. K. E. Moll, E. Galindo-Leon, A. Sharott, A. Gulberti, C. Buhmann, J. A. Koeppen, M. Biermann, T. Bäumer, S. Zittel, M. Westphal, C. Gerloff, W. Hamel, A. Münchau, and A. K. Engel. Asymmetric pallidal neuronal activity in patients with cervical dystonia. *Frontiers in Systems Neuroscience*, 8(FEB), 2014. Cited by: 60; All Open Access, Gold Open Access, Green Open Access.

[165] E. Monbaliu, K. Himmelmann, J.-P. Lin, E. Ortibus, L. Bonouvrié, H. Feys, R. J. Vermeulen, and B. Dan. Clinical presentation and management of dyskinetic cerebral palsy. *The Lancet Neurology*, 16(9):741–749, 2017.

[166] E. B. Montgomery Jr and J. T. Gale. Mechanisms of action of deep brain stimulation (dbs). *Neuroscience & Biobehavioral Reviews*, 32(3):388–407, 2008.

[167] A. Moran, E. Stein, H. Tischler, K. Belelovsky, and I. Bar-Gad. Dynamic stereotypic responses of basal ganglia neurons to subthalamic nucleus high-frequency stimulation in the parkinsonian primate. *Frontiers in systems neuroscience*, 5:21, 2011.

[168] R. Moran, D. A. Pinotsis, and K. Friston. Neural masses and fields in dynamic causal modelling. *Frontiers in Computational Neuroscience*, 4 2013.

[169] R. J. Moran, S. J. Kiebel, K. E. Stephan, R. B. Reilly, J. Daunizeau, and K. J. Friston. A neural mass model of spectral responses in electrophysiology. *NeuroImage*, 37:706–720, 9 2007.

[170] C. Morris and H. Lecar. Voltage oscillations in the barnacle giant muscle fiber. *Biophysical journal*, 35(1):193–213, 1981.

[171] H. Mäenpää and [et al.]. Effect of sensory-level electrical stimulation of the tibialis anterior muscle during physical therapy on active dorsiflexion of the ankle of children with cerebral palsy. *Pediatric Physical Therapy: The Official Publication of the Section on Pediatrics of the American Physical Therapy Association*, 16(1):39–44, 2004.

[172] A. Nambu. A new dynamic model of the cortico-basal ganglia loop. In *Brain Mechanisms for the Integration of Posture and Movement*, volume 143 of *Progress in Brain Research*, pages 461–466. Elsevier, 2004.

[173] A. Nambu, S. Yoshida, and K. Jinnai. Movement-related activity of thalamic neurons with input from the globus pallidus and projection to the motor cortex in the monkey. *Experimental Brain Research*, 84(2):279–284, Apr 1991.

[174] W.-J. Neumann, A. Horn, S. Ewert, J. Huebl, C. Brücke, C. Slentz, G.-H. Schneider, and A. A. Kühn. A localized pallidal physiomarker in cervical dystonia. *Annals of Neurology*, 82(6):912–924, 2017.

[175] M. Niethammer, M. Carbon, M. Argyelan, and D. Eidelberg. Hereditary dystonia as a neurodevelopmental circuit disorder: Evidence from neuroimaging. *Neurobiology of Disease*, 42(2):202–209, 2011. Special Issue: Advances in dystonia.

[176] N. Novaretti, A. Cunha, T. Bezerra, M. Pereira, D. de Oliveira, M. Brito, A. Pimentel, T. Brozinga, M. Foss, and V. Tumas. The prevalence and correlation of non-motor symptoms in adult patients with idiopathic focal or segmental dystonia. *Tremor and Other Hyperkinetic Movements (N Y)*, 9:596, 2019.

[177] J. A. Obeso and J. L. Lanciego. Past, present, and future of the pathophysiological model of the basal ganglia, 7 2011.

[178] M. K. O'Brien and A. A. Ahmed. Does risk-sensitivity transfer across movements? *Journal of Neurophysiology*, 109:1866–1875, 2013.

[179] S. Owen, J. Heath, M. Kringelbach, A. Green, E. Pereira, N. Jenkinson, T. Jegan, J. Stein, and T. Aziz. Pre-operative dti and probabilisitic tractography in four patients with deep brain stimulation for chronic pain. *Journal of Clinical Neuroscience*, 15(7):801–805, 2008.

[180] S. Owen, J. Heath, M. Kringelbach, J. Stein, and T. Aziz. Preoperative dti and probabilistic tractography in an amputee with deep brain stimulation for lower limb stump pain. *British journal of neurosurgery*, 21(5):485–490, 2007.

[181] M. Paff, A. Loh, C. Sarica, A. M. Lozano, and A. Fasano. Update on current technologies for deep brain stimulation in parkinson's disease. *Journal of movement disorders*, 13(3):185–198, 9 2020.

[182] A. Pana and B. Saggu. Dystonia. In: StatPearls [Internet], Jan 2023. [Updated 2023 Sep 4]. Available from: https://www.ncbi.nlm.nih.gov/books/NBK448144/.

[183] M. Penner, W. Y. Xie, N. Binepal, L. Switzer, and D. Fehlings. Characteristics of Pain in Children and Youth With Cerebral Palsy. *Pediatrics*, 132(2):e407–e413, 08 2013.

[184] J. B. Penney and A. B. Young. Gaba as the pallidothalamic neurotransmitter: implications for basal ganglia function, 1981.

[185] J. B. Penney and A. B. Young. Striatal inhomogeneities and basal ganglia function, 1986.

[186] I. Pereira, S. Frässle, J. Heinzle, D. Schöbi, C. T. Do, M. Gruber, and K. E. Stephan. Conductance-based dynamic causal modeling: A mathematical review of its application to cross-power spectral densities, 12 2021.

[187] D. A. Peterson, T. J. Sejnowski, and H. Poizner. Convergent evidence for abnormal striatal synaptic plasticity in dystonia. *Neurobiology of Disease*, 37(3):558–573, 2010.

[188] J. Pingel, M. S. Nielsen, T. Lauridsen, K. Rix, M. Bech, T. Alkjaer, I. T. Andersen, J. B. Nielsen, and R. Feidenhansl. Injection of high dose botulinum-toxin a leads to impaired skeletal muscle function and damage of the fibrilar and non-fibrilar structures. *Scientific Reports*, 7(1):14746, 2017.

[189] D. Piña-Fuentes, J. van Dijk, G. Drost, J. van Zijl, T. van Laar, M. Tijssen, and M. Beudel. Direct comparison of oscillatory activity in the motor system of parkinson's disease and dystonia: A review of the literature and meta-analysis. *Clinical Neurophysiology*, 130(6):917–924, 2019.

[190] C. N. Prudente, E. J. Hess, and H. A. Jinnah. Dystonia as a network disorder: What is the role of the cerebellum?, 2 2014.

[191] C. Pélabon, C. H. Hilde, S. Einum, and M. Gamelon. On the use of the coefficient of variation to quantify and compare trait variation. *Evolution Letters*, 4:180–188, 6 2020.

[192] S. Rajan, B. Kaas, and E. Moukheiber. Movement disorders emergencies. *Seminars in Neurology*, 39(1):125–136, Feb 2019.

[193] B. Ribot, J. Aupy, M. Vidailhet, J. Mazère, A. Pisani, E. Bezard, D. Guehl, and P. Burbaud. Dystonia and dopamine: From phenomenology to pathophysiology, 11 2019.

[194] T. L. Richards, T. J. Grabowski, P. Boord, K. Yagle, M. Askren, Z. Mestre, P. Robinson, O. Welker, D. Gulliford, W. Nagy, et al. Contrasting brain patterns of writing-related dti parameters, fmri connectivity, and dti–fmri connectivity correlations in children with and without dysgraphia or dyslexia. *NeuroImage: Clinical*, 8:408–421, 2015.

[195] L. Rigoux, K. E. Stephan, K. J. Friston, and J. Daunizeau. Bayesian model selection for group studies - revisited. *NeuroImage*, 84:971–985, 1 2014.

[196] M. J. Rosa, J. Kilner, F. Blankenburg, O. Josephs, and W. Penny. Estimating the transfer function from neuronal activity to bold using simultaneous eeg-fmri. *Neuroimage*, 49(2):1496–1509, 2010.

[197] P. M. Rossini, R. Di Iorio, M. Bentivoglio, G. Bertini, F. Ferreri, C. Gerloff, R. J. Ilmoniemi, F. Miraglia, M. A. Nitsche, F. Pestilli, et al. Methods for analysis of brain connectivity: An ifcn-sponsored review. *Clinical Neurophysiology*, 130(10):1833–1858, 2019.

[198] J. B. Rowe. Connectivity analysis is essential to understand neurological disorders. *Frontiers in Systems Neuroscience*, 4:144, 2010.

[199] K. S. Rudolph, M. J. Axe, and L. Snyder-Mackler. Dynamic stability after acl injury: Who can hop? *Knee Surgery, Sports Traumatology, Arthroscopy*, 8:262–269, 2000.

[200] T. Sanger. Childhood onset generalised dystonia can be modelled by increased gain in the indirect basal ganglia pathway. *Journal of Neurology, Neurosurgery, and Psychiatry*, 74(11):1509, 2003.

[201] T. D. Sanger. Failure of Motor Learning for Large Initial Errors. *Neural Computation*, 16(9):1873–1886, 09 2004.

[202] T. D. Sanger. Arm trajectories in dyskinetic cerebral palsy have increased random variability. *Journal of child neurology*, 21:551–557, 7 2006.

[203] T. D. Sanger. Bayesian filtering of myoelectric signals. *Journal of neurophysiology*, 97(2):1839–1845, 2007.

[204] T. D. Sanger. Risk-aware control. *Neural Computation*, 26:2669–2691, 12 2014.

[205] T. D. Sanger. Basic and translational neuroscience of childhood-onset dystonia: A control-theory perspective. *Annual Review of Neuroscience*, 41:41–59, 2018.

[206] T. D. Sanger. A computational model of deep-brain stimulation for acquired dystonia in children. *Frontiers in Computational Neuroscience*, 12, 2018.

[207] T. D. Sanger. Deep brain stimulation for cerebral palsy: where are we now? *Developmental Medicine and Child Neurology*, 62(1):28–33, 2020.

[208] T. D. Sanger, D. Chen, D. L. Fehlings, M. Hallett, A. E. Lang, J. W. Mink, H. S. Singer, K. Alter, H. Ben-Pazi, E. E. Butler, R. Chen, A. Collins, S. Dayanidhi, H. Forssberg, E. Fowler, D. L. Gilbert, S. L. Gorman, M. E. Gormley, H. A. Jinnah, B. Kornblau, K. J. Krosschell, R. K. Lehman, C. MacKinnon, C. J. Malanga, R. Mesterman, M. B. Michaels, T. S. Pearson, J. Rose, B. S. Russman, D. Sternad, K. J. Swoboda, and F. Valero-Cuevas. Definition and classification of hyperkinetic movements in childhood, 8 2010.

[209] T. D. Sanger, M. R. Delgado, D. Gaebler-Spira, M. Hallett, J. W. Mink, and Task Force on Childhood Motor Disorders. Classification and definition of disorders causing hypertonia in childhood. *Pediatrics*, 111(1):e89–e97, Jan 2003.

[210] T. D. Sanger, J. Kaiser, and B. Placek. Reaching movements in childhood dystonia contain signal-dependent noise. *Journal of Child Neurology*, 20:489–496, 6 2005. doi: 10.1177/08830738050200060401.

[211] T. D. Sanger and S. N. Kukke. Abnormalities of tactile sensory function in children with dystonic and diplegic cerebral palsy. *Journal of child neurology*, 22:289–293, 3 2007.

[212] T. D. Sanger, M. Liker, E. Arguelles, R. Deshpande, A. Maskooki, D. Ferman, A. Tongol, and A. Robison. Pediatric deep brain stimulation using awake recording and stimulation for target selection in an inpatient neuromodulation monitoring unit. *Brain sciences*, 8(7), 7 2018.

[213] T. D. Sanger, A. Pascual-Leone, D. Tarsy, and G. Schlaug. Nonlinear sensory cortex response to simultaneous tactile stimuli in writer's cramp, 1 2002.

[214] T. D. Sanger, A. Robison, E. Arguelles, D. Ferman, and M. Liker. Case report: Targeting for deep brain stimulation surgery using chronic recording and stimulation in an inpatient neuromodulation monitoring unit, with implantation of electrodes in gpi and vim in a 7-year-old child with progressive generalized dystonia. *Journal of child neurology*, 33(12):776–783, 10 2018.

[215] T. D. Sanger, D. Tarsy, and A. Pascual-Leone. Abnormalities of spatial and temporal sensory discrimination in writer's cramp, 1 2001.

[216] E. R. Santos. Understanding drug-induced movement disorders: Causes, symptoms, and treatment. 2024.

[217] J. Schlaier, J. Anthofer, K. Steib, C. Fellner, E. Rothenfusser, A. Brawanski, and M. Lange. Deep brain stimulation for essential tremor: targeting the dentato-rubro-thalamic tract? *Neuromodulation: Technology at the Neural Interface*, 18(2):105–112, 2015.

[218] R. Schmidt, E. Verstraete, M. A. de Reus, J. H. Veldink, L. H. van den Berg, and M. P. van den Heuvel. Correlation between structural and functional connectivity impairment in amyotrophic lateral sclerosis. *Human brain mapping*, 35(9):4386–4395, 2014.

[219] R. A. Schmidt and D. E. Sherwood. An inverted-–u relation between spatial error and force requirements in rapid limb movements: Further evidence for the impulse-variability model. *Journal of Experimental Psychology: Human Perception and Performance*, 8:158–170, 1982.

[220] S. L. Schmidt, D. T. Brocker, B. D. Swan, D. A. Turner, and W. M. Grill. Evoked potentials reveal neural circuits engaged by human deep brain stimulation. *Brain Stimulation*, 13(6):1706–1718, 2020.

[221] T. Schönecker, D. Gruber, A. Kivi, B. Müller, E. Lobsien, G.-H. Schneider, A. A. Kühn, K.-T. Hoffmann, and A. R. Kupsch. Postoperative mri localisation of electrodes and clinical efficacy of pallidal deep brain stimulation in cervical dystonia. *Journal of Neurology, Neurosurgery & Psychiatry*, 86(8):833–839, 2015.

[222] B. C. Schwab, D. Kase, A. Zimnik, R. Rosenbaum, M. G. Codianni, J. E. Rubin, and R. S. Turner. Neural activity during a simple reaching task in macaques is counter to gating and rebound in basal ganglia–thalamic communication. *PLOS Biology*, 18(10):1–38, 10 2020.

[223] S. R. Searle, F. M. Speed, and G. A. Milliken. Population marginal means in the linear model: An alternative to least squares means. *American Statistician*, 34:216–221, 1980.

[224] V. G. Shakkottai, A. Batla, K. Bhatia, W. T. Dauer, C. Dresel, M. Niethammer, D. Eidelberg, R. S. Raike, Y. Smith, H. A. Jinnah, E. J. Hess, S. Meunier, M. Hallett, R. Fremont, K. Khodakhah, M. S. LeDoux, T. Popa, C. Gallea, S. Lehericy, A. C. Bostan, and P. L. Strick. Current opinions and areas of consensus on the role of the cerebellum in dystonia, 4 2017.

[225] V. Sharma, M. Patel, and S. Miocinovic. Surgical treatment of parkinson's disease: Devices and lesion approaches. *Neurotherapeutics*, 17(4):1525–1538, Oct 2020.

[226] N. C. Sinclair, J. B. Fallon, K. J. Bulluss, W. Thevathasan, and H. J. McDermott. On the neural basis of deep brain stimulation evoked resonant activity. *Biomedical Physics amp; Engineering Express*, 5:057001, 8 2019.

[227] B. C. Souza, V. Lopes-dos Santos, J. Bacelo, and A. B. L. Tort. Spike sorting with gaussian mixture models. *Scientific Reports*, 9(1):3627, 2019.

[228] P. A. Starr, R. S. Turner, G. Rau, N. Lindsey, S. Heath, M. Volz, J. L. Ostrem, and W. J. Marks. Microelectrode-guided implantation of deep brain stimulators into the globus pallidus internus for dystonia: techniques, electrode locations, and outcomes. *Journal of Neurosurgery JNS*, 104(4):488–501, 2006.

[229] C. R. Steinhardt, P. Sacré, T. C. Sheehan, J. H. Wittig, S. K. Inati, S. Sarma, and K. A. Zaghloul. Characterizing and predicting cortical evoked responses to direct electrical stimulation of the human brain. *Brain Stimulation*, 13(5):1218–1225, 2020.

[230] A. Stenman, F. Gustafsson, D. E. Rivera, L. Ljung, and T. McKelvey. On adaptive smoothing of empirical transfer function estimates. *Control Engineering Practice*, 8(11):1309–1315, 2000.

[231] D. Sternad, M. O. Abe, X. Hu, and H. Müller. Neuromotor noise, error tolerance and velocity-dependent costs in skilled performance. *PLOS Computational Biology*, 7:e1002159, 9 2011.

[232] K. Stewart, A. Harvey, and L. M. Johnston. A systematic review of scales to measure dystonia and choreoathetosis in children with dyskinetic cerebral palsy. *Developmental Medicine & Child Neurology*, 59(8):786–795, 2017.

[233] Y. e. a. Sui. Deep Brain Stimulation Initiative: Toward Innovative Technology, New Disease Indications, and Approaches to Current and Future Clinical Challenges in Neuromodulation Therapy. *Frontiers in Neurology*, 11, 2021.

[234] K. Tambirajoo, L. Furlanetti, M. Samuel, and K. Ashkan. Subthalamic Nucleus Deep Brain Stimulation in Post-Infarct Dystonia. *Stereotactic and Functional Neurosurgery*, 98(6):386–398, 08 2020.

[235] D. Tarsy and D. K. Simon. Dystonia. *New England Journal of Medicine*, 355:818–829, 8 2006. doi: 10.1056/NEJMra055549.

[236] P. A. Taylor, A. Alhamud, A. van der Kouwe, M. G. Saleh, B. Laughton, and E. Meintjes. Assessing the performance of different dti motion correction strategies in the presence of epi distortion correction. *Human brain mapping*, 37(12):4405–4424, Dec 2016.

[237] P. Termsarasab, T. Thammongkolchai, and S. Frucht. Medical treatment of dystonia. *Journal of Clinical Movement Disorders*, 3:19, 2016. Erratum in: J Clin Mov Disord. 2018 Nov 16;5:8.

[238] C. Trompetto, A. Currà, L. Puce, L. Mori, C. Serrati, F. Fattapposta, G. Abbruzzese, and L. Marinelli. Spastic dystonia in stroke subjects: prevalence and features of the neglected phenomenon of the upper motor neuron syndrome. *Clinical Neurophysiology*, 130(4):521–527, Apr 2019.

[239] J. S. Vidmark, E. Hernandez-Martin, and T. D. Sanger. *Increasing Consistency of Evoked Response in Thalamic Nuclei During Repetitive Burst Stimulation of Peripheral Nerve in Humans*, volume 12908 LNCS. Springer International Publishing, Cham, 2021.

[240] J. L. Vitek. Mechanisms of deep brain stimulation: excitation or inhibition. *Movement disorders: official journal of the Movement Disorder Society*, 17(S3):S69–S72, 2002.

[241] J. L. Vitek. Pathophysiology of dystonia: A neuronal model, 2002.

[242] J. L. Vitek, V. Chockkan, J. Y. Zhang, Y. Kaneoke, M. Evatt, M. R. DeLong, S. Triche, K. Mewes, T. Hashimoto, and R. A. Bakay. Neuronal activity in the basal ganglia in patients with generalized dystonia and hemiballismus. *Annals of Neurology*, 46:22–35, 1999.

[243] Y. Wang, P. Li, F. Gong, Y. Gao, Y. Xu, and W. Wang. Micro lesion effect of the globus pallidus internus with deep brain stimulation in parkinson's disease patients. *Acta Neurochir (Wien)*, 159(9):1727–1731, Sept. 2017. Epub 2017 Jul 28.

[244] P. J. Winklewski, A. Sabisz, P. Naumczyk, K. Jodzio, E. Szurowska, and A. Szarmach. Understanding the physiopathology behind axial and radial diffusivity changes—what do we know? *Frontiers in Neurology*, 9, 2018.

[245] W. Xu, J. Wang, X.-N. Li, J. Liang, L. Song, Y. Wu, Z. Liu, B. Sun, and W.-G. Li. Neuronal and synaptic adaptations underlying the benefits of deep brain stimulation for parkinson's disease. *Translational Neurodegeneration*, 12(1):55, 2023.

[246] T. Yamamoto. Recent advancement of technologies and the transition to new concepts in epilepsy surgery. *Neurological Surgery (Tokyo)*, 60(12):581–593, 2020. Epub 2020 Nov 18.

[247] F. Yeh. Diffusion mri reconstruction in dsi studio. *Advanced Biomedical MRI Lab, National Taiwan University Hospital. Available online at: http://dsi-studio. labsolver. org/Manual/Reconstruction# TOC-Q-Space-Diffeomorphic-Reconstruction-QSDR*, 2017.

[248] C. Yen, C.-L. Lin, and M.-C. Chiang. Exploring the frontiers of neuroimaging: a review of recent advances in understanding brain functioning and disorders. *Life*, 13(7):1472, 2023.

[249] S. J. Young, J. V. Doornik, and T. D. Sanger. Visual feedback reduces co-contraction in children with dystonia. *Journal of Child Neurology*, 26:37–43, 1 2011.

[250] B. Youngerman, F. Khan, and G. McKhann. Stereoelectroencephalography in epilepsy, cognitive neurophysiology, and psychiatric disease: safety, efficacy, and place in therapy. *Neuropsychiatric Disease and Treatment*, 15:1701–1716, 2019.

[251] E. Zarahn, G. D. Weston, J. Liang, P. Mazzoni, and J. W. Krakauer. Explaining savings for visuomotor adaptation: linear time-invariant state-space models are not sufficient. *Journal of neurophysiology*, 100(5):2537–2548, 2008.

[252] S. Zhao, G. Li, C. Tong, W. Chen, P. Wang, J. Dai, X. Fu, Z. Xu, X. Liu, L. Lu, et al. Full activation pattern mapping by simultaneous deep brain stimulation and fmri with graphene fiber electrodes. *Nature communications*, 11(1):1788, 2020.

[253] X. Zhou, X. Cao, and X. Ren. Speed-accuracy tradeoff in trajectory-based tasks with temporal constraint. In T. Gross, J. Gulliksen, P. Kotzé, L. Oestreicher, P. Palanque, R. O. Prates, and M. Winckler, editors, *Human-Computer Interaction – INTERACT 2009*, pages 906–919, Berlin, Heidelberg, 2009. Springer Berlin Heidelberg.

[254] G. Zorzi, C. Marras, N. Nardocci, A. Franzini, L. Chiapparini, E. Maccagnano, L. Angelini, D. Caldiroli, and G. Broggi. Stimulation of the globus pallidus internus for childhood-onset dystonia. *Movement Disorders*, 20(9):1194–1200, 2005.

Appendix A

ABBREVIATIONS

AD Axial Diffusivity

ANOVA Analysis of Variance

BF Biofeedback

CCI Co-contraction Index

CHLA Children's Hospital Los Angeles

CHOC Children's Health Orange County

CNS Central Nervous System

CP Cerebral Palsy

CPSD Cross Spectral Density

CT Computed Tomography

CV coefficient of variation

DBS Deep Brain Stimulation

DTI Diffusion Tensor Imaging

DWI Diffusion Weighted Imaging

ECU Extensor Carpi Radialis

EEG Electroencephalography

EMG Electromyography

EP Evoked Potential

EPI Echo Planar Imaging

FA Fractional Anisotropy

FCR Flexor Carpi Radialis

FFT Fast Fourier Transform

FOV Field of View

GA1 Glutaric Aciduria Type 1

GLM Generalized Linear Model

GMM Gaussian Mixture Model

GPe Globus Pallidus Externus

GPi Globus Pallidus Internus

GUI Graphical User Interface

HFO High-Frequency Oscillation

IoD Index of Difficulty

IP Index of Performance

LFO Low-Frequency Oscillation

LFP Local Field Potential

LMER Linear Mixed Effects Model

LTI Linear Time Invariant

MP RAGE Magnetization-Prepared Rapid Gradient-Echo

MRI Magnetic Resonance Imaging

MT Movement Time

MVC Maximum Voluntary Contraction

NEO Non-linear Energy Operator

NMU Neuromodulation Monitoring Unit

P2P Peak-to-Peak Amplitude

PCA Principal Component Analysis

PD Parkinson's disease

PFR Peak to Floor Ratio

PPN Pedunculopontine Nucleus

PSD Power Spectral Density

SATO Speed-Accuracy Trade-off

sEEG Stereo-Electroencephalography

SISO Single Input Single Output

SNr Substantia Nigra Reticulata

SNR Signal to Noise Ratio

STN Subthalamic Nucleus

T2P Time to (first-)Peak Delay

TCI Task-Correlation Index

TE Echo Time

TR Repetition Time

UCI University of California, Irvine

USC University of Southern California

VA Ventral Anterior Nucleus

VIM Ventral Intermediate Nucleus

VO Ventral Oralis Anterior/Posterior

VoaVop Ventral Oralis Anterior/Posterior

VPL Ventral Posterolateral Nucleus